Surface Characterisation with Nonlinear Methods Based on Scale Analysis

Von der Fakultät für Mathematik und Naturwissenschaften
der Carl von Ossietzky Universität Oldenburg
zur Erlangung des Grades und Titels eines
Doktors der Naturwissenschaften (Dr. rer. nat.)
angenommene Dissertation
von Herrn

Kevin Bube

geboren am 22.4.1977
in Stade

Oldenburg 2007

Gutachterin : Prof. Dr. Ulrike Feudel
Zweitgutachter : Prof. Dr. Ulrich Parlitz
Tag der Disputation : 2. Mai 2007

Abstract

In this thesis we develop methods for the analysis of surfaces whose formation processes are not exactly describable. We demonstrate the methods for two examples. The first is a metal surface generated by the processing with a laser device, the second is the electron microscopy image of a cross section through a tidal flat sediment. Both surfaces are created by a complicated interplay of processes for which no closed mathematical model is available. The processes are acting on different time and spatial scales. We make use of this property and use a nonlinear methodology which emphasises these features, respectively.

The analysis of the laser surfaces is done to develop a control mechanism to suppress unwanted surface structures that are created while processing. We achieve this by developing a mathematical characterisation of the structures which connects the surface structures with the external process parameters. From the sediment analysis we gain insight into formation histories and distinguish regions in the sediment which were created by different formation mechanisms. Therefore, we detect structural differences between the various sediment layers and quantify these. The scale analysing methods yield very good results in both cases, despite the dissimilarity of the applications.

For the laser generated surface we mainly use adapted multifractal methods but also standard linear methods are applied. We derive a connection between the multifractal spectrum exhibited by the surfaces and the external process parameters. This allows the prediction of expected surface qualities and therefore an offline process control. We state a parameter window that yields the best possible surface quality with this process.

Furthermore, we develop an algorithm which finds layer boundaries in sediment images. This turns out to be a very helpful tool for further analyses. Additionally, we propose an entropy measure based method which allows a quantification of the structures within the sediment layers. We develop a noise reduction method involving symbolic dynamics and cluster analysis. The combination of the methods allows the assignment of formation process classes to the various layers. Therefore, we are able to divide biologically generated layers from sedimentation created ones.

Zusammenfassung

Die vorliegende Arbeit entwickelt Methoden zur Analyse von Oberflächenstrukturen, deren Entstehungsprozesse nicht exakt beschreibbar sind. Wir demonstrieren die Methoden anhand von zwei Beispielen. Beim ersten Beispiel handelt es sich um Metalloberflächen, welche mit einem Laser bearbeitet wurden. Beim zweiten um ein Elektronenmikroskopiebild eines Querschnitts durch ein Wattsediment. Beide Oberflächen sind durch ein kompliziertes Zusammenspiel verschiedener Prozesse entstanden, für die bisher kein geschlossenes mathematisches Modell zur Verfügung steht. Die Prozesse wirken auf verschiedenen räumlichen und zeitlichen Skalen. Dies machen wir uns zunutze und verwenden jeweils eine nichtlineare Methodik, die diese Eigenschaften hervorhebt.

Die Analyse der vom Laser bearbeiteten Oberflächen soll einen Kontrollmechanismus ermöglichen, der ungewollte Oberflächenstrukturen, die während der Bearbeitung entstehen, unterdrückt. Wir erreichen dies, indem wir eine mathematische Charakterisierung der Strukturen entwickeln, die einen Zusammenhang zwischen den Oberflächenstrukturen und externen Prozeßparametern herstellt. Die Sedimentanalyse gibt Einblicke in die Entstehungsgeschichte und unterscheidet Bereiche im Sediment, die auf unterschiedlichen Entstehungsprozessen beruhen. Dazu detektieren wir strukturelle Unterschiede zwischen den verschiedenen Sedimentschichten und quantifizieren diese. Trotz der Andersartigkeit der Anwendungen, erzielt die Verwendung von Skalenanalysemethoden in beiden Fällen sehr gute Ergebnisse.

Für die mit dem Laser bearbeiteten Oberflächen verwenden wir hauptsächlich angepaßte Multifraktalmethoden, sowie auch lineare Standardmethoden. Wir zeigen einen Zusammenhang zwischen dem Multifraktalspektrum der Oberflächen und den extern einstellbaren Prozeßparametern. Dies erlaubt die Vorhersage von erwarteten Oberflächengüten und damit eine Offline Prozeßsteuerung. Wir geben ein Parameterfenster an, welches die beste Oberflächengüte erzielt.

Weiterhin entwickeln wir einen Algorithmus zum Auffinden von Schichtgrenzen in Sedimentbildern. Es zeigt sich, daß dies ein nützliches Werkzeug für die

weiteren Analysen ist. Außerdem schlagen wir ein Verfahren vor, das eine Quantifizierung der Strukturen in den Sedimentschichten ermöglicht und auf einem Entropiemaß beruht. Ferner erreichen wir mit Hilfe von symbolischer Dynamik und Clusteranalyse eine Rauschreduktion. Die Kombination dieser Methoden erlaubt die Zuordnung von Klassen von Entstehungsprozessen zu einzelnen Schichten. Dadurch können wir biologisch erzeugte von durch Sedimentation erzeugten trennen.

Contents

1 Introduction

The characterisation of surfaces is a challenging task. It is frequently occurring mainly in solid state physics where the quality and properties of thin films or growing surfaces shall be quantified (Vázquez et al. 1994; Hoflund et al. 2000; Rath et al. 2005; Smith et al. 2006). Another typical example is the search of a connection between a surface and some process parameters (Schubart 1999; Waechter et al. 2003). The general problem is to reduce the information contained in a two dimensional (measurement) matrix to a small set of numbers. If a large set of data is measured in an experiment it is often impossible to compare each subset to the others. It is desirable to derive some few distinctive features from each measurement in order to compare them and to get an overview of the differences. However, finding the right measure that preserves useful information and drops uninteresting or redundant parts is not trivial in many cases.

The probably most prominent example for a simplified measure is the mean value. It is the projection of a more dimensional set to a single number. For some questions comparing the mean values of some data sets is fully satisfying although a great deal of information is disregarded. For example the mean values of surface heights does not say anything about the smoothness of the surface. Do all points have the same value or is there one large peak and no point comes close to the mean value at all? In order to take this into account another value is needed to quantify this. First approaches are the standard deviation or the variance. Another method is to look at the distribution function of the values at all points. This contains most information, but the number of values one needs for the quantification is also increased.

All these measures have in common that they describe only the global structures of the data set. The described structures are global in the sense that it does not matter if all points with high values are accumulated in one region or scattered all over the set. Another application where surface characterisation measures are needed is for structured surfaces, whose underlying formation processes are so complex that the development of a physical model description is impossible.

The difficulties can have various reasons. Often the gathering of information on the process is too complicated as measurements during the process are difficult. Another reason may be that many different processes take place and it is hard to separate them. In this case the processes mostly act on distinct time and spatial scales. Therefore, methods that distinguish between the scales and separate them reveal valuable information that may be used to develop a black box model.

In this thesis we develop and adapt suitable methods to characterise surfaces. They are able to extract and separate the information contained in multiple scales on the surfaces. This gives insight into systems which do not have an exact mathematical description. We apply the methods to measured data from two independent experiments. Our first example is a metal surface which was produced by a laser beam melt ablation process. This method was developed to provide a contact free tool to create depressions and forms from metals. Nowadays this is done by conventional milling devices which exhibit great toolwear and have problems generating complicated geometries or processing very hard or brittle materials. Unlike other laser processing methods which are already well established in the industrial production lines like laser cutting (Schuöcker 1986; Steen and Watkins 2003; Ermolaev et al. 2006), welding (Shao and Yan 2005; Mościcki et al. 2006) or drilling (Solana et al. 1999; Ruf et al. 2001), the laser beam melt ablation technique still suffers great problems regarding the resulting surface quality. Nevertheless, due to the great industrial interest in the technique, efforts have been made to solve the problems (Schubart 1999; Cser 2005). This ablation method is based on the melting of a surface with a high power laser and the simultaneous melt removing with a high pressure gas jet. At some process parameter combinations the device leaves tracks on the surface which arise from a complicated pattern formation process. Unfortunately these parameters are the technically relevant ones as they provide a compromise between amount of ablated material and processing speed. The aim is to suppress these structures that manifest in peaks and valleys on the material and to achieve a smooth surface with much ablated material. The origin of the unwanted structures lies in the interplay of a number of inseparable subprocesses that act on various time and spatial scales.

Two general strategies exist to improve the surface quality, an online and an offline control of the process. For an online control it is necessary to measure at least one state variable of the system continuously during the processing phase. Depending on the variable(s) the external forcing of the system has to be adjusted to push the process in the desired regime. An online control potentially yields the best results but is very hard to realise because it is experimentally quite complex to

supervise the process all the time. Furthermore a mathematical model is needed which connects the measurement state variables with the surface quality parameter(s). An offline control sets the suitable process parameters in advance and does not react on the current surface state. This setup is much simpler to realise and does not require a process model. Nevertheless, it may be a first step towards an online control.

We develop an offline control as a first approach. The gas jet that removes the material acts on a broad range of small scales due to its turbulent nature. The surface tension of the melt acts on larger scales. In our experiments there are two external parameters to tune the structures, the material feeding speed and the laser power. The intrinsic anisotropy of the process allows us to choose a one dimensional analysis of the surface structures. We take the measurement rows in ablation direction. These one dimensional data sets are analysed with methods known from fractal theory. We utilise two methods which estimate the multifractal spectrum of the sets, the wavelet transform modulus maxima method (Mallat and Hwang 1992; Arnéodo et al. 1995) and the detrended fluctuation analysis method (Kantelhardt et al. 2002). The multifractal spectrum measures the scaling of the surface heights around each measurement point versus the size of the regarded environment, thus providing a description for the local structure. This turns out to be an adequate description as it shows a correlation of the surface characteristics to parameters of the process. This connection is very important in order to develop a process control. Both the wavelet transform modulus maxima and the detrended fluctuation method should in theory yield the same results but recently it has been reported that this needs not to be the case for real data sets (Oświęcimka et al. 2006). We use both methods to make our results more reliable. Furthermore, do we also calculate linear measures often used by engineers (Cser 2005) and discuss possible state variables for an online control.

The second type of surfaces we survey are electron microscope images from tidal flat sediments. The images are density profiles of different chemical elements. The elements are usually clustered and form layers which differ in element abundance and average size of the contained clusters. In general, the succession of layers and the sediment constituents contain the information of the formation processes of the sediments. They allow conclusions on the environmental conditions in the past when the sediment was formed. It is of particular interest to conclude from the sedimentary layout to processes that created it (Pettijohn and Potter 1964; Tucker 2001; Anguy et al. 2001; Morford et al. 2003). Our analysed sediments originate from the Wadden Sea in the southern part of the North Sea and are

geologically very young (Gerdes et al. 1985; Block et al. 1991). They were formed by sedimentation and biological activity as well as chemical transformations. The separation of these processes is very complicated as the formation did not take place under laboratory conditions. One is particularly interested in distinguishing biologically formed regions from sedimentation dominated ones. Our samples consist of siliciclastic sediments containing microbial mats formed by microorganisms during dry periods. We develop methods to use the spatial element density configurations as proxies for formation processes. A method for finding the layer boundaries is introduced. It makes use of a wavelet multiscale decomposition (Mallat 1989a; Maroni et al. 2001), which is the successive removing of information in selected scales. The algorithm analyses the sediment samples at different scales and automatically divides the sample in regions with common element densities. The measurement process introduces additional measurement noise to the image, which is spatially very small scaled. As the noise is very disturbing for the image interpretation, we introduce a coarse graining technique which makes use of symbolic dynamics (Hao 1991; Ott 1993) to remove it. The method uses a clustering algorithm (Hartigan 1975) to divide the data set in a small number of classes. This effectively removes the noisy influences and shows the geometry of the element density layout. Furthermore, we develop a measure to quantify the clustering of the elements. It bases on the Kullback-Leibler distance (Kullback and Leibler 1951) between the element density distribution and a reference distribution. The measure may be applied over the whole surface or separately for each layer. This information can help sedimentologists to identify the formation process of the sediment as it quantitatively distinguishes different structures.

The thesis is organised as follows. It begins with an introduction of its intentions in chapter 1. Chapter 2 gives a short introduction and overview of the fundamental concepts of fractals. The multifractal methods used for the analysis of the surfaces generated by the laser beam melt ablation process are also explained. The following chapter 3 presents the analysis of these surfaces. A description of the process and the results of some linear analysis are shown. This includes correlation analysis as well as the calculation of the mean surface roughness. We proceed by presenting the application of the nonlinear multifractal methods. Chapter 4 presents the results of the analysis of the tidal flat sediments. Here a description of the sediment's original location and its features is given. Then the idea of the wavelet multiscale decomposition technique and the algorithm used to extract the layering in the samples is explained. This will be used in the later analysis. The chapter finally describes the developed image noise removal technique and the structure

quantification method with application to the sediment samples. Chapter 3 and 4 close with a short summary of the main results. The final chapter 5 contains an overall summary of all results and conclusions.

2 Theoretical concepts

This chapter describes some methods and theoretical concepts used in this thesis. We will give some basic information and simple examples for the readers not so familiar with these concepts. Furthermore, we define some terms and notations used throughout this thesis.

In the first two sections we will cope with scaling and (multi)fractality. Both concepts are strongly connected with each other. While the underlying basics were already known to mathematicians for quite some time, it was Hurst (1951) who found practical applications in nature for this while investigating the discharges of water basins. Mandelbrot generalised the approach (Mandelbrot 1967; Mandelbrot and van Ness 1968) and brought the mathematical construct of fractional dimensions (Cantor 1883; Hausdorff 1918) to it. He named such sets with fractional dimensions *fractals*. Mathematical examples include the von Koch curve, a curve which may be covered by a bounded two-dimensional object but whose length is infinite. The Sierpinski carpet is an example for an object in two dimensions. This object has holes whose total diameter is infinite but the area of the object vanishes. Finally, the Hilbert curve is a one dimensional curve which completely fills a two dimensional region without crossing itself (e.g. Feder (1988)). Since the original works of Mandelbrot many examples of fractal structures in nature have been analysed. The fingering in porous media that arises if a viscous liquid is brought into a porous medium exhibits fractal structures (Måløy et al. 1985). Those structures are also known if such a liquid is brought between two glass plates and then one plate is removed. It has also been shown that clouds have a fractal structure which is important for models on rainfall (Lovejoy 1982; Lovejoy and Schertzer 1985). Also the shape of the earth's landscape itself as well as trees and leafs exhibit fractal structures (Turcotte 1997).

A real boost was given to the topic by the upcoming area of nonlinear dynamical systems. Already founded by Poincaré, this research area did not experience many contributions until the works of Lorenz (1963) and Ruelle and Takens (1971). Since it was found that the attractors of many chaotic systems exhibit fractal

structures (*strange attractors*), a lot of applications were found. The Rayleigh-Bénard convection (Lorenz 1963; Ahlers and Behringer 1978), a dripping water faucet (Shaw 1984) and chemical reactions (Rössler 1976) were among the first systems investigated. Later examples for phase spaces of entities from all areas of scientific research were found to possess nonlinear structures (Ott 1981; Grebogi et al. 1987; Ott 1993). For some of those it turned out that a single dimension does not describe all features of the system, but a whole spectrum of dimensions is needed, the so called *multifractal spectrum*. We will make use of this approach in the following chapter.

There are various ways to estimate the multifractal spectrum from a data set. Although in the limit of an infinitely long set they should all converge to the same spectrum, there are differences in the convergence speed and the reliability of the estimation. We use two methods in this thesis, the wavelet transform modulus maxima (WTMM) method (Muzy et al. 1991; Arnéodo et al. 1995) as well as the detrended fluctuation analysis (DFA) method (Koscielny-Bunde et al. 1998; Kantelhardt et al. 2002). They are introduced in sec. 2.3.

2.1 Scaling

The fact that the shape of a tree can also be found similarly in all its branches and leafs can mathematically be described by the concept of scaling. Let $f(t)$ be some function $\mathbb{R} \to \mathbb{R}$. Then we say that the function is *scaling* if it has the property

$$f(\lambda t) = \lambda^{\alpha} f(t), \tag{2.1}$$

with the scaling exponent α.

A prominent example for a scaling set is the integral over a Wiener process

$$X(t) = \sum_{i=0}^{t} \xi_i \,, \tag{2.2}$$

often called random walk or Brownian motion (Feder 1988). The ξ_i are random variables with zero mean, standard deviation σ and are Gaussian distributed. The probability density function for $X(t) - X(t_0)$ is given by

$$\Phi(X(t) - X(t_0)) = \frac{1}{\sqrt{2\pi\sigma^2|t - t_0|}} \exp\left(- \frac{[X(t) - X(t_0)]^2}{2\sigma^2|t - t_0|} \right). \tag{2.3}$$

This function satisfies the scaling relation

$$\Phi(b^{1/2}[X(bt)-X(bt_0)]) = b^{-1/2}\Phi(X(t)-X(t_0)). \tag{2.4}$$

The Brownian motion is not only a scaling process, but it is also *self-affine*. A function $f(x,y)$ is self-affine if $f(rx, r^{Ha}y)$ is statistically similar to $f(x,y)$ (Turcotte 1997). r is a scaling factor, Ha the Hausdorff measure. In the special case of $Ha = 1$, f is called *self-similar*. The self-affinity of the Brownian motion can be seen by taking into account that the fluctuations $X(t)-X(t_0)$ are Gaussian distributed on any scale. Let $X(t)-X(t_0) = \xi'$ and $|t-t_0| = \tau$. We put this into (2.3) and get

$$\Phi(\xi',\tau) = \frac{1}{\sqrt{2\pi\sigma^2\tau}} \exp\left(-\frac{\xi'^2}{2\sigma^2\tau}\right). \tag{2.5}$$

If we scale τ by $b\tau$ and ξ' by $b^{1/2}\xi'$, we get the self-affinity relation

$$\Phi(b^{1/2}\xi', b\tau) = b^{-1/2}\Phi(\xi,\tau). \tag{2.6}$$

For independent, Gaussian random variables $\xi(t)$ the variance of the increments of the Brownian motion scales like

$$\langle[X(t)-X(t_0)]^2\rangle \sim |t-t_0|^{2H}, \tag{2.7}$$

with $H = 1/2$. H is called *Hurst exponent*. For other values of H one speaks of fractional Brownian motion. The increments are not independent anymore in this case (Mandelbrot and van Ness 1968; Feder 1988). A possible way to construct such a process is to take the Fourier-transform of a usual Brownian motion process with statistically independent increments

$$\mathscr{F}(\omega) = \int_{-\infty}^{\infty} \xi(t) e^{i\omega t}\,\mathrm{d}t\,. \tag{2.8}$$

$\mathscr{F}(\omega)$ is then convolved by with an exponentially decreasing kernel and then transformed back:

$$X(t) = \frac{1}{2\pi}\int_{-\infty}^{\infty} \mathscr{F}(\omega)|\omega|^{-2H} e^{-i\omega t}\,\mathrm{d}\omega\,, \tag{2.9}$$

where we exclude the point $\omega = 0$.

It can be seen in Fig. 2.1 that realisations of fractional Brownian motion processes with small Hurst exponents fluctuate on small scales. For processes with larger exponents the curves look smoother and the variance diverges faster. The fluctuation scales are larger. Processes with $H > 0.5$ are called *persistent*. For a persistent particle that moves in one dimension at an infinitesimal time step it is more likely to keep the previous direction than to change it. For $H = 0.5$ the probability to go up or down is the same. For $H < 0.5$ the probability to change the direction is larger. This is called *anti-persistent*. We will also use these termini in the context of the laser generated surfaces to describe its features. From Eq. (2.4) it can be seen that persistent processes diverge slower than normal Brownian motion processes. Anti-persistent ones diverge faster. This can also nicely be seen from Fig. 2.1.

2.2 Fractal sets

In his famous article Mandelbrot (1967) introduced the concept of fractals, which was at that time only used in mathematics, to physics and geosciences. What followed was an enormous development in this area and the application to many fields and problems.

A fractal set is a set which has a fractional dimension. The probably most famous example is the *Cantor set*. This set is recursively defined. One begins with the unit interval, divides it into three equal parts and cuts out the middle part. Then one repeats the procedure with the remaining two parts and so on *ad infinitum*. A sketch for the first four recursion steps is shown in Fig. 2.2. The length l of occupied sites converges to 0, on the other hand the number of points N in the set stays infinite. The dimension of the set is somewhere between 0 (a point) and 1 (a line).

One way to define a reasonable dimension for such an object was given by Hausdorff (1918). But in physics the mostly used dimension definition is the *box counting dimension* (Ott 1993). It has some deficiencies over the Hausdorff dimension, but they are not important for most applications. The advantage of the box counting dimension is that it can be quite easily computed numerically.

The box counting dimension D_0 is defined by the scaling of the number of nonempty boxes N of size ϵ needed to cover the set

$$N(\epsilon) = \epsilon^{-D_0}. \tag{2.10}$$

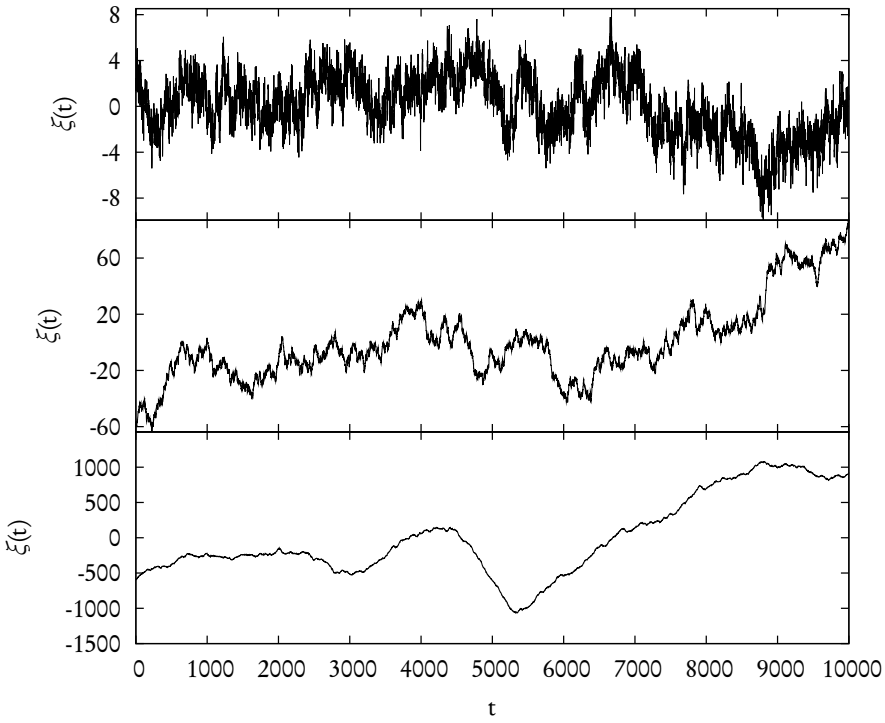

Figure 2.1: Fractional Brownian motion. The figure shows some realisations of fractional Brownian motion processes. From top to bottom: $H = 0.3$, $H = 0.5$ and $H = 0.7$. Note the different scales on the ordinate.

Figure 2.2: Construction of the Cantor set.

After simple calculus:

$$D_0 = \frac{\ln N(\epsilon)}{\ln 1/\epsilon}. \tag{2.11}$$

In the case of the Cantor set, the number of boxes is 2^n, where n is the recursion step, and the box length is 3^{-n}. This yields

$$D_0 = \frac{\ln 2^n}{\ln 3^n} \tag{2.12}$$

$$= \frac{\ln 2}{\ln 3} \tag{2.13}$$

$$\approx 0.63. \tag{2.14}$$

The definition of the dimension of fractal sets can be generalised as follows (Hentschel and Procaccia 1983; Grassberger 1983):

$$D_q = \frac{1}{1-q} \lim_{\epsilon \to 0} \frac{\ln I(q,\epsilon)}{\ln 1/\epsilon}, \tag{2.15}$$

with

$$I(q,\epsilon) = \sum_{i=1}^{N(\epsilon)} \mu_i^q, \tag{2.16}$$

where $q \in \mathbb{Z}$. μ_i is the mass within each box. In order to avoid a pole at $q = 1$ μ_i must be normalised to $\sum \mu_i = 1$. The Cantor set can be constructed by distributing the total mass of 1 equally on the occupied sites. In this way, the mass of all boxes always integrates to 1. The box counting dimension is a special case of Eq. 2.15 for $q = 0$. For D_0 the mass of each box does not matter as only the occupation is counted. This is not true for $q \neq 0$. D_1 is the so called information dimension, D_2 the correlation dimension. In the case of the Cantor set all these measures yield the same result, no matter how the boxes are weighted. Sets with this property are called *monofractals*. However, there are sets where the scaling depends on the parameter q. In the extreme case, the scaling may be different in every point of the set. Those sets are called *multifractals*.

The Cantor set may be generalised to a multifractal for example by not distributing the mass equally on both occupied parts in each iteration or not breaking it

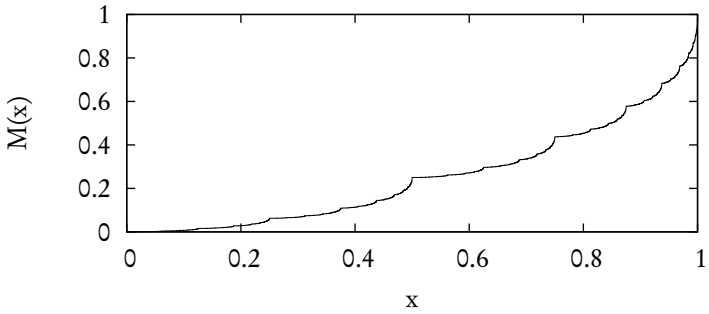

Figure 2.3: Integrated binomial multiplicative cascade. 15 iterations for $p = 0.25$ are shown here.

into parts of equal lengths. However, a more prominent example for a multifractal set is the *binomial multiplicative cascade* (Feder 1988). It is constructed by taking a unit interval and dividing it into two equal parts and assigning them the weights p and $1-p$, respectively, so that the total sum is always 1. The first iteration results in two intervals of weights μ_0 and μ_1. The second iteration yields four intervals of weights $\mu_0\mu_0$, $\mu_0\mu_1$, $\mu_1\mu_0$ and $\mu_1\mu_1$ and so forth. The integrated cascade is shown in Fig. 2.3.

The binomial multiplicative cascade has a different scaling in every point. A way to describe this set is to calculate the dimension of the point sets which have the same scaling. The number $\tilde{N}(k)$ of intervals which have the same product $\mu_{0,1} \cdot \ldots \cdot \mu_{0,1}$ is

$$\tilde{N}(k) = \binom{N}{k} = \frac{N!}{(N-k)!k!}, \tag{2.17}$$

where N is the iteration depth and $k = 0, \ldots, N$. With Eq. (2.10) we get the dimension f_k of the support of points with the same mass

$$f_k = \frac{\ln \tilde{N}(k)}{\ln 1/\epsilon} \tag{2.18}$$

$$= \frac{\ln \tilde{N}(k)}{N \ln 2}, \tag{2.19}$$

as the size of the intervals is $\epsilon = 2^{-N}$. The scaling of the mass within the intervals is given by

$$\alpha_k = \frac{\ln M(k)}{\ln 1/\epsilon}, \tag{2.20}$$

where $M(k)$ is the mass of an interval which contains k times μ_1 and $N-k$ times μ_0. The plot α versus $f(\alpha)$ is called the *multifractal spectrum* of the set (Halsey et al. 1986). The $f(\alpha)$ plot gives information about the dimensions of subsets with the same scaling of mass or more mathematically: Let $\mathscr{X} \subset \mathbb{R}$, $x \in \mathscr{X}$, $\epsilon > 0$ and

$$M(x) = \int\limits_{\substack{|x'-x|<\epsilon \\ x' \in \mathscr{X}}} dx'$$

then

$$f(\alpha) = \dim\{x | \lim_{\epsilon \to 0} - \frac{\ln M(x)}{\ln \epsilon} = \alpha\}. \tag{2.21}$$

A numerically more practical way to compute the different scalings of the points in a multifractal set is to use the weighted mass from Eq. (2.16)

$$\tau(q) = -\lim_{\epsilon \to 0} \frac{\ln I(q,\epsilon)}{\ln \epsilon}. \tag{2.22}$$

$\tau(q)$ is the so called *mass exponent*. It may be shown that it is related to the multifractal spectrum by the following relations (Feder 1988):

$$\alpha(q) = -\frac{d}{dq}\tau(q) \tag{2.23}$$

$$f(\alpha(q)) = q\alpha(q) + \tau(q). \tag{2.24}$$

$\alpha(q)$ is the *Hölder exponent*. In the special case $q = 0$ $f(\alpha)$ describes the box counting dimension of the multifractal set's support. This is obvious if one considers that the box counting dimension just counts the occupied sites disregarding their weights.

For the example of the binomial multiplicative process given above, $\tau(q)$ is given by

$$\begin{aligned}\tau(q) &= \frac{\ln\left(\sum_{k=0}^{N}\binom{N}{k}p^{qk}(1-p)^{q(N-k)}\right)}{N\ln 2}\\ &= \frac{\ln(p^q+(1-p)^q)}{\ln 2}.\end{aligned} \tag{2.25}$$

A method for directly estimating the multifractal spectrum was introduced by Chhabra and Jensen (1989). Their method works by using methods from probability theory. The information entropy of a process $\{x_i\}_{i=1}^{N}$ is defined by

$$S = -\sum_i p(x_i)\log p(x_i), \tag{2.26}$$

where $p(x_i)$ is the probability for x_i (Shannon 1948). The dimension of this process is given by

$$d = -\lim_{N\to\infty}\frac{1}{\log N}\sum_{i=1}^{N} p(x_i)\log p(x_i) \tag{2.27}$$

(Billingsley 1965). Chhabra and Jensen now defined the normalised quantity

$$\nu_i(q,\epsilon) = \frac{\mu_i(\epsilon)^q}{\sum_i \mu_i(\epsilon)^q} \tag{2.28}$$

where the support of $\{x_i\}_{i=1}^{N}$ is covered with boxes of size ϵ and in analogy to Eq. (2.16) the box masses μ_i are calculated. The weight q emphasises regions with higher (for $q > 0$) or lower mass (for $q < 0$). With Eq. (2.27) we can define the following two equations now

$$\begin{aligned}f(q) &= -\lim_{N\to\infty}\frac{1}{\log N}\sum_{i=1}^{N}\nu_i\log\nu_i\\ &= \lim_{\epsilon\to 0}\frac{1}{\log\epsilon}\sum_{i=1}^{N}\nu_i\log\nu_i\end{aligned} \tag{2.29}$$

$$\alpha(q) = -\lim_{N\to\infty} \frac{1}{\log N} \sum_{i=1}^{N} \nu_i \log x_i$$
$$= \lim_{\epsilon\to 0} \frac{1}{\log \epsilon} \sum_{i=1}^{N} \nu_i \log x_i \,. \tag{2.30}$$

These equations provide an elegant way to estimate the multifractal spectrum from a data set. The WTMM method makes use of them.

2.3 Numerical methods

In the following section an overview over the methods for estimating the multifractal spectrum used in this thesis will be given. The brute force method to estimate the spectrum is to use Eq. (2.22) to calculate the mass exponents and then use the transformation given by (2.23) and (2.24). However there are numerically superior methods as we will see in the next subsections.

2.3.1 Structure functions

The most straightforward approach for estimating the multifractal spectrum is the structure function method. For a given time series $\mathscr{Y} = \{y_n\}_{n=1}^{N}$ the scaling exponents α_q may be calculated as the moments of the increments

$$\langle \Delta y_n^q \rangle \propto \ell^{q\alpha_q} \,, \tag{2.31}$$

with $\Delta y_n = y_{n+\ell} - y_n$. The Legendre transform of α_q yields the Hausdorff dimension $D(\alpha)$ of the subset of $\mathscr{Y}$, where the increments scale with α.

This method is mainly used in the analysis of turbulence data and may be considered as a standard tool in that community (see eg. Vincent and Meneguzzi 1991). Its main drawback is its inability to characterise negative moments. For some time series where only small fluctuations or even constant regions occur, the method fails as Eq. (2.31) diverges in those regions.

2.3.2 Wavelet transform modulus maxima method

The wavelet transform modulus maxima method (WTMM) is a more sophisticated method to extract the multifractal spectrum from a time series (Muzy et al. 1991;

Mallat and Hwang 1992; Arnéodo et al. 1995). It was developed in order to overcome the deficiencies of the structure function method as it does not suffer from divergence problems. This method uses wavelets as natural box generators for the covering of the set. By wavelet transforming the set with a suitable wavelet a nice box covering is achieved. This method is very elegant as fast algorithms exist to compute the transform efficiently (Torrence and Compo 1998). Furthermore, a solid theoretical basis for the method exists (Mallat and Hwang 1992; Bacry et al. 1993).

The basic idea of the method is to use wavelets at various sizes in order to emphasise or suppress singularities within the analysed signal. The continuous wavelet transform of the sampled signal $\mathscr{Y} = \{y_n\}_{n=1}^{N}$ is given by

$$W_\psi[\mathscr{Y}](b,a) = \frac{1}{a}\sum_{n=1}^{N} \bar{\psi}\left(\frac{n-b}{a}\right) y_n \,, \tag{2.32}$$

where $a \in \mathbb{R}_{>0}$ is the dilatation of the wavelet, b its translation and $\bar{\psi}$ the complex conjugate of the wavelet ψ. ψ must be a square integrable function, that is

$$\int_{-\infty}^{+\infty} |\psi(x)|^2 \, dx < \infty \,. \tag{2.33}$$

For the WTMM the wavelets are required to be orthogonal to some low order polynomials

$$\int_{-\infty}^{+\infty} x^m \psi(x) \, dx = 0, \qquad 0 \le m < n_\psi \,. \tag{2.34}$$

This gives us the nice feature of removing polynomial trends of orders smaller than n_ψ from the data. This is often required as systematic trends disturb the real signal. The class of wavelets used throughout this thesis is given by successive derivatives of the Gaussian function (DOGN)

$$\psi^{(N)}(x) = \frac{(-1)^{N+1}}{\sqrt{\Gamma(N+\frac{1}{2})}} \frac{d^N}{dx^N} e^{-x^2/2} \,, \tag{2.35}$$

for which $n_\psi = N$ (Arnéodo et al. 1995). Figure 2.4 shows the second derivative of the Gaussian function (DOG2) wavelet. Due to its shape it is often called Mexican

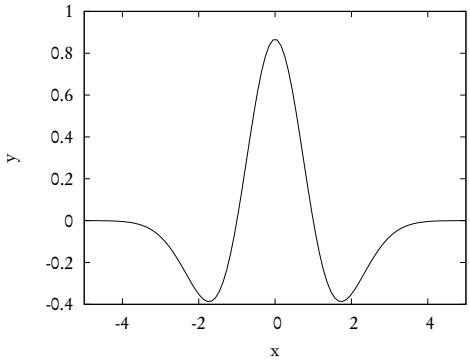

Figure 2.4: Second derivative of a Gaussian wavelet

hat wavelet. The parameter a controls the width of the wavelet peak, while b shifts it over the data set. The area within the peak is emphasised, while the rest is damped. This makes the wavelet a natural microscope for a data set.

The Hölder exponent $\alpha(x_0)$ of a function f at the point x_0 may be defined as the largest exponent such that there exists a polynomial $P_n(x)$ of order n satisfying

$$|f(x) - P_n(x - x_0)| \leq C|x - x_0|^\alpha , \tag{2.36}$$

for x in a neighbourhood of x_0 (Bacry et al. 1993). The polynomial P_n corresponds to the Taylor expansion of f around x_0. Thus,

$$\begin{aligned} |f(x) - f(x_0) - \frac{1}{1!}\frac{df}{dx}\Big|_{x_0}(x - x_0) - \frac{1}{2!}\frac{d^2f}{dx^2}\Big|_{x_0}(x - x_0)^2 - \cdots \\ - \frac{1}{n!}\frac{d^nf}{dx^n}\Big|_{x_0}(x - x_0)^n| \leq C|x - x_0|^\alpha . \end{aligned} \tag{2.37}$$

One can interpret higher exponents α as a smoother function f, as it is easy to see from Eq. (2.37) that f is n times differentiable at x_0 but not $n + 1$ times, if $\alpha \in]n, n + 1[$.

Wavelets can be seen as general partition functions. A naïve ansatz to generalise Eq. (2.16) would be

$$I(q, a) = \int |W_\psi[\mathscr{Y}](x, a)|^q \, dx . \tag{2.38}$$

The structure function method may be seen as a special case of this approach with analysing wavelet

$$\psi(x) = \delta(x+1) - \delta(x). \tag{2.39}$$

The wavelet transform parameter a plays the role of the scale parameter ℓ in the structure function Eq. (2.31). The translation parameter b shifts the wavelet over the whole data set.

The problem with Eq. (2.38) is that it suffers the same problems as the structure function method. Nothing prevents the integrand from vanishing at some points. Therefore the integral diverges for $q < 0$. As a solution for this problem it was proposed (Muzy et al. 1991; Mallat and Hwang 1992) to take only the maxima of the integrand

$$\tilde{I}(q,a) = \sum_{\ell \in \mathscr{L}(a)} \left(\sup_{(x,a') \in \ell} |W_\psi[\mathscr{Y}](x,a')|^q \right). \tag{2.40}$$

The mass exponent $\tau(q)$ can be estimated via

$$\tilde{I}(q,a) \propto a^{\tau(q)}. \tag{2.41}$$

For the determination of the $f(\alpha)$ spectrum the relations given by Chhabra and Jensen (1989) (cf. sec. 2.2) are used:

$$f(q) = -\lim_{a \searrow 0} \frac{1}{\log a} \sum_{\ell \in \mathscr{L}(a)} \hat{W}_\psi[\mathscr{Y}](q,\ell,a) \log \hat{W}_\psi[\mathscr{Y}](q,\ell,a) \tag{2.42}$$

$$\alpha(q) = -\lim_{a \searrow 0} \frac{1}{\log a} \sum_{\ell \in \mathscr{L}(a)} \log \left| \sup_{(x,a') \in \ell} W_\psi[\mathscr{Y}](x,a') \right| \hat{W}_\psi[\mathscr{Y}](q,\ell,a), \tag{2.43}$$

with

$$\hat{W}_\psi[\mathscr{Y}](q,\ell,a) = \frac{\left| \sup_{(x,a') \in \ell} W_\psi[\mathscr{Y}](x,a') \right|^q}{\tilde{I}(q,a)}. \tag{2.44}$$

Numerically α and f are estimated by fitting linear curves to a plot versus $\log a$.

Figure 2.5 shows a plot for a wavelet modulus maxima tree from a multiplicative cascade with $p = 0.25$. It displays the local maxima of the absolute value of the

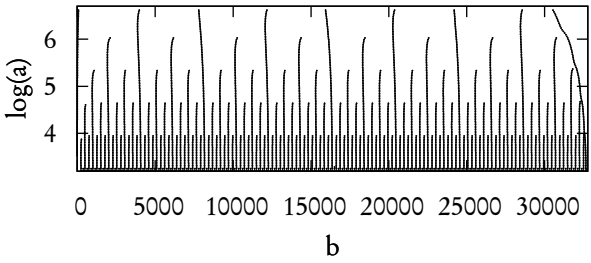

Figure 2.5: Wavelet transform modulus maxima lines for a multiplicative cascade with $p = 0.25$. The lines indicate the local maxima of the absolute value of the cascade's wavelet transform. The wavelet used was DOG1.

wavelet transform. The self similar structure of the multiplicative cascade can be very well perceived except for one irregularity on the right which may be due to finite size effects. However, numerically small errors may occur and yield false maxima lines with very small values. This is no problem for $q > 0$ but for $q < 0$ these errors are emphasised. Thus, it is necessary to set a reliability threshold and set all values below it to 0. We set the threshold to 10^{-10} in this work. This should be reasonably low to avoid cutting valid values, yet high enough to wipe out the numerical errors. Using this result for equations (2.43) and (2.42), Fig. 2.6 is obtained. For every moment q a straight line has to be fitted to the semi-logarithmic plots in order to get estimates for $\alpha(q)$ and $f(\alpha(q))$. The inclinations of the fitted lines give an α, $f(\alpha)$ pair for each q which can be used to plot the multifractal spectrum. Equation (2.41) tells us that $\tau(q)$ may be estimated via a $\log a$ vs. $\tilde{I}$ plot. The results are displayed in both panels of Fig. 2.7. It can be seen that the fitting is quite error-prone for negative moments which is reflected in the large error bars. Nevertheless, it can be seen that the estimation matches quite well the theoretical line for $\tau(q)$ for positive moments, but deviates from it for negative moments. This also manifests in the deviation from the expected parabola shape in the left wing of the $f(\alpha)$ curve.

2.3.3 Detrended fluctuation analysis

Another method for estimating the multifractal spectrum of a time series is the detrended fluctuation analysis (DFA) (Peng et al. 1994; Kantelhardt et al. 2002).

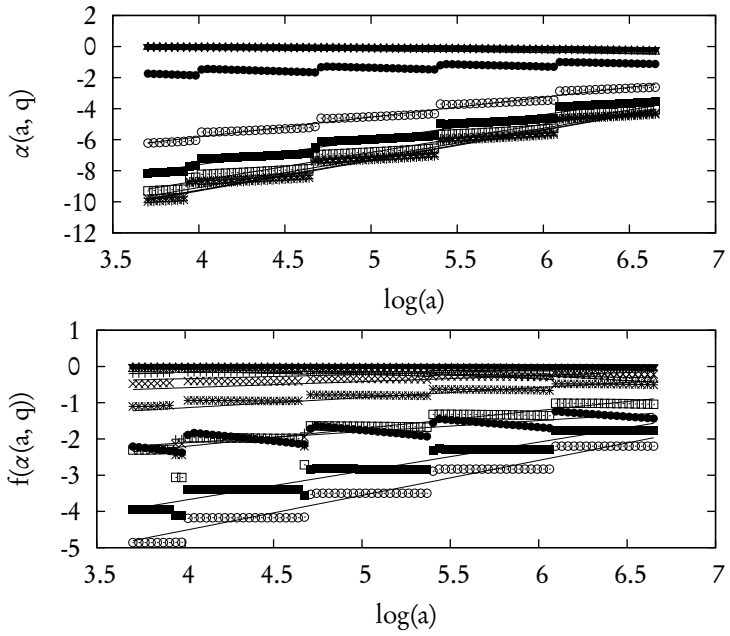

Figure 2.6: Fit of $\alpha(a,q)$ and $f(\alpha(a,q))$. The symbols in both figures discriminate the various values of q. From bottom to top: $q=-5,-4,\ldots,4,5$. The straight lines are linear fits to the curves estimated from the wavelet transform modulus maxima plot.

This method was developed for the analysis of non-stationary time series. Similar to the WTMM method it removes local, polynomial trends from the data.

The method works as follows: suppose we have a time series $\mathscr{Y}=\{y_n\}_{n=1}^N$, then we first integrate its fluctuations to

$$Y(n)=\sum_{i=1}^{n} y_i - \langle y \rangle\,, \quad n=1,\ldots,N\,. \tag{2.45}$$

One has to keep in mind that this step increases the Hölder exponent to be estimated by one. The main idea of the DFA method is to look at the scaling of the local variances of the time series. Therefore we have to divide $Y(n)$ in N_s

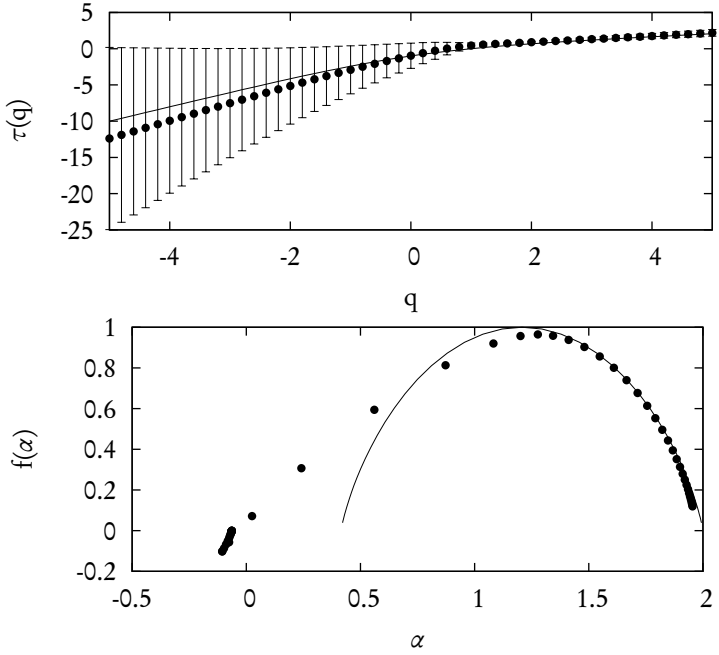

Figure 2.7: Top: Mass exponent τ estimated from a linear fit of $\hat{W}$ against $\log(a)$. Bottom: $f(\alpha)$ spectrum estimated from the linear fits shown in Fig. 2.6. The straight lines denote the theoretical result.

equally spaced, non-overlapping boxes of size s. As the length N of $Y(n)$ is not always a multiple of s, it is desirable to do this procedure from the start and the end of $Y(n)$, respectively. This way $2N_s$ segments are obtained and one takes the optimal advantage of the data length. The next step proceeds by calculating the local variances

$$F^2(\nu,s) = \frac{1}{s}\sum_{n=1}^{s}\left\{Y[(\nu-1)s+n] - p_\nu(n)\right\}^2, \tag{2.46}$$

for each segment ν. p_ν is a M-th order polynomial fitted to the ν-th segment. The method is then called DFAM. Variation of M makes it possible to estimate the order of the underlying polynomial trends within the data set. The right order

is found if the result does not change anymore. As the last step the fluctuation function

$$F_q(s) = \left\{ \frac{1}{2N_s} \sum_{\nu=1}^{2N_s} \left[F^2(\nu, s) \right]^{q/2} \right\}^{1/q} \tag{2.47}$$

is calculated for which holds

$$F_q(s) \propto s^{h(q)} \tag{2.48}$$

(Kantelhardt et al. 2002). Eq. 2.47 is only valid for $q \neq 0$. The limit $q \to 0$ yields

$$\begin{aligned} F_0(s) &= \lim_{q \to 0} \left\{ \frac{1}{2N_s} \sum_{\nu=1}^{2N_s} \left[F^2(\nu, s) \right]^{q/2} \right\}^{1/q} \\ &= \lim_{q \to 0} \exp \left\{ \frac{1}{2N_s q} \log \left[\sum_{\nu=1}^{2N_s} \exp \left[\frac{q}{2} \log \left[F^2(\nu, s) \right] \right] \right] \right\} \\ &= \exp \left\{ \frac{1}{4N_s} \sum_{\nu=1}^{2N_s} \log \left[F^2(\nu, s) \right] \right\}. \end{aligned} \tag{2.49}$$

The scaling exponent $h(q)$ is connected with the mass exponent $\tau(q)$ via

$$\tau(q) = q\,h(q) - 1. \tag{2.50}$$

Thus $h(q)$ may be used with equations (2.23) and (2.24) to calculate the multifractal spectrum

$$\alpha(q) = h(q) - q \frac{dh}{dq} \tag{2.51}$$

$$f(\alpha(q)) = q[\alpha - h(q)] + 1. \tag{2.52}$$

Equation (2.50) does not result from a rigorous proof but is based on analogy assumptions. For the case

$$F^2(\nu, s) = [Y(\nu s) - Y((\nu - 1)s)]^2,$$

that is the standard fluctuation analysis (Peng et al. 1994), the proof is easily obtained by inserting this into Eq. (2.47). Comparison with Eq. (2.22) yields the result.

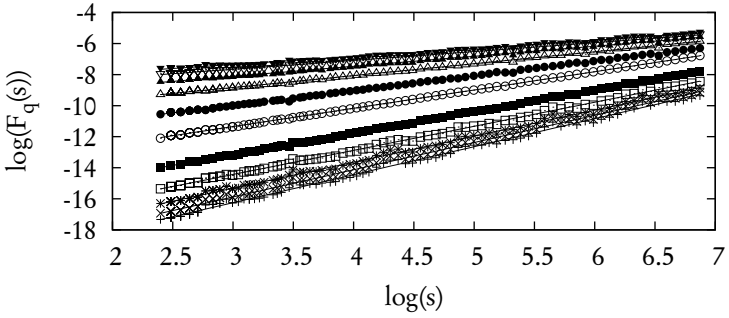

Figure 2.8: Fit of $F_q(s)$. The symbols in both figures discriminate the various values of q. From bottom to top: $q = -5, -4, \ldots, 4, 5$. The straight lines are linear fits to the curves.

However, this is not true for the detrended case. To our knowledge no rigorous proof has been given up to now that shows that Eq. (2.50) is correct. Nonetheless, the results show that the method is suitable for estimating the multifractal spectrum.

In Fig. 2.8 the calculated $F_q(s)$ curves and the fits of straight lines to them are shown. It can be seen that the curves are much more regular than for the WTMM method, which results in lower error bars in the $\tau(q)$ plot shown in Fig. 2.9. For the negative moments the calculated curve fits the theoretical prediction perfectly. For the positive moments the estimation deviates from the analytical calculation. The tails from the multifractal spectral plot also deviate from what is expected. They even violate the monotonicity, although the $\tau(q)$ plot is not so far from the expectation. This is due to the calculation method via equations (2.51) and (2.52). The estimation of the $f(\alpha)$ curve by means of finite differences is error prone.

2.3.4 Comparison

Summing up the results of the estimation of a multiplicative cascade's multifractal spectrum, it can be said that neither method hits the theoretical result perfectly as can be seen in the lower panel of Fig. 2.9. Both the DFA and WTMM method have their major deficiencies in estimating the negative moments. For the positive moments both methods yield satisfactory results. For the DFA the spectral plot is not the optimal way of presentation as it has to be calculated indirectly. The $\tau(q)$

plot gives better results.

In general one can say that the DFA gives the better overall results but the WTMM is more exact at the positive moments. Therefore we decided to use both methods to assure our results.

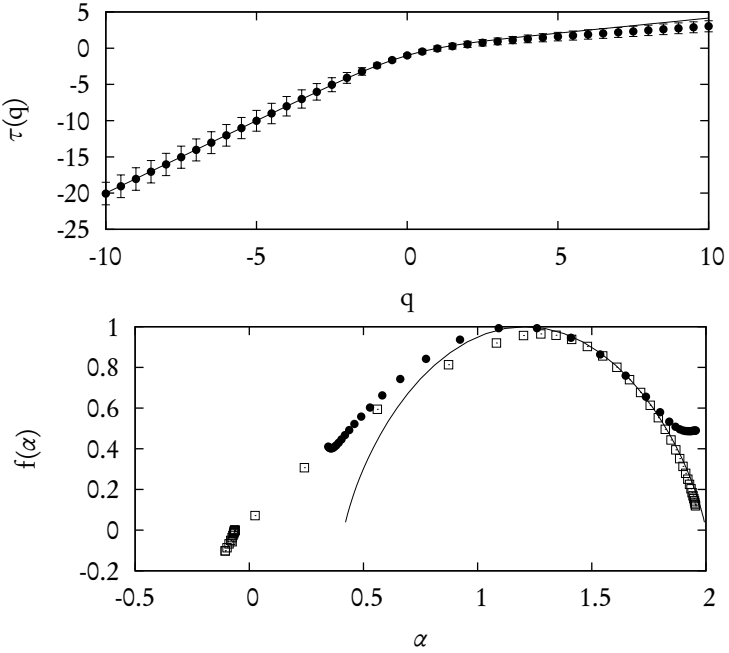

Figure 2.9: Upper figure: the mass exponent $\tau(q)$ of the multiplicative cascade estimated by the DFA method. The points denote the estimation with its error bars, the straight line is the theoretical curve. Lower figure: the points denote the $f(\alpha)$ spectrum calculated with equations 2.51 and 2.52. The solid line is the theoretical curve. The squares show the spectrum estimated with the WTMM method for comparison.

3 Surface analysis of a laser beam melt ablation process

In this chapter we will analyse surfaces generated by a laser beam melt ablation (LBMA) process. This process was developed in the 1980s to replace conventional milling techniques and electro-erosive ablation. The potential advantages of the LBMA technique are enormous especially in the areas of rapid prototyping and tooling. Material processing with the laser is considered to be a key technology due to its extraordinary flexibility. Cutting, welding and hardening are processes where laser technology is already well established (Schubart 1999).

The LBMA has the perspective to extend or even replace the existing toolbox for the creation of forms and depressions. Unlike conventional techniques where the replacement of milling heads is a great expense factor, it has no tool wear. This alone lets the method be of great commercial interest. From the engineering point of view there are many other advantages. It makes the processing of very hard or brittle material possible. Compared to classical milling the diameter of the ablating device may be smaller up to a factor of 50. Additionally, the LBMA has an integrated workpiece hardening due to the thermal processing (Cser et al. 2004).

Unfortunately, at the moment either the quality of the workpiece is poor in terms of roughness or the ablated amount of material is very low (Schubart 1999; Donner et al. 2004; Bube et al. 2006c). The morphology of the remaining surface is highly dependent on the chosen process parameters. It was shown that a great variety of forms observed in experiment may be created by structure formation processes modelled by a convective Cahn-Hilliard equation. This equation describes the phase separation of driven systems. It is dependent on one driving parameter which tunes the emerging structures. Some parameter ranges cause the equation to generate travelling or stationary periodic structures (Golovin et al. 2001). This is the same type of structures also observed on the laser processed surfaces. Unfortunately, the driving parameter is very hard to combine with experimentally adjustable parameters. Therefore a more descriptive approach is

chosen in this work. We derive statistical parameters from the processed surfaces and connect them with the adjustable process parameters.

The aim of the analysis described in the following sections is to find a process parameter window where the process produces a satisfactory workpiece quality in terms of roughness while reaching a reasonable ablation depth and processing speed. This can be considered as an offline control of the process. To achieve this we derive a proper statistical description of the resulting surfaces and connect the description with the process parameters. This research was done in cooperation with Adrienn Cser and Andreas Otto from the university of Erlangen. The experiments and measuring of the surfaces was done by them while the statistical analysis and modelling was done in Oldenburg. The experimental device and the measurement of the process results will therefore only be described shortly in this thesis. More detailed information can be found in the work of Cser (2005).

In the following sections we will first shortly describe the experimental setup we used. Furthermore a description on the statistical parameters normally used by engineers and their application will be shown. While the process takes place the two online parameters laser power and optical emissions are measured. They will be discussed and analysed. As the interplay of processes is too complicated to develop a model which includes them all, we are investigating suitable statistical descriptions to characterise the resulting surfaces and to connect them with the process parameters. This includes simple linear statistics as well as a nonlinear, multifractal characterisation. At the end of the chapter we summarise the results and give an outlook on what further needs to be done in order to extend the offline control to a forced feedback online control. Most of the presented results in this chapter are published in (Rodrigues Neto et al. 2004; Bube et al. 2006c).

3.1 The experimental setup

The term laser beam ablation is a generic term for various processes where the processing may take place in different states of aggregation. The basis is the removal of material as melt or vapour (Hügel 1992). The idea behind the laser beam melt ablation process is quite simple. A high power laser is used to melt a track from the workpiece under the laser. At the same time the melt is continuously blown out by a high pressure gas jet. A sketch of the setup is shown in Fig. 3.1. In most cases it is desired to not only create a thin ridge within the workpiece but to ablate a larger area. This can be achieved by melting a small track, turning

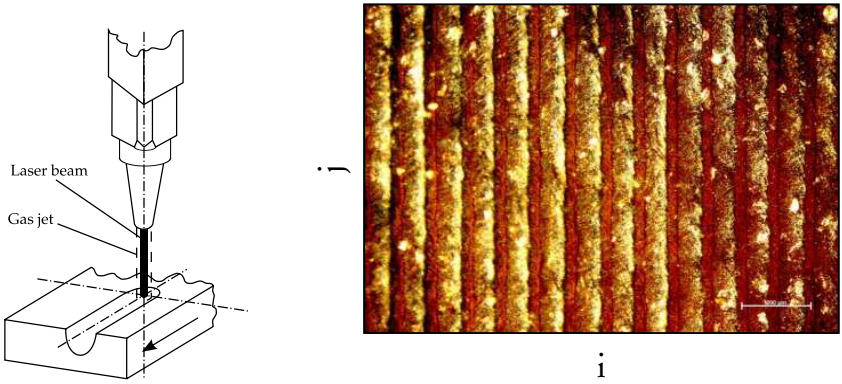

Figure 3.1: Left: Sketch of the laser beam melt ablation process. The workpiece is moved under the fixed laser beam. Attached to the aperture of the laser is a nozzle from which gas is blown out parallel to the laser beam. This gas drives out the molten material. Right: microscope photograph of a sample processed at low line energy. The bar in the lower right corner denotes 200 µm.

the laser off and afterwards melting another track slightly next to the previous one. This can be repeated several times. A resulting surface is shown in Fig. 3.1 on the right. The darker areas are valleys and the brighter ones peaks. In this regime the laser ablation tracks can nicely be distinguished. In Fig. 3.2 microscope photographs of surfaces processed at the same laser power but different material feeding speeds are shown. For the highest feeding speed the ablation tracks can clearly be distinguished. If the feeding speed is reduced and more energy is put into the material a transition regime occurs. The tracks merge and larger valleys and ridges are formed. For the lowest feeding speed large melt pools remain on the surface and join together to form larger structures. The surface gets very rough in this state.

A physical description of the process is very difficult as several processes which influence each other take place in the process. The laser heats the material and the heat diffuses into deeper layers of the material. The external heating of the surface causes a Marangoni instability due to local gradients of the surface tension. Further instabilities are induced by the cooling of the gas jet. Another difficulty for modelling the process is that singularities are introduced by the breakaway of

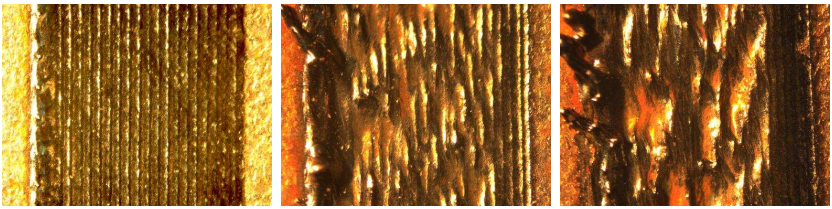

Figure 3.2: Microscope photographs of processed surfaces. The laser power is 550 W in each case. The feeding speed v varies from left to right: 5 m min^{-1}, 3 m min^{-1}, 2 m min^{-1}.

the melt particles.

Several parameters can be changed for the process but only few are suitable to be used as an online control. The gas jet may be varied in direction, intensity and nozzle configuration. Furthermore, several process gases are thinkable. We used compressed air, as this has proven to be a good compromise between the advantages and disadvantages of other possible process gases (Schubart 1999; Cser 2005; Bube et al. 2006c). In later experiments also argon was used, but it turned out that the chemical reactions induced by the oxygen contained in the air are necessary to drive the process. Even a pure oxygen jet was tried to accelerate the process, but this made it uncontrollable (Schubart 1999). The pressure of the gas jet is unsuitable for an online control due to its inertia and turbulence induced unpredictability. Therefore, it is kept constant in our experiments.

The online adjustable parameters are the feeding speed of the material and the laser power, where the laser power is by far the fastest parameter. It can be changed within milliseconds. Nevertheless, in our project the parameters were fixed during the processing phase in order to survey the stationary regimes. Only rudimentary tests were made with oscillating power. Those tests showed interesting emerging structures on the surfaces which it will be a challenge to survey (Cser 2005).

The experiments were carried out using a 5-axis CO_2 continuous wave laser (Trumpf L5000) which is excited by a frequency of 10 kHz, resulting in a maximum output power of 2.2 kW, focused on the material with the focus diameter kept constant at 0.3 mm. During the processing phase two parameters are measured online. The optical emission from the melt is measured by a silicon photo diode (Siemens BPX 65). Läßiger (1995) claims that the acoustic measurement of the emissions is suitable for the process monitoring, but the delay of the sound makes

the measurement of the optical emissions preferable (Sutor 1994). The laser power is measured by a thermopile which is attached to the resonator (see e.g. Zeuner (1994); Brozio (1999)). After the processing took place, the surfaces are surveyed with a laser based triangulation device (by UBM). Figure 3.3, upper panel shows the raw measurement data from a surface. As can be seen, there is a strong trend in the data. This results from the bending of the material as it heats up under the influence of the laser beam. This linear trend is subtracted and the measurement matrix is rotated manually so that the ablation tracks are parallel to the image baseline. Furthermore the unprocessed borders which are also measured were cut from the measurement matrices. This was done by hand for every single surface. It is very important to cut these areas as they disturb the results of further analyses. The border may be very well perceived in Fig. 3.3 by the very high height values. The maximal resolution of the measurement device is 2 μm in planar directions and about 1 μm in depth (Cser 2005).

The experiments were carried out as follows. The laser is switched on and melts a track of about 4.5 cm in length. After finishing this track, the laser is switched to minimal power (20 W), where nearly no heating takes place, moves back to the starting point and is displaced 0.1 mm in perpendicular direction. Then the power is turned on to the processing value and the procedure repeats. The diameter of the laser beam focus is 0.3 mm, thus every track is processed three times. For all experiments commercial low carbon steel (AISI 1008) was used. Throughout this thesis we will denote the processing direction as the j-direction and the transversal direction as the i-direction as indicated in Fig. 3.1.

As already mentioned above, two parameters may be set for the process: the average *laser power* P and the *feeding velocity* v of the processed material. Both parameters control the amount of energy which is brought into the material. The energy per line is

$$\begin{aligned} E_l &= \alpha \frac{P t}{s} \\ &= \alpha \frac{P}{v}, \end{aligned} \tag{3.1}$$

where t is time, s is the length of the processed track and α is the absorption coefficient of the laser radiation in the material. In our case $\alpha \approx 0.1$. Table 3.1 lists a matrix with the combinations of process parameters used for the measurements. Not all possible parameter combinations are experimentally realisable. For exam-

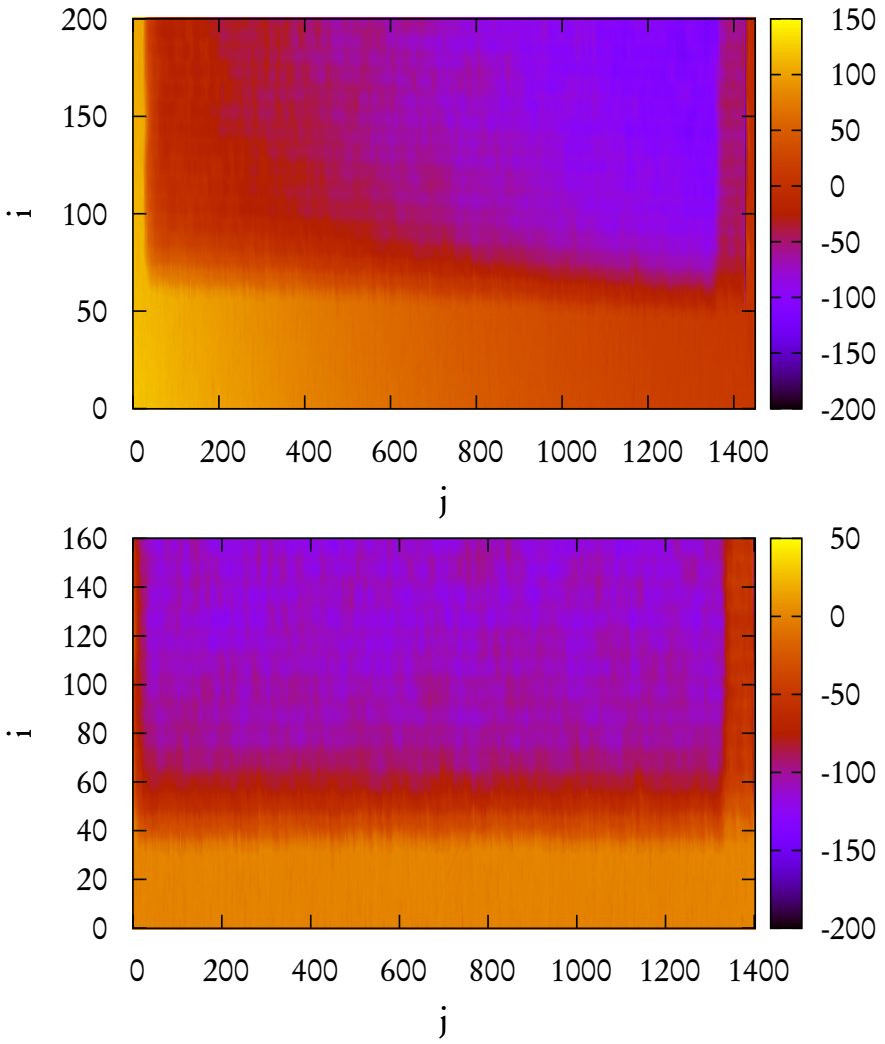

Figure 3.3: Upper panel: raw measurement data from laser triangulation device. Lower panel: measurement rotated so that the tracks are parallel to the baseline. The bending of the workpiece due to the heating is also corrected.

	550 W	660 W	770 W
2 m min^{-1}	X		
3 m min^{-1}	X	X	
4 m min^{-1}	X	X	X
5 m min^{-1}	X	X	X
6 m min^{-1}	X	X	X
7 m min^{-1}	X	X	X
8 m min^{-1}		X	
9 m min^{-1}		X	

Table 3.1: Combinations of process parameters used in the experiments.

ple if the line energy is too high, the workpiece heats up too much and deforms. On the other hand, if the line energy is too low no ablation takes place at all. The pressure of the air jet was kept constant at 2 bar in all experiments.

3.2 Linear analyses

In this section we measure linear features of the online measured data and the surfaces. In order to develop an online control for the ablation process it is important to find some relations between the online measured data and the measured surfaces. Unfortunately it turns out that the online measured data is completely unusable for this purpose.

3.2.1 Online measured signals

The online measured signals are the current power of the laser and the optical emission from the melting zone. In Fig. 3.4 an example of a measurement pair for a processing run is shown. Especially the time series for the laser power looks false at first sight. Even if the laser is switched off, the measured power does not decrease immediately to a very low value, but it drops off and then continues to decrease linearly. The same is true for the processing phase. The measured power jumps to a high value and then linearly increases instead of remaining on the same level. Obviously this is a flaw in the detector. The most probable explanation is that the

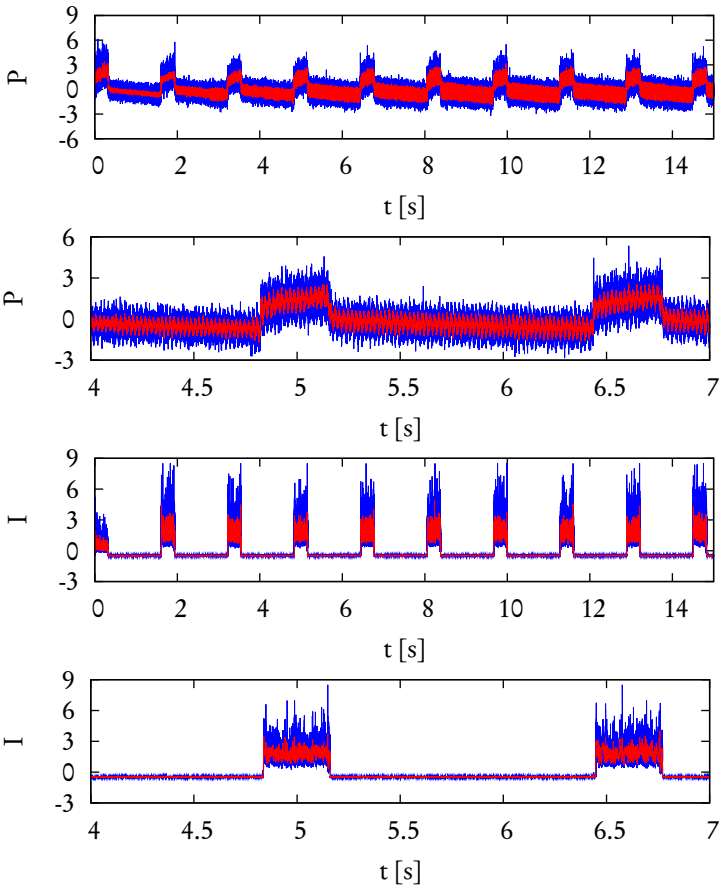

Figure 3.4: Online measurements of process properties. The first two plots show the measurement of the laser power, the second plot is a magnification of the first. The last two plots show the optical process emissions. In blue are the raw data, in red is the data smoothed by a moving average filter with window size 20. The process parameters were 550 W at 5 m min^{-1}. The data is normalised to zero mean and variance one.

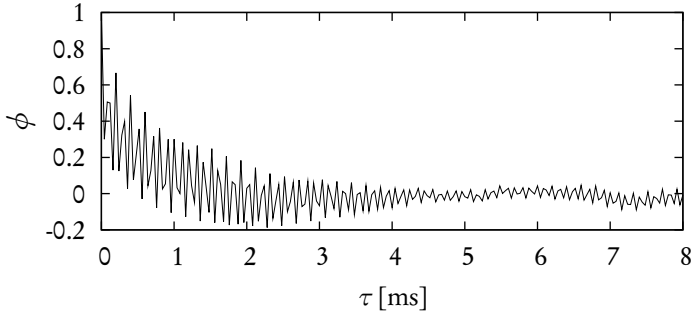

Figure 3.5: Autocorrelation function of a optical emission signal during processing phase.

thermal drift within the detector is too strong and destroys the measurement (Cser et al. 2004).

For the measurements of the optical emissions from the melt it can be seen that they are quit spiky. The spikes result from the fact that the melt particles that are blown out by the gas jet fly around the workpiece. Some fly near the photo diode and cause a spike. Nevertheless, we did some analysis of the data. A method to test for periodicities in the data is the autocorrelation function

$$\phi(\tau) = \frac{1}{N\sigma^2} \sum_{i=\tau+1}^{N} (y_i - \langle \mathscr{Y} \rangle)(y_{i-\tau} - \langle \mathscr{Y} \rangle), \tag{3.2}$$

where σ^2 is the variance of the time series $\mathscr{Y}$. The result for the second peak (ie. the second track) shown in Fig. 3.4 is displayed in Fig. 3.5. It can be seen that the correlation drops to zero after less than one millisecond, thus indicating no distinguished periodicities. What is more remarkable is that the autocorrelation function is modulated by two sines. The period of the one sine is about 0.1 ms and the other about 0.2 ms. This is easily understood by considering the fact that the sampling frequency of the optical device is 25 kHz and the laser pumping frequency is 10 kHz. Therefore the modulation of the autocorrelation function is an aliasing effect.

Considering these results we refrain from a further investigation of these data. Ref. (Cser et al. 2004) contains some more results from the analysis of the online data including results from another laser device, where the faulty power detector

is replaced. The new device does not show the aliasing effect anymore. The Fourier spectrum of the laser signal does not show any dominant frequencies but the characteristics of $1/f$ noise. The autocorrelation functions drop very fast. The emission signal possesses two dominant frequencies at 20 and 40 Hz which could not be assigned. The problem is that these features could not be found in the characteristics of the surface. In order to develop a suitable online control it is necessary to connect the properties found for the online measured signals with properties of the surfaces depending on the process parameters. The optical emission signal is expected to play a key role here, as it reflects the procedures happening on the surface. This should allow the control mechanism to directly react if the surface gets into a critical state where the roughness increases. We were not able to find such a feature of the emission signal which allows a connection to the surface. Another requirement for an online control is that the searched feature is not a global value like fractal dimension and the like. Such measures require the whole time series to be present to be calculated, but at processing time one has only the present measurement and the past measurements, which are only a few at the beginning. A mapping from the online signals to the state of the surface is needed. We did not succeed in finding this. Maybe such a mapping can be found by nonlinear correlation tools or black box modelling techniques like cellular automata.

3.2.2 Surface analysis

As the online control of the process is still out of reach, we want to stick with an offline control. This means that we find out a suitable process window where acceptable results can be achieved. We do not want to only do a trial and error search in the parameter space but find regularities and predict results. Before this can be done we need a suitable mathematical description of the surfaces, one statistical parameter or a small set of parameters which can be connected with the process parameters feeding speed and laser power.

In order to get a statistical characterisation of the processed surfaces, we need some measures to describe them. A measure often used by engineers is the *arithmetic mean roughness* R_a, which is simply given by

$$R_a = \frac{1}{NM} \sum_{x=1}^{N} \sum_{y=1}^{M} h(x,y), \tag{3.3}$$

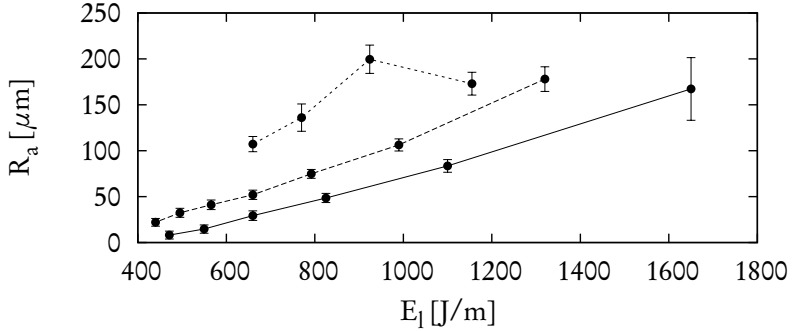

Figure 3.6: Arithmetic mean roughness R_a for some samples taken from processed low carbon steel. For every parameter set three samples were produced. The lines connect samples which were processed with the same laser power: solid: 550 W; long dashes: 660 W; short dashes 770 W.

where $h(x,y)$ is the height at location (x,y), i.e. R_a is the mean value of the profile heights (DIN 4287). In Fig. 3.6 the roughness of some processed steel surfaces are plotted against the selected line energy. The lines connect samples which were processed with the same laser power. It can be seen from the plot that the generated roughness is not dependent on the energy per line alone, but the laser power and the feeding speed have to be regarded separately. In nearly all cases the roughness increases monotonously with the line energy. One exception is for very high laser power and low feeding speed. There the roughness decreases again. There are two possible reasons for this phenomenon. On the one hand, initial evaporation processes consume more energy and therefore the laser can melt less material. On the other hand, the higher laser power melts more material which cannot be removed completely by the gas jet. The remaining melt leads to a smoothing of the surface as larger pools join together and are smoothed by the surface tension (Bube et al. 2006c). However this question could not definitely be solved. A hint on the surface quality can be extracted from the standard deviation of the roughness. The standard deviation tells us how reproducible the results are. Smooth surfaces have in general a good reproducibility and therefore a low standard deviation. Surfaces which form large structures or where even melting drops remain on the surface have a bad reproducibility as those events are random and different in each realisation. In that sense a low laser power and a low feeding

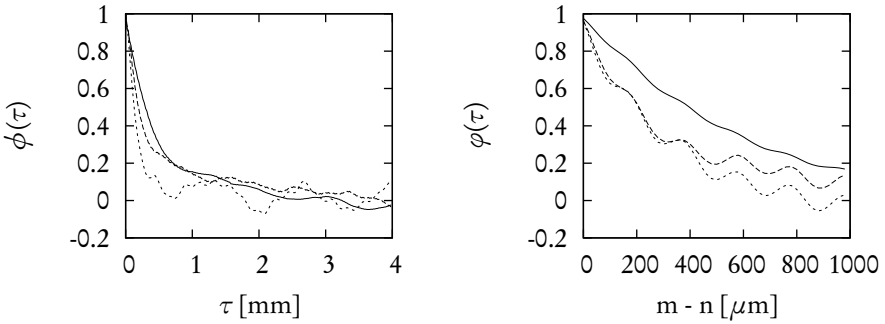

Figure 3.7: Left: mean autocorrelation along the processing tracks. Right: average correlation coefficient versus the distance of the tracks. Solid: E_l = 1320 J m^{-1} (v = 3 m s^{-1}, P = 660 W); long dashes: E_l = 792 J m^{-1} (v = 5 m s^{-1}, P = 660 W); short dashes: E_l = 825 J m^{-1} (v = 4 m s^{-1}, P = 550 W).

speed give the worst results. The reason may be that in contrary to higher laser power and higher feeding rates, lots of material is molten and all is driven out by the gas jet at once. What seems to be desirable at first, turns out to give very bad results. The irregular removing of the melt particles forms a surface of ridges and valleys. Thus it seems to be important that some of the melt remains and smooths the remaining surface by its surface tension.

We have looked at the autocorrelation functions of the process' optical emission signal. Therefore it is also interesting to get the same information on the surface. For each measurement track we have calculated the autocorrelation function and averaged over all functions. From Fig. 3.7 left we see that the correlations depend on the process parameters. Within 200 to 600 µm the autocorrelation drops to $1/e$, where for higher line energies longer correlations occur and vice versa. This can be understood by the larger structures that are created for higher line energies. For small line energies the appearing structures remain local and small. The shortness of the correlation length indicates that there are no periodic structures or they are at least hidden by strong stochastic influences (Bube et al. 2006c). Furthermore it turns out that the correlations within the optical emission signal should have been much longer, in order to correspond to the correlations on the surface. For example at a feeding speed of 3 m/min, a correlation length of 200 µm for the surface would correspond to a correlation length of about 10 ms for the optical

signal. Therefore it follows that the disturbances in the signal are either too strong to preserve the information in the signal or that the surface is still in motion after the detector already moved on. In the latter case the detector is not able to measure the structures online. Maybe a lag behind the laser would help, but it is questionable if the optical signal is still strong enough in that case.

A very important point for a control of the process is the question how the disturbances in one track influences the succeeding ones. A linear measure to quantify this is the correlation coefficient

$$\varphi(m,n) = \frac{\langle S_{m,j} S_{n,j} \rangle}{\sqrt{\langle S_{m,j}^2 \rangle \langle S_{n,j}^2 \rangle}}, \tag{3.4}$$

where $S_{i,j}$ is the height of the surface measured at i, j. We average over j. Thus with the coefficient $\varphi(m,n)$ we measure the correlation between track m and n. In Fig. 3.7 right the interesting result is shown for some example surfaces. For higher line energies the influence between the tracks is rather long, over the distance of about seven tracks the correlation coefficient stays above $1/e$. The explanation is the same as for the intertrack correlations. The structures get larger and range over more tracks. This can nicely be seen on the photograph in Fig. 3.2. The surfaces processed with a smaller line energy do not have structures which range over various tracks. Here the tracks can still be distinguished after processing. It can be seen, that the correlation drops below $1/e$ after about 400 µm. This is the length where the overlapping of the tracks is gone. We remember that every track is processed three times. The laser beam diameter is 300 µm, whereas its disposition after finishing the track is only 100 µm. Here we also have the explanation for the eye-catching oscillations in the curves for the lower line energies. Their period is 100 µm, which is exactly one track. Thus this measure nicely reproduces the track structure.

A measure often used in turbulence analysis is the analysis of the shape of the power density functions (PDF) of increments (Frisch 1995; La Porta et al. 2001; Jun and Wu 2005). In the turbulence case these are mostly velocity increments. This measure gives insight in the occurrence of intermittent phenomena by comparing the distribution with Gaussian distributions. We transfer this method to our surfaces. We analyse the increments of profile heights

$$\Delta S = S_{i,j} - S_{i,j-s}, \tag{3.5}$$

where s is a space lag. s may also be considered as a scale parameter. The smaller

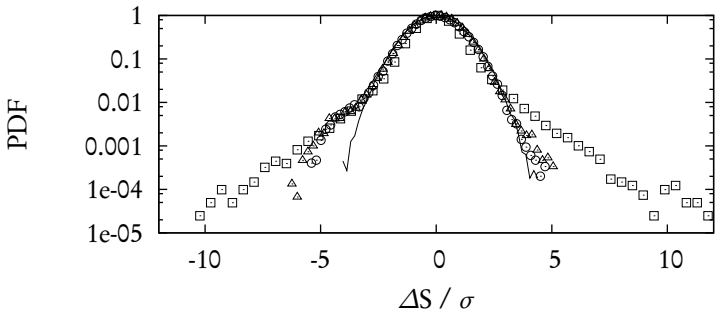

Figure 3.8: Probability density function of the surface heights. The parameters of the process were $v = 3\ \mathrm{m\,s^{-1}}$ and $P = 550\,\mathrm{W}$. The symbols mark different scales s. Squares: $s = 1$, circles: $s = 10$, triangles: $s = 100$. The solid line is the PDF of a "surface" of Gaussian distributed random numbers with $s = 1$. The x-axis is in units of the standard deviation in order to make the plots for the different scales comparable. The maxima are normalised to 1.

it is, the smaller spatial structures are surveyed. In this analysis one is interested in the deviations of the PDF from the Gaussian PDF shape. The plots are mostly displayed in semi-logarithmic style with the maxima normalised to 1 and the x-axis in units of the standard deviation (see Fig. 3.8). In this style Gaussian distributions are upside-down parabolas. If the PDF possesses wings – so called *fat tails* – thus showing a higher probability for extreme events than it would be expected for a random process, the process is called *intermittent*. These intermittent phenomena may be peculiar for different scales. This is reflected in the scale parameter s in equation (3.5). The shape of the PDF is also somewhat connected with the structure functions. If the PDF decays algebraically i.e. $p(x) \propto x^{\alpha}$, then moments

$$\int p(x) x^m \, dx = \int x^{\alpha} x^m \, dx \tag{3.6}$$

exist only for $m < \alpha$.

Figure 3.8 shows an example for a PDF of a surface processed with the LBMA method. It can be seen that the plots have the characteristic fat tails and differ significantly from the plot for the random surface. The latter shows the characteristic parabola shape of a purely random distribution. On small scales the deviation

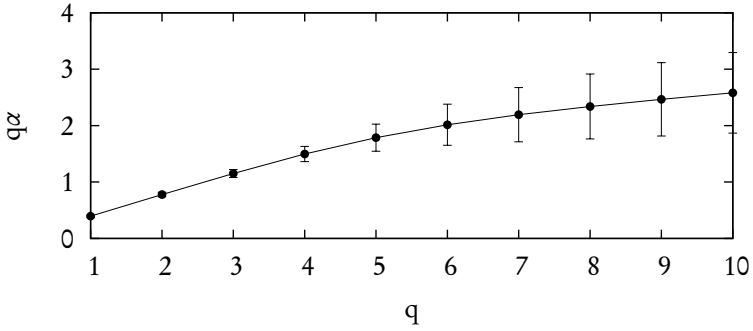

Figure 3.9: Structure function of the surface heights. This is an average over three samples processed with 550 W at 3 m min^{-1}.

from the Gaussian distribution is stronger. That means intermittent events occur more often on small scales. For larger scales the distribution converges to the Gaussian. This behaviour can be observed for all surfaces we analysed.

Intermittency is often connected with fractality. A prominent example for a fractal set with intermittency is the devil's staircase (Frisch 1995). This is the integrated signal of the Cantor set already discussed in section 2.2. The devil's staircase is almost everywhere constant, that is its (uncountable) infinitely many singularities have Lebesgue measure 0. Imagine a box of length ℓ positioned on the devil's staircase. As ℓ gets smaller, the number of singularities within the box is more and more dependent on the box's position. It is characteristic for an intermittent set, that its singularities are rare. A counterexample for a non-intermittent set is a (Gaussian) random walk. Here it does not matter where the box is positioned the number of singularities is always infinite.

We applied the structure function approach already discussed in section 2.3.1 as a first simple test for fractality in the surface height measurements. For a fractal set α is the same for all q. In the case of a multifractal it is different for all q. We averaged over ten measurement tracks in transversal ablation direction in order to suppress fluctuations and calculated the structure functions for the remaining track. The ten tracks were chosen far away from the transition region. We now applied Eq. (2.31) and calculated $q\alpha_q$ from the inclination of a $\log\langle y_n^q\rangle$ vs. $\log\ell$ plot. The result for a selected surface is displayed in Fig. 3.9. It can clearly be seen that the q vs. $q\alpha$ plot is nonlinear which is a sign for a multifractal set. All surveyed samples

exhibit this behaviour. It can also be seen that the errors grow for larger exponents q. This is not surprising as rare but extreme events are emphasised with larger weighting exponents. In order to access negative moments, more sophisticated methods are necessary. We will elaborate on this in the next section.

3.3 Nonlinear analyses

As we saw in the previous section the surfaces of the processed workpieces exhibit nonlinear scaling functions and show signs of intermittency. This information motivates us to use measures of multifractality. In section 2.3 we already introduced some methods which we will now apply to our measured surface data.

We stick to a one dimensional analysis of the data. The surfaces are analysed trackwise where we average over ten measurement tracks in order to suppress noise influences. The one dimensional analysis is justified by the geometry of the problem. The surface is highly anisotropic and we are interested in the height geometry in ablation direction. Our analysis have shown that the first few tracks represent a transient regime due to the heating of the material. After those few tracks the process becomes stationary and the results reproduce for the subsequent tracks.

3.3.1 Wavelet transform modulus maxima method

The first method we applied to our surface data was the WTMM method. This method is theoretically very well reasoned but practically quite tricky to apply (Struzik 1998; Haase and Lehle 1998; Oświęcimka et al. 2006). Especially the crucial extraction of the maxima is subject to numerical pitfalls. It is necessary to set a reasonable threshold in the maxima tree (cf. Fig. 2.5) in order to cut untrusted points below it. Nevertheless it is very elegant and efficiently computable.

The first task to apply the method is to choose a wavelet function. This is important for the polynomial trend order which is removed from the data. We chose the first derivative of the Gaussian function (DOG1). This wavelet removes trends up to (but not including) first order polynomials. We also used other orders but the results remained qualitatively the same.

A more difficult question is that of the fitting range of equations (2.42) and (2.43). Normally the fitting range is chosen more or less by eye for each data set. This is impractical for the amount of data sets we are using. We just choose the range

for some randomly picked sets and use it accordingly for all other sets in order to make them comparable. Adjustments are only made in very few exceptional cases if the results are obviously wrong. In our analyses we averaged over ten measurement tracks far from the first track in order to skip the transient region. This means we analyse one dimensional data. Attempts were made to extend the WTMM method to two dimensions (Arnéodo et al. 2000; Decoster et al. 2000), but tracking the maxima lines in the three dimensional maxima space is numerically very challenging. This possible refinement of our results has been deferred in favour of the promising results achieved with the one dimensional analysis.

In Fig. 3.10 we can see the start and the end of the fitting range that we choose for our analysis indicated by two vertical dashed lines. This was found to be at 5 to 6.8 $\ln \mu$m. For the WTMM method the fitting range could be chosen larger, but this was neglected in order to keep comparability with the DFA method which shows a shorter fitting range (Bube et al. 2006c). This means the scaling describes structures of the size from about 80 to 183 μm. For the WTMM alone the scaling region could be chosen up to 8 $\ln \mu$m before the plots saturate because of the finiteness of the data set. However, using the full range does not change the results qualitatively but only improves the reliability, which is not a bad thing at all, but we prefer the comparability in this study.

Fig. 3.11 shows the multifractal spectrum estimated by the WTMM method for four line energies. The laser power was kept constant at 660 W. It can be seen that the error bars on the right wings of the spectra are drastically larger than for the left or the middle parts. This simply reflects the fact that this part is estimated via the negative exponents q, which emphasise smaller fluctuations. This is also the scale where numerical instabilities take place. These instabilities are "random" and cause bad fittings. The left wings are estimated with the higher exponents q. In this case the effect is reversed and the noise is suppressed. On the other hand for very high q large number problems occur. The best results in the sense of reliability are obtained around $q = 0$. For this exponent $f(\alpha)$ must be equal to 1 as this is the dimension of our data set's support. We can see that our experimental results fulfil this requirement well within the error bars.

It can be seen that the multifractal spectra are ordered by the line energy. The higher the line energy the higher are the Hölder exponents. This is true for both the maxima and also for most of the ends of the wings. This behaviour is observed for all surveyed surfaces.

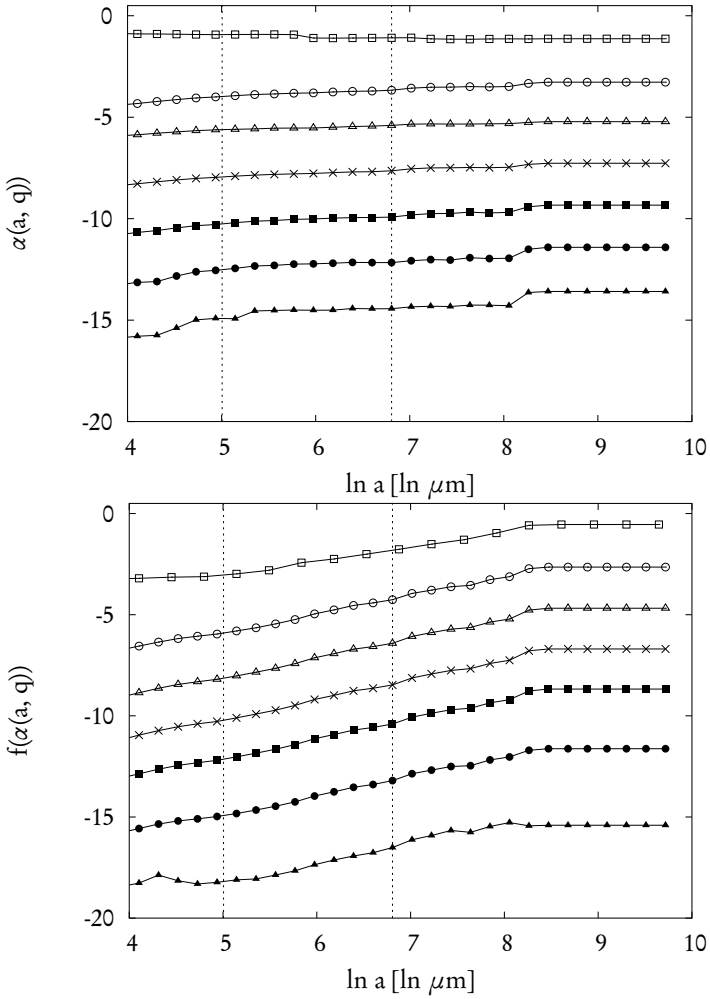

Figure 3.10: Fitting of α and $f(\alpha)$ from linear fits within the range between the dashed vertical lines. In both panels the surface used was processed with $v = 8$ m/min at $P = 660$ W. From bottom to top the moments are $q = -4$, -2, -1, 0, 1, 2 and 4.

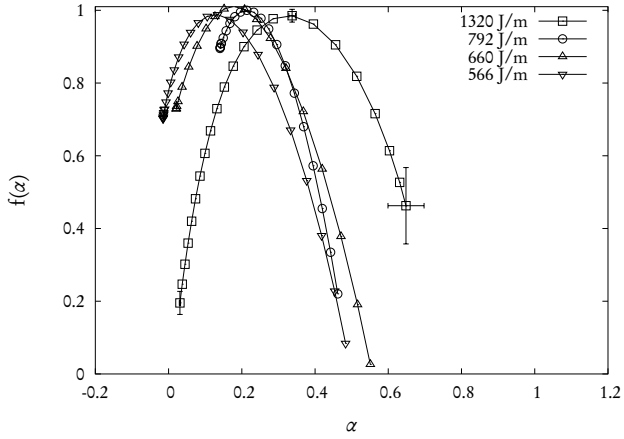

Figure 3.11: Multifractal spectrum of surfaces processed with $P = 660\,\mathrm{W}$ and varying feeding speeds estimated by the WTMM method. In each plot three error bars are indicated in order to give an idea on the reliability. Constant trends were removed from the data by using DOG1.

3.3.2 Detrended fluctuation analysis

We want to test the reliability of the results gained in the previous section with another multifractal estimation method, the detrended fluctuation analysis (DFA). This method is much easier to implement and does not require much numerical tuning. However, the method is not so well reasoned theoretically as the WTMM method which is a direct application of generalised thermodynamics (Tsallis 1988; Arnéodo et al. 1995). The method is often used for the analysis of long range correlations (Koscielny-Bunde et al. 1998, 2006; Rybski et al. 2006). This is controversial and has raised concerns. Maraun et al. (2004) showed that it is possible to generate autoregressive processes where the DFA falsely detects long range correlations. However, we use this technique only to characterise our surfaces and avoid conclusions on long range correlations as our data sets are much too short to allow this.

The DFA method relies on making a linear fit to the plots of equation (2.47). Often this is not so trivial as the function is spiky or oscillates. An attempt to overcome this deficiency has been made by replacing the polynomial fit term in

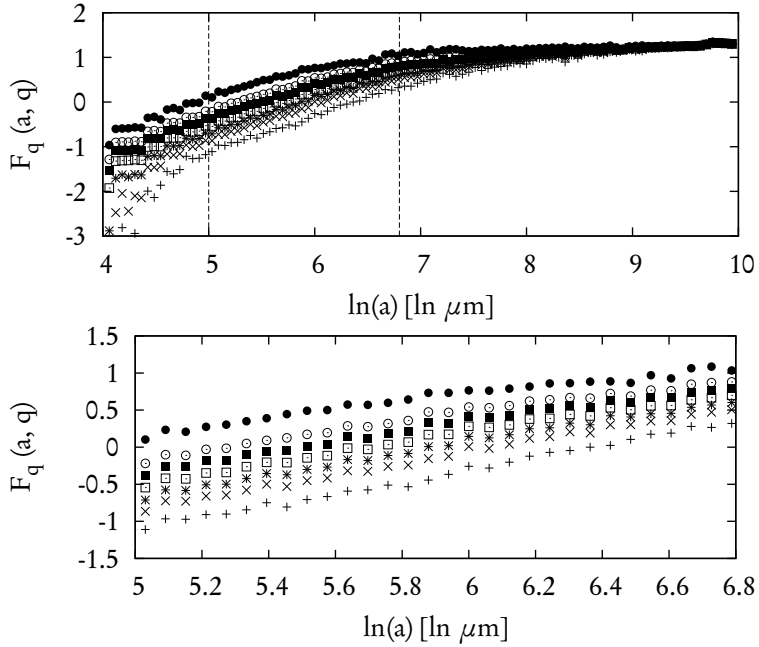

Figure 3.12: Fitting of $F_q(a,q)$ linear fits within the range between the dashed vertical lines. The surface used was processed with $v = 5$ m/min at $P = 550$ W. From bottom to top the moments are $q = -4$, -2, -1, 0, 1, 2 and 4.

equation (2.46) by a moving average fit (Alessio et al. 2002; Alvarez-Ramirez et al. 2005). However, it seems that this method only works for the estimation of Hurst exponents in random signals and is therefore unusable for our applications.

Now we come to the results for the analysis of the surfaces generated by the laser beam melt ablation process. In Fig. 3.12 we see the choice of the scaling range for the estimation of the multifractal spectrum. In the upper panel it can be seen that the F_q plot saturates much faster than the $\alpha(a,q)$ and $f(\alpha(a,q))$ plots for the WTMM method. Therefore, only a smaller scaling range can be chosen. The magnification of this range is displayed in the lower panel of Fig. 3.12.

In Fig. 3.13 we see the example of a multifractal spectrum estimated by the DFA method. All spectra in this figure are calculated from surfaces processed with a

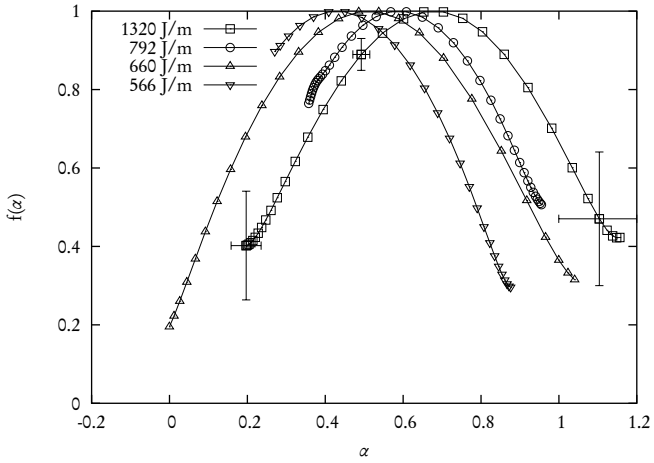

Figure 3.13: Multifractal spectrum of surfaces processed with $P = 660\,\mathrm{W}$ and varying feeding speeds estimated by the DFA method. In each plot three error bars are indicated in order to give an impression on the reliability. Constant trends were removed from the data by subtracting fitted polynomials of zeroth order.

laser power of $P = 660\,\mathrm{W}$, like in the example for the WTMM method shown in Fig. 3.11. The spectra are ordered by the line energy. The tails and maxima of the spectra calculated from tracks processed with lower line energy lie at smaller α than those processed with higher line energy. The errors for the spectrum estimation are higher at the tails. At the maximum the estimation is very reliable.

3.4 Summary and Outlook

Figure 3.14 shows the results for all surfaces analysed with both the WTMM and the DFA methods. Displayed is the location of the Hölder exponents α of the multifractal spectra at the wings' extrema and the position of $q = 0$ in dependence on the line energy. Both methods show an increase in the central Hölder exponent (the one for $q = 0$ with the maximum $f(\alpha)$) towards more persistent behaviour with increasing line energy, for all plots, but for 770 W of DFA, where the tendency

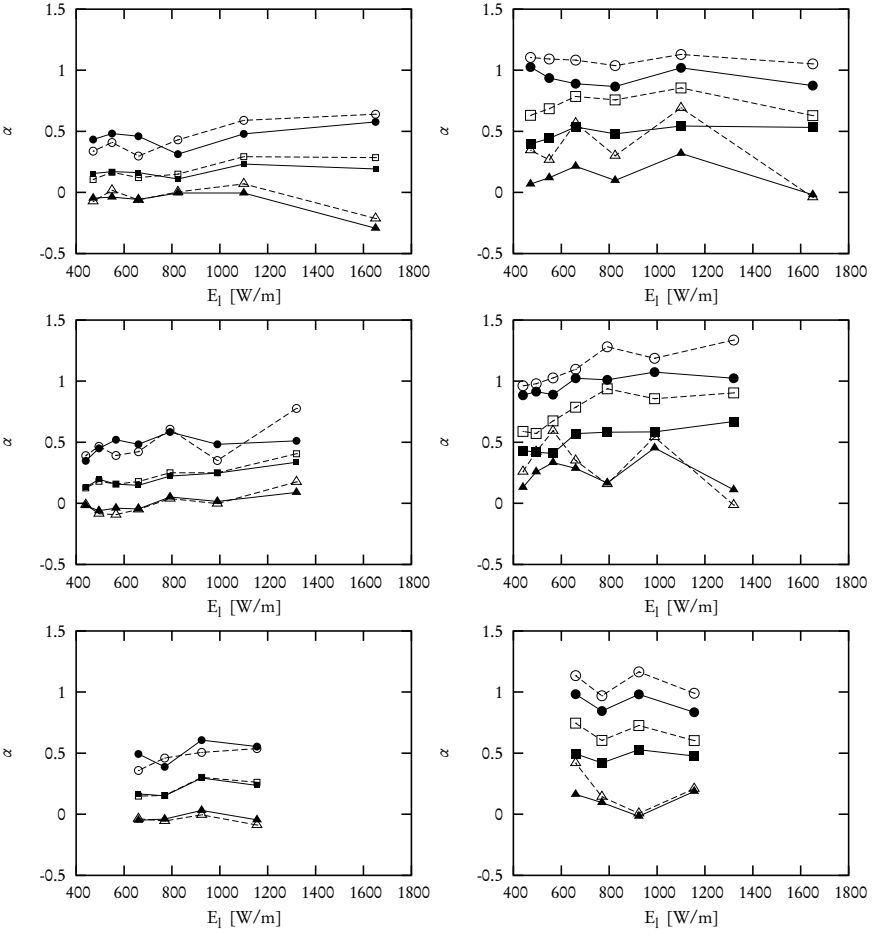

Figure 3.14: Multifractal spectrum extrema points against line energy; in each plot, triangles, squares and circles denote, respectively, minimum, medium and maximum values of α. Bold symbols are for constant trends removed, while open symbols for first order trends. Left plots: Hölder exponents of the surfaces estimated with the WTMM method, right plots: with the DFA method; from top to bottom: laser power is 550, 660 and 770W.

is not evident. The most notable difference in the results appears for the spectra width in all laser powers. Furthermore, one can observe a shift in the Hölder exponents of about 0.3 between the two methods. For both methods the removal of higher order trends results in a shift towards higher Hölder exponents.

In theory one would expect that both methods yield the same results. We checked our implementations with standard examples such as the devil's staircase (a monofractal) or the binomial multiplicative cascade (a multifractal) (Feder 1988) and found that this is really the case for those analytical examples. Also the fitting ranges are exactly the same and everywhere smooth. For the analysed surfaces this expected coincidence of the results from both methods cannot be found. The linear regions and therefore the fitting ranges differ. This shows us that one needs to be very careful when applying these methods to short measured real world data. The differences in the results have their origin in the different convergence speed to the real result.

The fact that the multifractal spectra shift towards higher Hölder exponents for higher line energies is consistent with what one observes by visual inspection of the surfaces. For these high energies large patterns evolve as the melt pool becomes larger and the surface tension smoothes the surface before it solidifies. The analogy with the fractional Brownian motion holds in the sense that the standard deviation diverges faster for higher Hölder exponents. This is confirmed by the linear analysis.

Our analysis provided many new insights into the properties of the surfaces created by a LBMA process. We observe a strong influence of linear processes perpendicular to the ablation direction. The overlapping of the ablation tracks manifests clearly in the linear correlation function. By contrast, in the ablation direction nonlinear processes dominate the formation of surface structures. Linear correlation drops very fast and both of our applied nonlinear methods detect a pronounced multifractal spectrum. We also see that the WTMM and DFA, although producing equal results for mathematical systems, give different quantitative results. Nevertheless, qualitatively we obtain the same results with both methods, namely that the persistence of fluctuations in the data series increases with the line energy. However, no conclusion can be drawn on the kind of any possible long range correlation in the data as the difference between the results of the two methods is too large. This could be expected if one recalls the available data length.

The analysis also shows that the line energy which is frequently used by engineers is not a correct order parameter, but one has to consider feeding velocity and laser power separately. This is confirmed by the global parameter of the surface

roughness as well as by the characteristics of the Hölder exponents. The surface characteristics described by the multifractal measures are in good agreement with the properties that can be observed by visual inspection. They are therefore a suitable tool to translate the surface properties into a mathematical description.

Our results also show that the process is highly anisotropic. We have strong nonlinear influences in the processing direction, while in the transversal direction the process is dominated by linear effects.

In this thesis we showed that an offline control of the process is possible. We connected the surface quality with the mathematical construct of multifractals and showed that a connection of this quantity with the process parameters exists. The parameter line energy, which is a combination of the laser power and the feeding speed is misleading as it was shown that the surface quality varies if this parameter is kept constant but its components are changed. From our results we can conclude that laser powers above 660 W are not useful as new processes are introduced which make the process more unpredictable. Also feeding speeds above $5\,\mathrm{m\,min^{-1}}$ are not helpful as the ablation rates are too low to be useful. For other process regimes an online control has to be developed which establishes a feedback control of the process. The already established online measurement parameters optical emission and laser power do not seem to be of very much help. Especially for the optical emission it is doubtful if it is the right quantity to give insight into the development of the surface during the process.

An online control requires either a fundamental understanding of the physical processes going on so that a process model can be established. This was successful for example at the process of laser drilling. In order to succeed in this it is necessary to separate the mixture of processes that take place during the ablation. This has to be done by examining the corner cases and then successively add more functionality. A first starting point is to turn off the gas jet. It introduces much complexity to the method and has to be considered as the major source of uncertainty. Without it no ablation will take place but the instabilities and the structure formation processes on the surface can be understood. They will also vary with the feeding speed and the laser power. Functional relations between the structure formation and these parameters may be determined. A good starting point in this direction are the works of Golovin et al. (2001). The next step would be to slowly add the gas jet and study its impact. Also thinkable is to add the gas jet to an understood process like laser drilling. This can be regarded as a special case of laser beam melt ablation with feeding speed $v = 0$.

Another possibility is to develop a black box model which predicts the expected

surface shape at the current position from the current value of one or more state variables. Possible approaches are cellular automata and self-organising maps (Wolfram 1983; Kohonen 2001) or next neighbour methods in embedding spaces (Parlitz and Merkwirth 2000). The challenge with this methods is to find the right set of state variables to predict the surface state.

4 Analysis of tidal flat sediments

This chapter deals with the analysis of microscopy images taken from sediment cores out of an island in the North Sea. It is a standard problem in biogeochemistry to find out the history of a sediment sample as it tells a part of the history of its extraction region. We want to describe new methods which allow to gain insight in the spatial distributions of chemical elements within single sediment layers. This information allows conclusions on the sediment formation history.

Marine sediments are complex biogeosystems which are formed by a great variety of processes on many time and spatial scales. Textural and structural characteristics of a sedimentary sequence or even a certain layer document the acting processes of sedimentation (Pettijohn and Potter 1964). The analysis of distributions of grain sizes and pores or ensembles of components and other details of a sediment is a basic instrument in sedimentological studies (Tucker 2001). The analysis of sediment samples gives insight into the formation of the sediments and therefore enables to reconstruct environmental conditions. Recently, it has been shown that biogeochemical processes involved both in the formation and in the alteration of a sediment can be monitored via careful analysis of sedimentary geometries (Visscher et al. 2000; Anguy et al. 2001; Haussels et al. 2001; Morford et al. 2003).

A pending problem is to identify certain processes of sedimentation and diagenesis when analysing different geometries of a sediment and to deliver quantitative information on these geometries. The aim of this study is to provide measures on sedimentary geometries which can be regarded as proxies to physical processes and to biogeochemical processes. In this study we analyse small samples of siliciclastic tidal sediments at a millimetre scale. At this scale microorganisms form microbial mats growing on top of the inorganic matter (clastic minerals). The microbial mats form during periods of low sedimentation rates on the sediment surface. Inorganic matter can be brought in by wind. During certain flood periods the mats are buried by sedimentation. If the deposited layer is too thick, the microorganisms die and the newly created sediment surface is inoculated again. Otherwise, microbes are

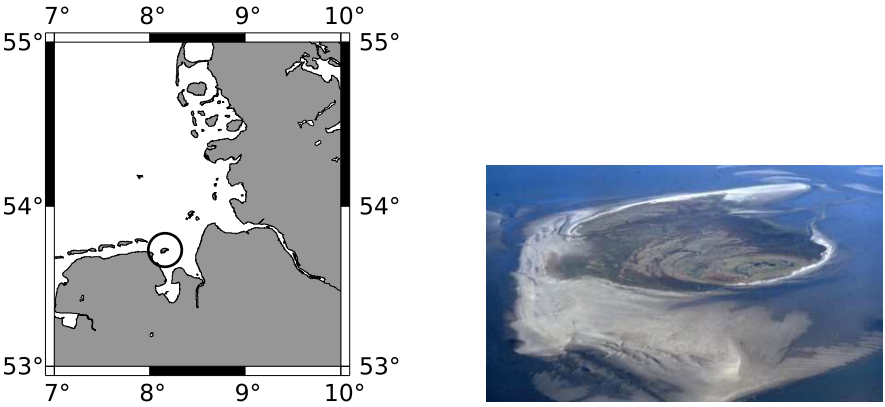

Figure 4.1: Left: Location of Mellum Island in the North Sea. The island is located in the middle of the circle. Right: Bird's eye view of the island.

capable to penetrate the surface layer and to colonise the surface again.

The chemical composition of microbial mat layers differs from other layers which were created by sedimentation processes. We want to exploit this property to distinguish different layers in the sediment by the density and spatial configuration of chemical elements. We use electron microscopy images to perform a quantitative analysis which allows us to derive unique properties for each layer. The chapter is organised as follows: first we will introduce and describe the particular samples we used for our analyses. Then we will proceed with presenting a numerical algorithm which helps finding the boundaries of the sediment layers. The results in that section are published in (Bube et al. 2006a). In the next section the algorithm is applied and the sediment layers are analysed. Firstly we use an entropy measure to characterise the distribution of the elements. Secondly we use symbolic dynamics to calculate characteristic cluster sizes. Those results are mostly taken from (Bube et al. 2006b). At the end we summarise the results and draw our conclusions.

4.1 The data

In our analysis we use sediment samples taken from the supratidal area of Mellum Island in the German Bight. Figure 4.1 shows an image of the island's location.

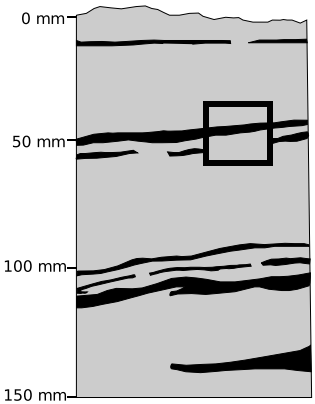

Figure 4.2: Sketch of the sedimentary profile. The upper layers of the supratidal sedimentary column represent a sequence of siliciclastic layers (grey parts) and intercalcated microbial mats (black parts). The rectangle focuses on the section regarded in this study in detail.

Its geographic coordinates are 53° 43′ 16″ N, 8° 8′ 58″ E. The samples were taken from lower supratidal areas and consist of porous siliciclastic sediments with high biological activity. The laminated sediments are nerved with microbial mats (Gerdes et al. 1985; Block et al. 1991). As the sediment was bedded in supratidal area of the island it is mostly excluded from the tidal cycle. It is only flooded during tidal waves. Thus the succession and thickness of the layers are expected to be much more irregular than in samples from the intertidal zone. High biological activity during times of low sedimentation documents itself in biofilms of microbial mats. Our samples originate from the upper section of the sedimentary profile, which consists of fine grained quartz sand with intercalcated microbial mats and biofilms of several millimetres thickness (Gerdes et al. 1985; Block et al. 1991). A sketch of the sediment bedding is given in Fig. 4.2.

Small pieces were sub-sampled and surveyed as thin polished films under a scanning electron microscope equipped with an energy dispersive X-ray analysis device (Block et al. 1991). This device measures the X-ray backscatter of the chemical elements in the probe, which were excited by an electron beam. The chemical elements are distinguished by their characteristic absorption lines. The preparation method of the samples ensures that information of the spatial distribution of the

chemical elements is preserved. This gives us a spatial image of the densities of various chemical elements. The element densities give insight into the composition of the sediment. The succession of various layers indicates different processes that formed it.

Figure 4.3 shows the raw measurement data for one sample. The measurement device measures the different chemical elements simultaneously. We measured three chemical elements: calcium, silicon and aluminium. These elements indicate different processes in the sediment. Silicon and aluminium are mostly remnants of inorganic structures, whereas calcium is an important component of organic matter. In sec. 4.2 we analyse these measurements. In sec. 4.3 a different measurement was necessary in order to understand the working principle of the electron microscope. We tried to measure the same spot on the sediment sample and did a quite good job there. As the measurement process took much longer for each run, we decided to use a smaller image and only measure calcium and silicon as those have the most pronounced structures and represent a process class, respectively.

4.2 Finding the layers

The interpretation of sedimentary formations is based on the careful analysis of textural and structural properties. Recently, much progress has been achieved in identifying units and layers of sedimentary sequences and their internal characteristics as well. This is considerably due to the application of methods based on wavelets (Daubechies 1992; Louis et al. 1998). Wavelets have been used successfully in the analysis of seismic (Gunninga and Glinsky 2006; Capilla 2006) or gravity data (Fedi et al. 2005; Cooper 2006), and in the characterisation of porous media (Sahimi 2000). However, there are not many works which use wavelets as a tool to directly detect sediment layer boundaries. Niebuhr and Prokoph (1997) used wavelets to detect periodicities in sediment successions from one dimensional data. Maroni et al. (2001) used a multiscale approach for the detection of deep-sea subbottom horizons from two dimensional images. This method looks for the maxima lines in smeared acoustic profiler images.

For many questions it is sufficient to get a rough estimation on the sequence of the layers. However, whenever a quantitative analysis is needed, it is indispensable to separate the different layers, to be able to assess statistical measures for the individual layers. This task is simple as long as the layer boundaries are just horizontal straight lines or boundary regions can be dropped. But this is often not

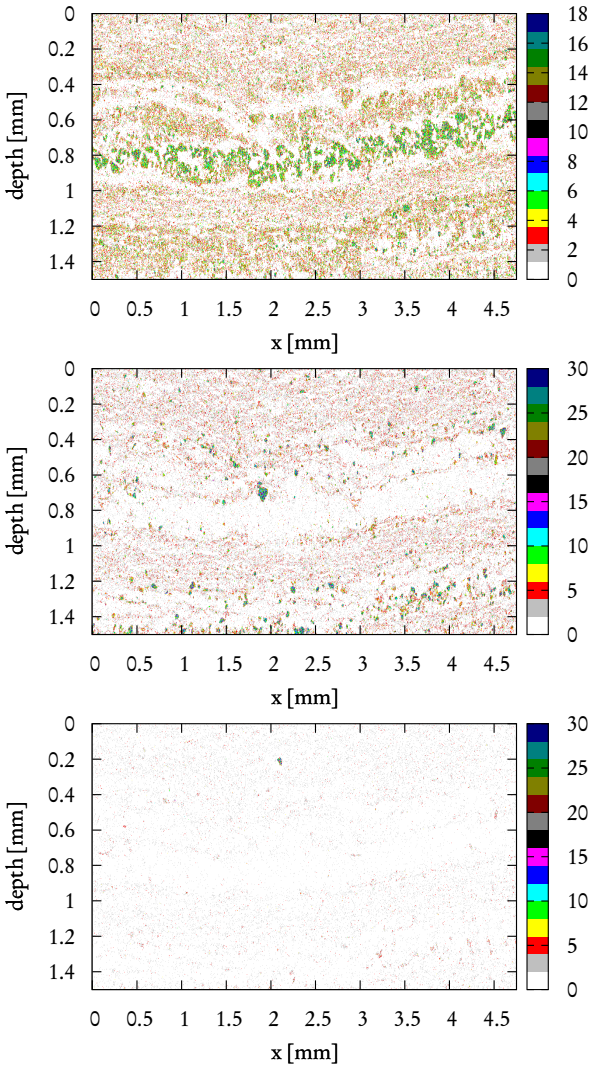

Figure 4.3: Raw electron microscopy measurements. From top to bottom: calcium, silicon and aluminium.

the case, the layers can be rippled or even rather complicated in their geometrical structure. Moreover, the data sets are often small so that every point is needed to improve the statistics. Thus an algorithm is required which is able to detect such boundaries. Conventional methods from image processing libraries mostly fail in such cases, because they do not consider additional information such as the orientation or the curvature of the boundary line. The standard method in this area is the one introduced by Canny (1986) and is now part of most image processing toolboxes. Canny's work uses the derivative of a Gaussian as an optimal filter function which emphasises large gradients. This method works well for detecting any gradients in images, but yields lots of false positives as not every gradient in the image is a layer boundary. One has to make the definition of a layer boundary more strict.

In the following we present a method which helps to detect layer boundaries within two-dimensional data sets obtained from sediment profiles. The data may be high-resolution photographs or two-dimensional maps of certain features, e.g. chemical element densities. A change from one layer to the next one is characterised by a considerable change of the particular feature over a long contiguous range. This change can be identified by a strong gradient of the feature. Our method makes use of the fact that in most applications the layers are to some extent parallel to a baseline. Naturally this is also the baseline of the data set. This is the major difference to conventional edge detection methods (e.g. (Canny 1986)) where no direction information is assumed, but it turned out that this additional information is very helpful in order to avoid lots of false positives. The presented algorithm is based on a two-dimensional multiscale decomposition (Mallat 1989a) of the data. More or less horizontal lines of maximal gradients are searched within the coarse grained data. Afterwards the lines are transferred back to the finer scales. After applying this procedure it is possible to detect the different layers and subsequently to analyse the properties of every single layer.

The basic idea of our method is that we make use of a modified multiscale approach which was originally developed by Maroni et al. in 2001 to automate the search for layer boundaries in our sediment profiles. The algorithm is based on a wavelet decomposition of the underlying image in various scales (Mallat 1989a,b). While in the original work by Maroni et al. the aim was to find longest connected lines of similar height within greyscale images, we are looking for maximal gradients. Furthermore, we use smoothing techniques in order to suppress noise influences and a modified line following algorithm which manifests the assumption that the orientation of the layer boundaries does not deviate too much from the

baseline orientation. This has proven to help avoiding many false positives for our application.

First we present the proposed algorithm in detail by means of an artificially created profile. We evaluate this profile where the layer boundaries are known and compare the expected versus the calculated result. We proceed by applying our method to a core taken from the Pacific deep sea floor, where the layer boundaries are quite smooth and regular. Afterwards we analyse a micro-sequence of a profile taken at Mellum Island in the North Sea. This illustrates the capabilities of the algorithm when applied to sediments with a clustered structure where the boundaries are very irregular.

4.2.1 Theoretical background

The multiscale decomposition method which is the heart of our proposed algorithm allows a signal $f(x,y)$ to be decomposed into two parts: an approximation part $a_s(x,y)$ and a detail part $d_s(x,y)$ at a certain scale s. The detail part contains all information of the signal at s, while the approximation part contains all information of f at smaller scales. The original signal can be retrieved by adding both

$$f(x,y) = a_s(x,y) + d_s(x,y). \tag{4.1}$$

$a_s(x,y)$ can further be decomposed and more and more details can be removed from the signal and a coarse representation of the image is obtained

$$f(x,y) = a_{s-n}(x,y) + d_s(x,y) + \cdots + d_{s-n}(x,y). \tag{4.2}$$

Actually in two dimensions the detail coefficients $d_s(x,y)$ are split into three parts d_s^h, d_s^v and d_s^d which hold the information contained in horizontal, vertical and diagonal direction. However, this is not relevant for our application and we summarise this as the detail part. For our analysis we are only interested in the approximation part.

The decomposition algorithm works the following way: Let $f(x,y) \in \mathbf{L}^2(\mathbb{R}^2)$ be the measured image. $\mathbf{L}^2$ is the vector space of measurable, square-integrable functions. There exists a *scaling function* $\phi(x) \in \mathbf{L}^2(\mathbb{R})$, such that if $\phi_{2^j}(x) = 2^j\phi(2^j x)$ is the dilatation of $\phi(x)$ by 2^j, $j \in \mathbb{Z}$, then $(\sqrt{2^{-j}}\phi_{2^j}(x - 2^{-j}n)\phi_{2^j}(y - 2^{-j}m))_{(n,m)\in\mathbb{Z}^2}$ is an orthonormal basis of the vector space $\mathbf{A}_{2^j}$ of all possible approximations at scale 2^j of the functions in $\mathbf{L}^2$ (Mallat 1989a). We can approximate

the signal $f(x,y)$ with ϕ_{2^j} by calculating the inner products

$$a_{2^j}(n,m) = \langle f(x,y), \phi_{2^j}(x-2^{-j}n)\phi_{2^j}(y-2^{-j}m)\rangle_{(n,m)\in\mathbb{Z}^2} \tag{4.3}$$

$$= \iint_{-\infty}^{+\infty} f(x,y)\phi_{2^j}(x-2^{-j}n)\phi_{2^j}(y-2^{-j}m)\,dx\,dy\,. \tag{4.4}$$

A similar theorem exists for the detail part at scale 2^j. It can be shown that for every scaling function $\phi(x)$ there exists a corresponding orthogonal wavelet $\psi(x)\in\mathbf{L}^2(\mathbb{R})$, where $(\sqrt{2^{-j}}\psi_{2^j}(x-2^{-j}n))_{n\in\mathbb{Z}}$ forms an orthogonal basis in the space of signal details.

Let $\mathbf{A}_{2^j}$ be the vector space of signal approximations at scale 2^j, then

$$\mathbf{A}_{2^{j+n}} \subset \ldots \subset \mathbf{A}_{2^{j+1}} \subset \mathbf{A}_{2^j}\,. \tag{4.5}$$

This means that the image may be decomposed into coarser and coarser parts as the finer scales are successively removed. This is the property we want to exploit for our purposes. For our analysis we use the well known Haar wavelet

$$\psi(t) = \begin{cases} 1 & 0 \le t < \frac{1}{2} \\ -1 & \frac{1}{2} \le t < 1 \\ 0 & \text{otherwise}, \end{cases} \tag{4.6}$$

whose corresponding scaling function is

$$\phi(t) = \begin{cases} 1 & 0 \le t \le 1 \\ 0 & \text{otherwise} \end{cases} \tag{4.7}$$

(Louis et al. 1998). This wavelet is also known as the Daubechies D2 wavelet as it is a special case of the Daubechies wavelet family and is orthogonal to polynomials up to second order (Daubechies 1992). Wavelets with higher vanishing moments may also be used for our method and may yield better results in some applications. However, this was not the case with our data sets, so we decided to keep the simplest wavelet possible.

4.2.2 The algorithm

The main idea of the algorithm is to look first at a coarse grained instance of the original image, search for some desired property and then propagate it back again

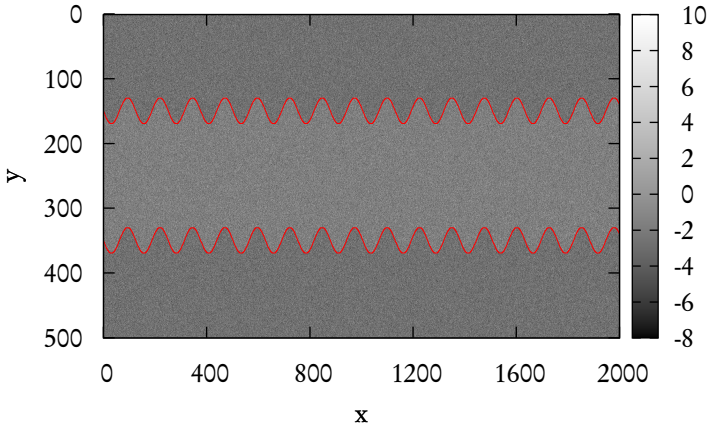

Figure 4.4: Artificial example layers. The boundaries are sines. In the two outer layers to each pixel the value 0 is assigned as the characteristic feature, while in the middle layer this value is elevated by 1. Afterwards Gaussian random numbers with a variance of 2 and zero mean are added to the image. The red lines mark the theoretical, undisturbed boundaries.

to the finer scales. The property we are interested in are distinguished gradients more or less parallel to the image baseline. In order to demonstrate the algorithm, we produce an artificial sediment profile. We generate an empty image filled with zeros, add two sinusoidal layer boundaries and fill the space in between them with ones. Afterwards we add random Gaussian noise with a variance of 2 to the whole image. Thus, the characteristic feature of the layers are their mean values. The result is shown in Fig. 4.4.

Finding the line seeds

1. As can be seen in Fig. 4.4, the raw image is very irregular. Although it is possible to distinguish brighter and darker layers by eye, it is very difficult for a computer to distinguish different regions. This is a common problem also with sediment data. Fortunately, the disturbances only play a role at small scales, so we use the multiscale decomposition to remove them.

   We start the algorithm by decomposing the measured image $f(x,y)$ accord-

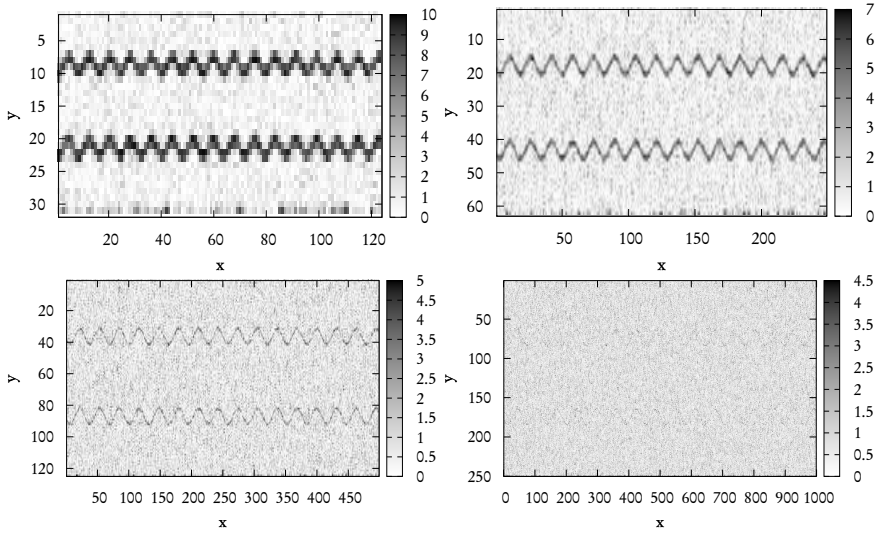

Figure 4.5: Absolute value of the gradient in the y-direction of the decomposed images. From upper left to lower right decomposition levels 4 to 1 are shown. The size of the moving average window is 2 in x- and 1 in y-direction.

ing to the Mallat algorithm described in section 4.2.1. According to Eq. (4.4) this gives us a series of images $a_{2^d}(x,y), d = 0 \ldots l$, where l is the maximum decomposition level ($d = 0$ is the original image). l has to be chosen by the user. Usually the finiteness of the data sets tight limits on what is a useful coarse graining.

2. We define a layer boundary as a more or less horizontal curve where the gradients in vertical y-direction are maximal. Therefore, we do not look at the decomposed image $a_{2^l}(x,y)$ itself, but at the image of absolute values of gradients in y-direction

$$\Delta a_{2^l}(x,y) = |a_{2^l}(x,y) - a_{2^l}(x,y+1)|. \tag{4.8}$$

In Fig. 4.5 this is shown for our artificial example. It can be seen that the width and height of the image is divided by 2 for every coarse graining step.

3. Often the approximation image is still quite irregular. Thus in the next step the decomposed gradient image at level l may be smoothed by a moving average filter

$$\Delta h(x,y) = \frac{1}{MN} \sum_{j=y}^{M+y-1} \sum_{i=x}^{N+x-1} \Delta a_{2^l}(i,j), \tag{4.9}$$

where N and M are the sizes of the moving average window. These parameters have to be chosen by the user. The results have to be harmonised with the expected results by adjusting N and M. With our used data sets this was possible within a few iterations. Unsuitable values often result in sudden high jumps in the layer boundaries. The right configuration yields quite smooth boundaries with only a few jumps.

4. Our aim is to find the k strongest gradient lines which are more or less parallel to the x-axis of the image and which are as long as possible. This number of lines k we search for has to be chosen in advance. As the lines do not have to be exactly parallel to the x-axis, we calculate the deviation of each column at position x from the parallel as the cross correlation to the first column

$$\xi(\tau(x)) = \sum_{y} \Delta h(1,y) \Delta h(x, y+\tau). \tag{4.10}$$

To get the main layer boundaries we take the average over all gradients shifted by $\tau(x)$ where ξ is maximal

$$\Delta \tilde{h}(y) = \frac{1}{N} \sum_{x}^{N} \Delta h(x, y+\tau(x)). \tag{4.11}$$

Let the k highest maxima in $\Delta \tilde{h}(y)$ be at y_i, with $i = 1 \ldots k$. Then our layer boundaries in the coarsest image are at $(x, y_i + \tau(x))$. To demonstrate this procedure a cross section along the y-axis is shown in Fig. 4.6. The shifted profiles and the resulting mean value are displayed.

Propagating the seed lines to the finer images

The propagation to the finer scales is quite straightforward. In the previous subsection we calculated the initial lines to be at $(x, y_i + \tau(x))$ at resolution level l.

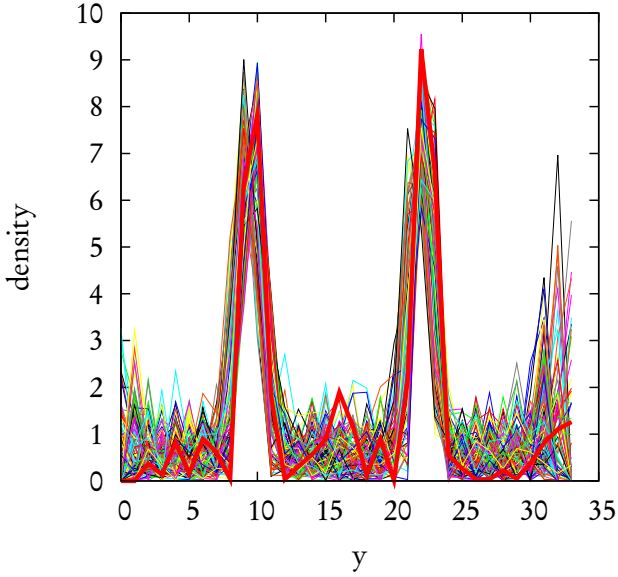

Figure 4.6: Cross sections along the y-axis of Δh. The lines are shifted by the lag τ which yields the maximal correlation coefficient ϕ between the first and the concerned line. The thick red line is the mean of all lines.

In level $l-1$ the width and height of the image doubles for the Haar wavelet and the lines from the coarser level get smeared from (x,y) to $(2x,2y)$. The upscaling happens now as follows.

1. We calculate the gradients in y-direction (see Eq. (4.8)) of $a_{2^{l-n}}(x,y)$, where $n=1\ldots l$.

2. Then the result is smoothed with the moving average procedure according to Eq. (4.9).

3. Let $(x,y_i+\tau(x))$ with $i=1\ldots k$ be the layer boundaries at resolution $l-n+1$. As mentioned above the upscaled boundary at $l-n$ gets smeared around $(2x,2(y_i+\tau(x)))$. Therefore we look for the maxima in a band at $(2x,2(y_i+\tau(x))+\epsilon)$ and $(2x+1,2(y_i+\tau(x))+\epsilon)$ with $\epsilon=-1,0,1$. Looking

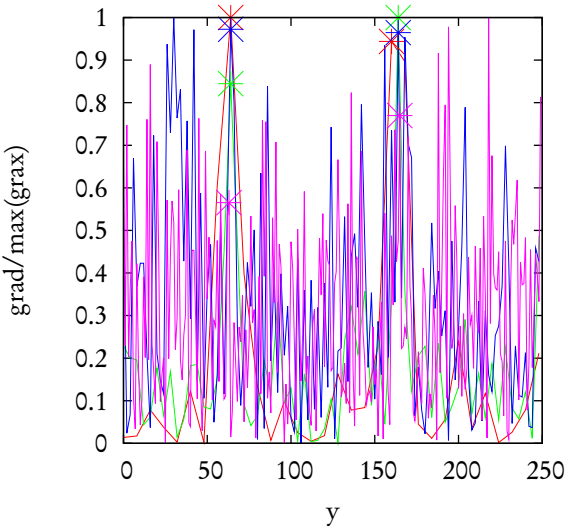

Figure 4.7: Maximum gradients of a column within various coarseness levels. The blue line denotes column 30 of the gradient image at level 4, the red line is column 60 at level 3 and the green line column 120 at level 2. The crosses mark the two tracked maxima. The position of the points on the abscissa is multiplied with 2^j, where j is the scale. This way points from different scales neighbour each other. The curves are normalised so that the maximum is 1, in order to make them comparable.

at $2x + 1$ is necessary as the size of the upscaled image is doubled. These are the positions of the boundaries at resolution $l - n$.

4. The procedure has to be repeated until resolution level 0 is reached. Figure 4.7 shows the tracking of two maxima throughout the upscaling process.

The layers reconstructed by the detection algorithm are displayed in Fig. 4.8. It can be seen that despite the bad signal to noise ratio of the example, found boundaries follow very good the theoretical layer boundary. As shown in Fig. 4.5 the multiscale decomposition successfully removes the noise which mainly acts on the small scales, but the large structures, which are the ones we are interested in

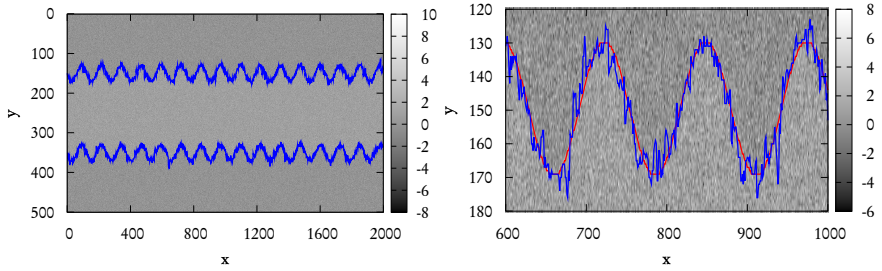

Figure 4.8: Left: The blue lines are the layer boundaries reconstructed by the algorithm from the noisy artificial sediments. Right: a magnification of the upper boundary. The red line indicates the theoretical boundary and the blue line the one the algorithm calculated.

remain. When going up to the finer scales the fluctuations within the image have also an impact on the boundary which becomes visible in the magnification.

4.2.3 Borehole data

As an application for the algorithm introduced in the previous section, we analyse samples from deep-sea borehole cores. The data are taken from the Integrated Ocean Drilling Program (IODP) expedition 301[1]. This expedition gathered core samples from the eastern flank of the Juan de Fuca Ridge west of North America (Expedition 301 Scientists 2005). The section analysed by us is from core 15H, section 3.

We convert the high-resolution colour JPEG image from the database to a greyscale image. The resulting image matrix has 14700×433 points. Systematic trends are removed by subtracting the mean from each column.

The image is decomposed down to the fourth level and smoothed with a moving average window of size 20×3. This size turned out to yield the smoothest lines and eliminates high jumps which occur at smaller window sizes. We search for 35 boundaries. The resulting boundaries found by the algorithm are shown in Fig. 4.9. By comparing the algorithmic result on the right with the lines drawn by the ship board party on the left it can be seen that they match very well. Nearly every boundary found by visual inspection is also automatically detected by the

[1] `http://iodp.tamu.edu/scienceops/expeditions/exp301.html`

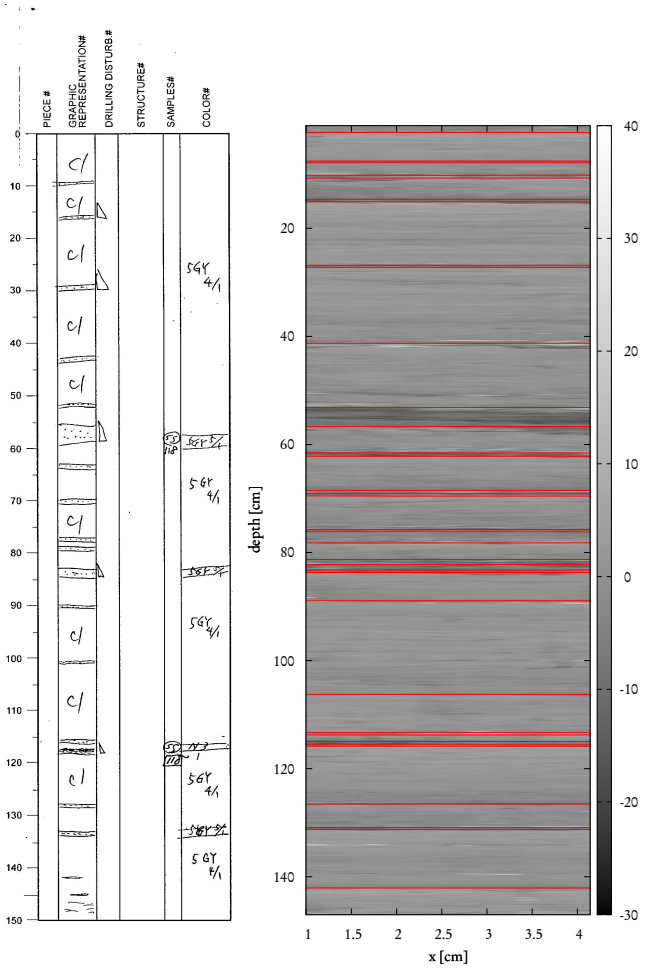

Figure 4.9: Left: the visual core description from the expedition log. (Picture courtesy of IODP.) Right: The layer boundary lines found by the algorithm. A moving average smoothing of 20 in x-direction and 3 in y-direction was used. The number of lines is 35.

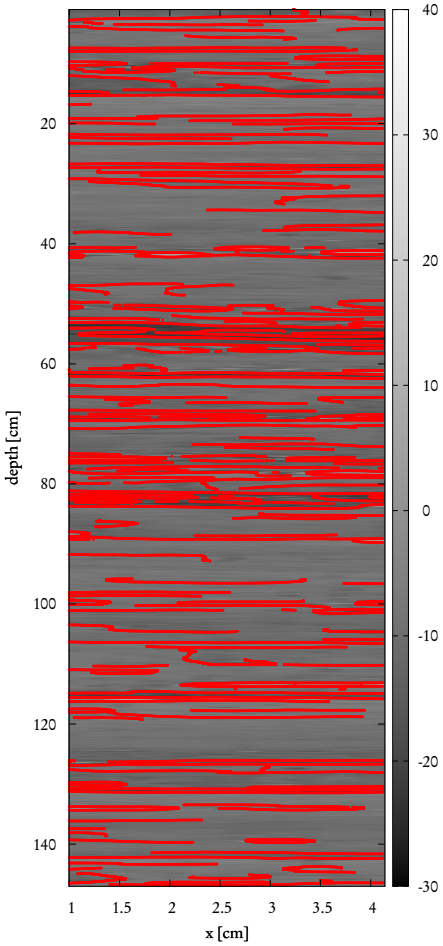

Figure 4.10: Layer boundaries found by the Canny edge detection algorithm. The standard deviation for the Gaussian filter was set to 50.

algorithm. Even the finer structures are well resolved. In between 0 and 10 cm of depth two false positives are found, which are likely due to artifacts in the image or from the cutting of the core. The boundary at 100 cm is not found, probably as it is too badly resolved on the photograph.

The result of the proposed algorithm looks even better if it is compared with the result of the Canny edge detector displayed in Fig. 4.10. The standard detector is clearly unsuitable for the application as it finds much too many boundaries. As it makes no assumption on the orientation of the layers, it detects every contour within the image. This is what the algorithm was designed for, but this is clearly undesirable in this particular application. Also adjusting the standard deviation of the Gaussian filter does not improve the result significantly.

4.2.4 Experimental data from tidal sediments

Now we want to test the algorithm on the tidal flat sediment samples. They exhibit a more irregular structure compared to the borehole sample. The layer boundaries are curved and often broken so that the algorithm has to connect the gaps. Out of the three measured chemical elements calcium shows the most distinguished layer structure. We set the number of boundaries to be found to 6 and got the lines displayed in Fig. 4.11, upper panel. The boundaries found in the image match very well to what one would expect from visual inspection.

The result for the Canny edge detector is shown in Fig. 4.11, lower panel. For this data set the method performs much better than for the borehole dataset, but again the result of the multiscale algorithm is better. The boundary of the calcium rich zone is detected quite well, but the boundary line is broken at many places. The boundaries of the other zones are indicated but even more discontinuous.

It is now possible to compare the properties of the calcium layers to the layers of the other elements. Therefore, we transfer the boundaries obtained from the analysis of calcium to the measurements of the other elements. This is shown in Fig. 4.12. For calcium we can see that the fourth layer (counted from top to bottom) consists of large clusters of calcium. For silicon and aluminium this is a depletion zone. In the sixth layer accumulations of silicon and aluminium can be found. In general one can see that the lines clearly divide regions of different characteristics in terms of element densities.

Table 4.1 lists the mean measured densities $\langle\rho\rangle$ and the standard deviation σ for the found layers. It can be seen that the standard deviations are quite high compared to the mean densities for all layers. This is because of small clusters of

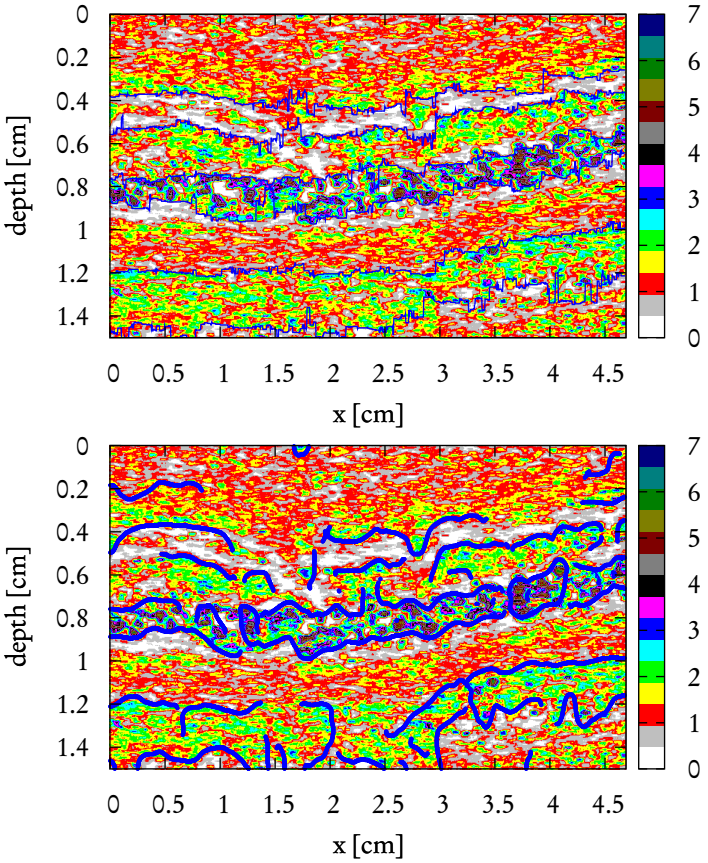

Figure 4.11: Upper panel: Densities for calcium smoothed by a moving average window of size 20 in x-direction and 3 in y-direction. In blue are the calculated layer boundaries. Lower panel: The same but the layers are searched by the Canny edge detector. The standard deviation of the filter function was set to 15.

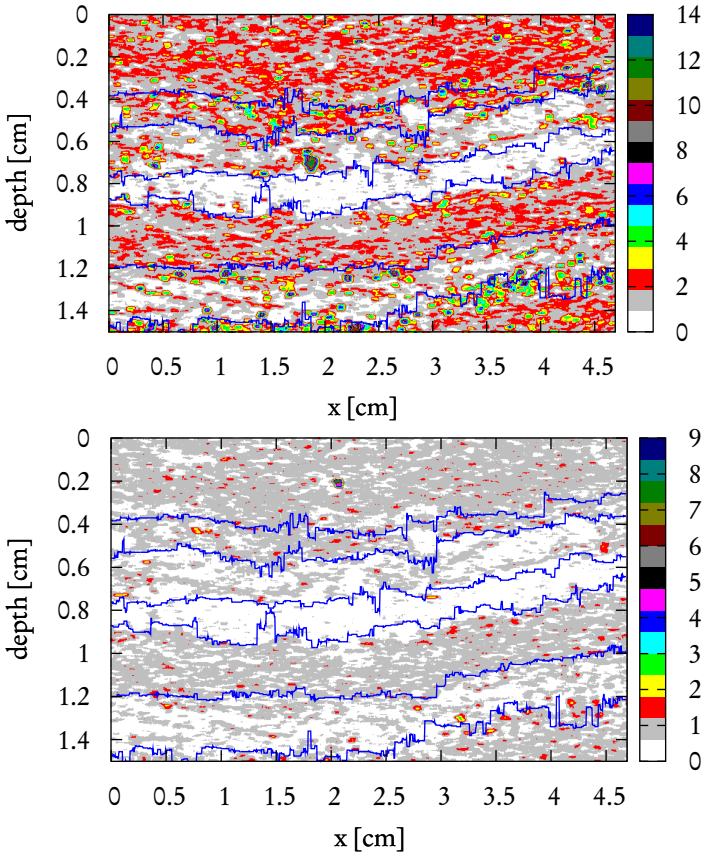

Figure 4.12: Upper panel: image of silicon densities. Lower panel: image of aluminium densities. The size of the moving average window was the same as for calcium (see Fig. 4.11).

Table 4.1: Mean densities $\langle\rho\rangle$ and standard deviation σ within the different layers.

Layer	Si		Ca		Al	
	$\langle\rho\rangle$	σ	$\langle\rho\rangle$	σ	$\langle\rho\rangle$	σ
1	1.902	0.644	1.245	0.417	0.815	0.272
2	2.057	1.119	0.880	0.497	0.773	0.237
3	1.536	1.102	1.420	0.679	0.616	0.216
4	0.893	0.389	2.462	1.228	0.457	0.144
5	1.707	0.634	1.180	0.526	0.759	0.225
6	1.688	1.130	1.636	0.603	0.648	0.232
7	2.444	1.437	1.191	0.578	0.760	0.253

very high densities which are existent in all layers. Here a cluster size analysis and the comparison of density distributions are more suitable to get more pronounced differences between the layers. In Fig. 4.13 the density distributions for the different layers are shown. The obtained distributions make it possible to develop and fit theoretical process models. It can be seen that layer 4 clearly exhibits different characteristics as the other layers. As we will show in the next section, this layer contains the microbial mat.

4.3 Pattern analysis of silicon and calcium layers

In this section we introduce statistical measures to characterise the distribution of silicon and calcium in different layers of the sediments. We also use cluster analysis and symbolic dynamics to filter measurement noise and to classify different density regions. This allows to calculate characteristic patch sizes which reflect the sizes of individual clastic grains and the corresponding pore sizes. Silicon indicates the independent processes in the sedimentation history of certain grains. Calcium is capable to monitor intrinsic early diagenetic processes of biogeochemical calcium mineralisation of primary organic matter as documented in more organised distributions with higher clustering.

Figure 4.14 illustrates the scanning of the electron beam of the microscope. Every point of the measurement grid is processed several times. On every i-th step

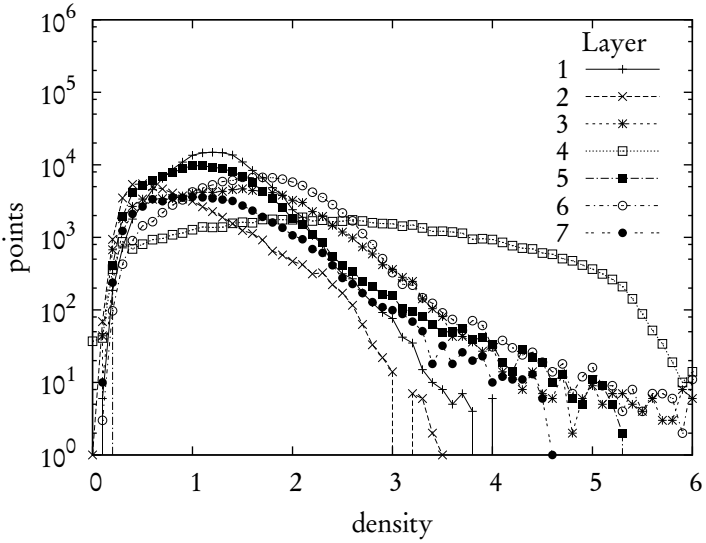

Figure 4.13: Distribution of calcium densities within the calculated layers.

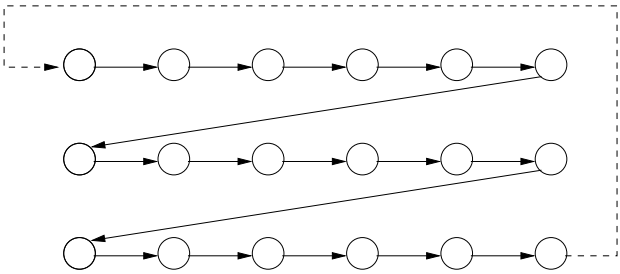

Figure 4.14: Working principle of the scanning electron microscope. The X-ray backscattering is measured on a grid.

a number $r_i \in \mathbb{N}_0$ is returned at point (x, y) with a probability $p_{(x,y)}(r_i)$ which is proportional to the concentration of the chemical element under consideration. The r_i are cumulated so that the measurement matrix the device returns is the summation of various sampling steps. In that way, the more often the sample is scanned, the more accurately is the resulting image reflecting the underlying concentration of the chemical element. This is a consequence of the central limit theorem (Papoulis 1984). However, the number of repetitions is limited by the time the measurement takes (about 2 minutes for each scan over the whole surface) and the fact that the method is not completely non-destructive. The electron beam charges the material and destroys a non-negligible amount of the sample after some measurements.

We measured densities of silicon and calcium for this test series. Those two elements were chosen since silicon is mostly a component of inorganic matter whereas calcium is an important representative of organic compounds. Each measurement yields a 512×512 matrix. The surface is scanned 50 times, so that finally the measurement matrix contains the cumulated entries on the grid. We tried to meet the same region on our sediment sample for this measurement as in sec. 4.2. This worked quite well, but slight differences can be seen when comparing Figs. 4.3 and 4.15. Those concern mostly the rotation of the cutout and do not influence the further results.

Figure 4.15 shows the measurement data from the microscope. It can be seen that the sediments consist of various layers with different characteristics. Every layer has a different abundance of chemical elements and different characteristic sizes of its element clusters. We calculated the layer boundaries with the help of a multiscale algorithm which searches for strong, horizontally connected, vertical gradient changes (Bube et al. 2006c). In Fig. 4.15 the found boundaries are marked with red lines. The layers were calculated for calcium because of its most pronounced layer structure. These layer boundaries were also taken for silicon assuming that the same layers should also be present for all elements. A cross check did not yield large deviations from this assumption.

4.3.1 Understanding the measurement process

In the previous section we noticed that the measurement process is stochastic by nature. Therefore, we can only make statistical statements. Before we go into the surface analysis, we want to describe the measurement process in more detail.

Each measurement site (x, y) scatters back a certain intensity of X-rays. The

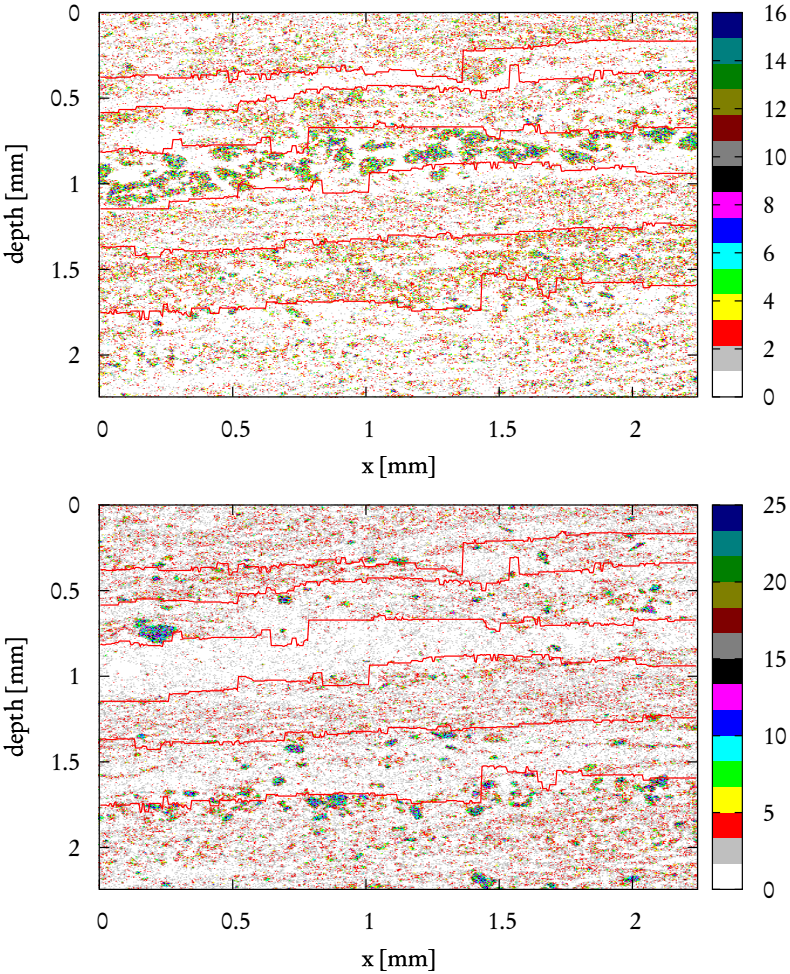

Figure 4.15: Measurements from a sediment sample. The image is the sum of 50 single measurements. The red lines are the layer boundaries found by a layer searching algorithm. Upper panel: calcium, the numbers within the sediment plot mark the layer numbering; lower panel: silicon.

precise number of backscattering events and the energy of the rays is stochastic as a number of effects cause the emission of X-rays, namely the Compton effect, Auger effect and the normal relaxation of the electrons in the atomic hull. If a certain threshold is reached, the detector emits a signal and the count at that point is incremented by one. This may be repeated several times. The probability for a response r at point (x,y) is $p_{(x,y)}(r)$. We repeat the experiment N times and add the number of responses $r_i(x,y), i = \{1 \dots N\}$, the probability of the result $R(x,y) = \sum_i r_i(x,y)$ is

$$p_{(x,y)}(R) = p_{(x,y)}(r_1) \circ \cdots \circ p_{(x,y)}(r_N), \tag{4.12}$$

where $\circ$ denotes a convolution. In order to get a good estimation for $p_{(x,y)}(R)$ N has to be very large. This is experimentally infeasible. If the surface is homogeneous, the element concentrations are constant and the fluctuations are mainly due to the atomic emission mechanisms and have the same statistics for every point. This means that the probability is spatially independent, i.e. $p_{(x,y)}(R) = p(R)$. Therefore, it can be estimated from all measurement points on the surface which drastically increases the reliability. We verify this assumption by analysing glass as an amorphous material and measure the contents of silicon and calcium. The result is shown in the upper panel of Fig. 4.16. In order to model the probability density functions in terms of Eq. (4.12) we assume that the probability for a response is equal for each point, thus $p_{(x,y)}(r) = p(r)$. This is reasonable, as the sample is homogeneous in a good approximation. Furthermore, we assume that the results r_i are uncorrelated due to the intrinsic measurement noise. This leads us to a Poisson distribution

$$p(r) = \frac{\lambda^r}{r!} e^{-\lambda}, \tag{4.13}$$

where λ is the average value of the data.

The parameter λ can obviously be easily calculated from the data. Therefore, we are now able to generate artificial surfaces with the same properties as the homogeneous samples. We generate a 512×512 (the same size as the original measurement) matrix with natural numbers distributed according to Eq. 4.13. The distribution parameter λ is calculated as the mean of the 50 single measurements from the glass sample. The result is shown in Fig. 4.17. It matches very well the experimental result.

To mimic the real measurement process we generate 50 such 512×512 measurement matrices possessing the same distribution and add their entries as the

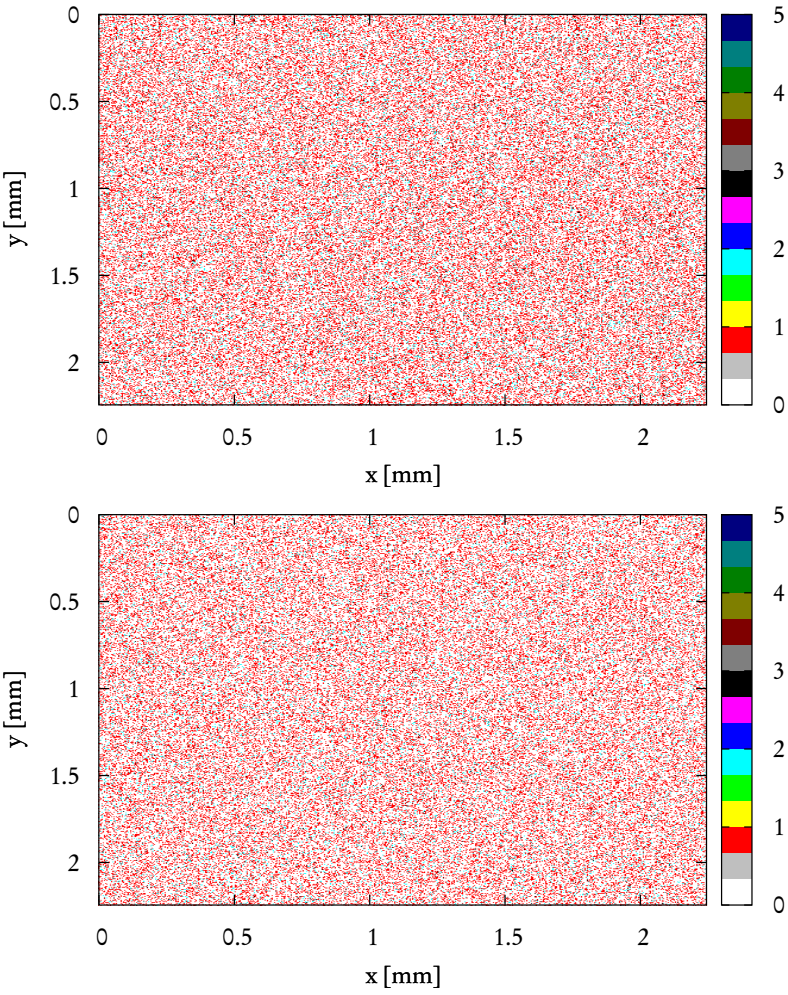

Figure 4.16: Upper panel: calcium measurement data of the analysis of glass. Lower panel: an artificial surface generated by adding exponentially distributed random numbers.

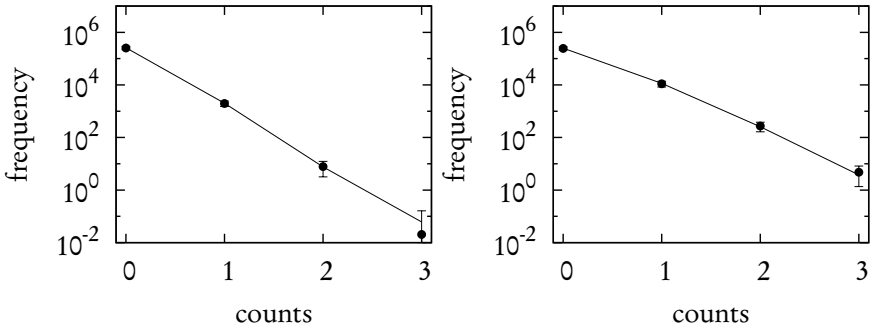

Figure 4.17: The dots mark the mean frequency of responses for a single scan over the glass sample. We averaged over 50 iterations. The error bars denote the standard deviation. The solid line indicates the frequency calculated from a Poisson distribution with λ estimated as the mean of the measured glass data. The left panel displays the results for calcium, the right one for silicon.

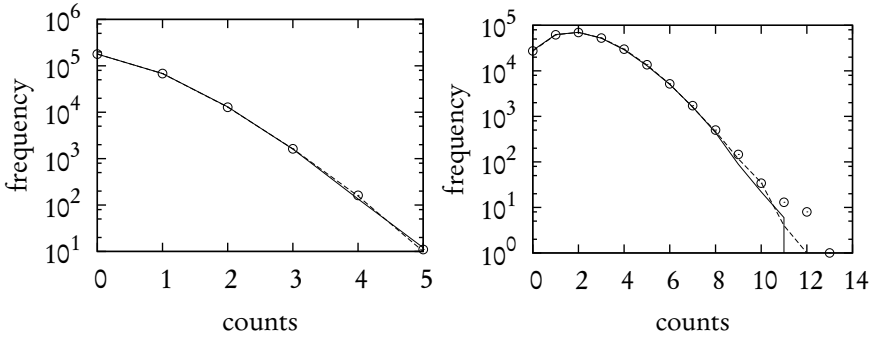

Figure 4.18: Frequency of the measurement responses integrated over 50 scans. The circles mark the integrated responses measured on a glass sample, the solid line indicates the result simulated by integrating over 50 Poisson distributed random surfaces, the dashed line marks the result from a single random surface with λ estimated from the integrated glass data. Left panel: calcium, right panel: silicon.

cumulated values. An example is shown in the lower panel of Fig. 4.16. The density distribution of the resulting artificial measurement matrix is plotted in comparison to the measured glass sample in Fig. 4.18. The result from a set of Poisson distributed random numbers with λ calculated directly from the measured data is also shown in that figure. Both results match equally well.

4.3.2 Probability analysis

In many applications one is interested in quantifying how clustered an entity which was measured on a two-dimensional grid is. A possibility for such a quantification is to assume a homogeneous distribution and calculate the deviation from this assumption. In our particular case a homogeneous distribution of chemical elements on the surface plane is characterised by a Poissonian distribution of the detector responses as we have shown in the previous section. A structured surface violates the assumption that the average measurement is equal for every pixel and thus will yield a distribution different from a Poissonian.

When measuring data from sediments the probability for a response is not homogeneous over the sample, but spatially variant depending on the distribution of chemical elements in the sample (see Figure 4.15). The probability to measure a response, e.g. for silicon, is much higher at locations with quartz grains than at locations with clay. The difference in terms of information between the homogeneous case and the structured case can be measured by the Kullback-Leibler (KL) distance (Kullback and Leibler 1951), which is given by

$$k(p,q) = \sum_x p(x) \log_2 \frac{p(x)}{q(x)}. \tag{4.14}$$

$q(x)$ is the *a priori* probability and $p(x)$ the *a posteriori* probability. In our case the *a priori* probability is given by the assumption that every element is distributed homogeneously. Thus $q(x)$ can be estimated by a Poisson distribution with the same average as the sediment measurement. $p(x)$ is the probability which is estimated from the sediment sample.

As some *a priori* events are very rare and do not occur in numerical experiments we use a modified probability estimator

$$p(x) = \frac{n_x + 1}{N + M}, \tag{4.15}$$

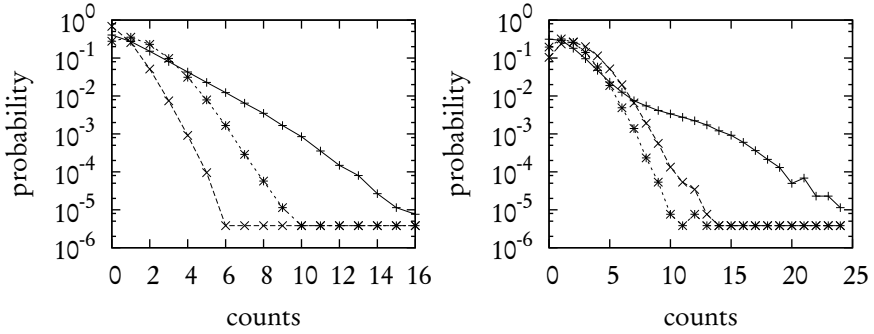

Figure 4.19: Comparison between the sediment (solid) and the glass (long dashes) measurements. The short dashes denote a Poissonian surface with the same average as the sediment sample. Left panel: calcium, the KL-distance from the glass sample is 0.97 and from the Poissonian sample 0.17. Right panel: silicon, the KL-distances are 0.40 and 0.23, respectively.

where n_x is the number of measurements with the result x, N is the total number of measurements and M is the number of bins in which we sort the measurements, i.e. $x \in \{1, 2, \ldots, M\}$.

Figure 4.19 shows the distributions of the detector responses for the sediment profiles in comparison to the glass sample and Poisson distributed random numbers using the mean of the measured sediment data for the parameter λ. These distributions were calculated over the whole surface. We now use the Kullback-Leibler distance to quantify the difference between the distributions in terms of information. As we have shown above, the Poisson distributed random matrices yield a rather good approximation of the homogeneously distributed elements in the glass sample (cf. Fig. 4.18). Their KL distance is less than $2 \cdot 10^{-4}$ for both elements. The standard deviation of the KL distance for 100 different realisations of the Poissonian surfaces is about 1%. The KL distances for the distribution shown in Fig. 4.19 are 0.97 for the distances between the sediment calcium data and the glass sample calcium data, whereas the distance between sediment and Poisson distributed data for calcium is only 0.17. For the silicon data we find 0.4 (sediment – glass) and 0.23 (sediment – Poisson), respectively. It is important to note that the sediment data and the Poisson distributed random matrices possess the same mean value. Thus their comparison yields more insight than the comparison with the

glass sample. That the KL distance between sediment and glass is usually bigger than between sediment and Poisson distributed data is to a large extent due to the different mean values. Furthermore, the distribution of a homogeneous real sample depends on the material characteristics of the material chosen. If another material than glass is taken, another average value of responses and thus another distribution shape has to be expected. Therefore the comparison to a randomly generated surface with the same mean value yields much more reliable results than the comparison with a homogeneous sample of another material.

We also calculated the KL distance for every sediment layer separately and compared it to the corresponding "layer" in the glass sample and the random matrices. The result is shown in Tab. 4.2. If compared with Fig. 4.15, it can be seen that the layers with large clusters have a large KL distance to the Poisson surfaces. These are layer 3, 6 and 7 for silicon and layer 4 for calcium. The other layers are structured but do not include larger clusters which is reflected in a lower KL distance. The layers with the lowest element densities also have a low KL distance. For silicon this is especially layer 4 and for calcium layer 2. A few higher density regions prevent the calcium layer from being as low as the silicon layer. The KL distances of the sediment distribution to the glass sample are generally higher than to the Poisson distributed random matrices. However, these distances are a bad measure to characterise the layers as sometimes clustered layers have a lower KL distance than unclustered ones. The distances of silicon layer 3 and 4 are an example for such a case.

4.3.3 Cluster analysis

From Fig. 4.15 it can be seen that the measurements are disturbed with noise. This is intrinsic to the X-ray backscattering method as there is an amount of uncertainty involved in the backscattering of the X-rays. Therefore, it is necessary to reduce the extent of fluctuations by spatial averaging to improve the reliability of the measurements. This is justified by the fact that the grain size is typically larger than the area covered by a single measurement pixel. As one is mainly interested in the areas with large abundance of certain chemical elements relative to the other areas we use an approach known as coarse graining from symbolic dynamics (Hao 1991; Ott 1993). Each measurement point is assigned a symbol out of a small alphabet which is associated with some distinct property of the system.

In our application it seems natural to choose some binning and to sort the points into these bins. The questions that remain open are how to include the

Layer	Poisson		Glass	
	Ca	Si	Ca	Si
1	0.06	0.08	0.92	0.22
2	0.08	0.14	0.32	0.28
3	0.13	0.31	0.84	0.49
4	0.47	0.05	1.87	0.87
5	0.07	0.07	0.71	0.26
6	0.11	0.24	1.41	0.53
7	0.13	0.33	0.62	0.36

Table 4.2: Kullback-Leibler distances within the single layers. The second and third column lists the distance between the measured and an estimated Poissonian surface, the fourth and fifth the distance between the measured glass sample distribution for calcium and silicon, respectively.

information from the neighbouring points and how to choose the bin thresholds. These problems can be solved by using cluster analysis. We embed the points from the measurement grid in a vector (see Fig. 4.20). For each point $R_{x,y}$ in the grid a corresponding vector

$$\begin{aligned}\xi(x,y) \quad &= (R_{x-1,y-1}, R_{x-1,y}, R_{x-1,y+1}, R_{x,y-1}, R_{x,y}, \\ &\quad R_{x,y+1}, R_{x+1,y-1}, R_{x+1,y}, R_{x+1,y+1})\end{aligned}$$

with the point itself and its next neighbours is created, yielding a 9 dimensional vector. Repeating this for every measurement point we end up with a set of points in a 9 dimensional vector space. As the ordering of points conveys misleading information, we rank order them. Within this 9 dimensional space it is now possible to search for clusters of points using a cluster algorithm. All members of a cluster share the property that the measurement points from which its vectors are composed have similar values. This method has the advantage over moving average or other coarse graining techniques that the binning into clusters is chosen automatically in such a way that the clusters are optimally discriminated. Furthermore all information except the spatial configuration within the grid, which is destroyed by the sorting of the points within the vectors, is preserved for the cluster searching.

For cluster searching we use the well known k-means algorithm (Hartigan 1975;

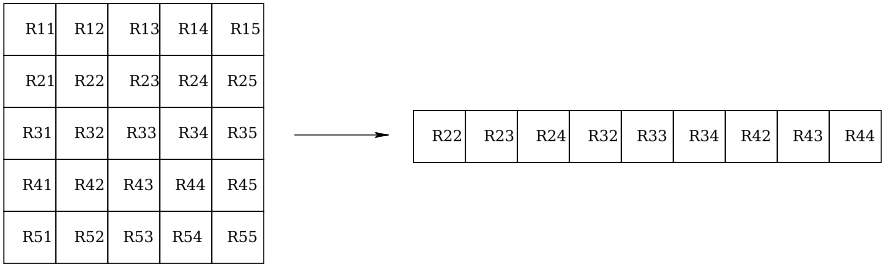

Figure 4.20: Creation of an embedding vector. The neighbouring points around the centre $R33$ are embedded. The points in the embedding vector are rank ordered afterwards.

Hartigan and Wong 1979). With this algorithm the number of clusters has to be preset. After some trials we decided to use three clusters. Choosing more clusters does not make sense with our data sets as the found clusters are too close to each other and the information gain is not large enough to justify it. We denote the clusters with the capital letters A, B and C. A stands for the cluster with the lowest detector responses, B for intermediate values and C for the highest values. A way to measure the discriminability of the clustering is the value

$$d' = \frac{|\mu_1 - \mu_2|}{|\sigma_1 + \sigma_2|/2}, \tag{4.16}$$

where μ_i is the centroid of cluster i and σ_i the standard deviation of the cluster member's distance to it (Green and Swets 1966). Table 4.3 lists the values for d' calculated for our application. For comparison: if the points were Gaussian-distributed around the centroid and we put a threshold in the middle of the centroids, a short tail of both distributions lies on the opposite side of the threshold as its centroid. The d' value would have to be 3.31 so that 95% of the distribution is on the right side of the threshold. Thus we have a satisfactory discriminability of the clusters. In Fig. 4.21 an image of the clusters found from the sediment measurement is shown. This is a noise filtered image of Fig. 4.15. In the fourth layer large grains of calcium can be seen, whereas in the second layer it is lacking almost completely. The others are a mixture, they differ in the structure of the alternation of the different clusters. In general the structures are much clearer than in the raw measurement images. Comparing the silicon and calcium image,

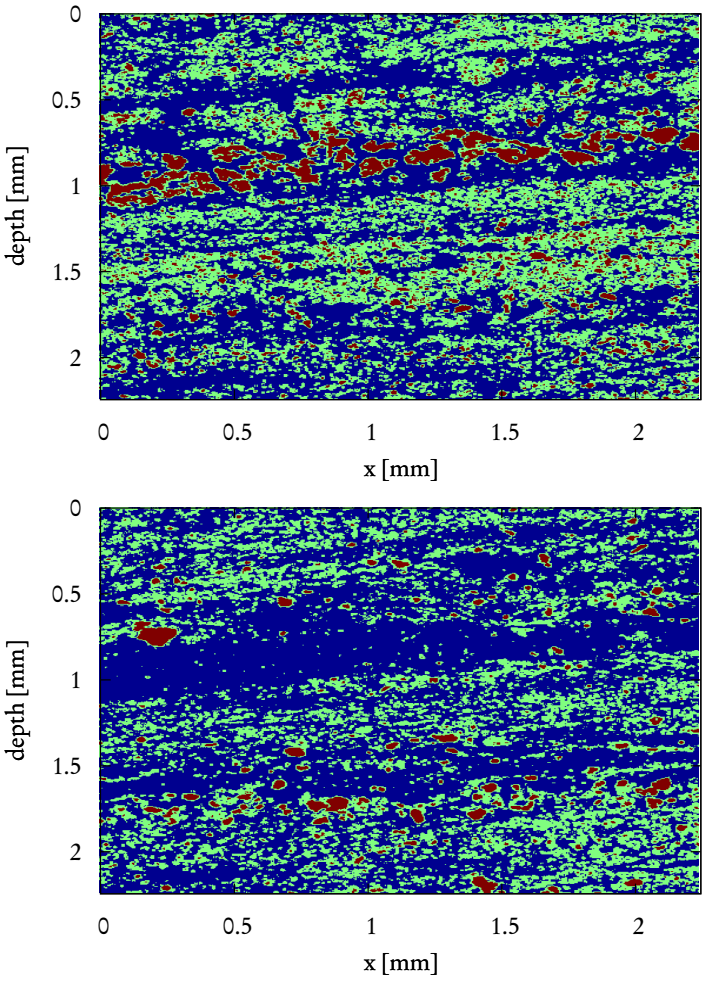

Figure 4.21: Clusters calculated from the element density measurements. The three colours distinguish three clusters, blue is category A, green is B and red is C. The red lines mark the layer boundaries. Upper panel: calcium; lower panel: silicon.

Clusters	Ca	Si
A-B	6.43	4.58
B-C	5.80	7.90
A-C	10.37	12.93

Table 4.3: Cluster distance measure d' for various cluster combinations.

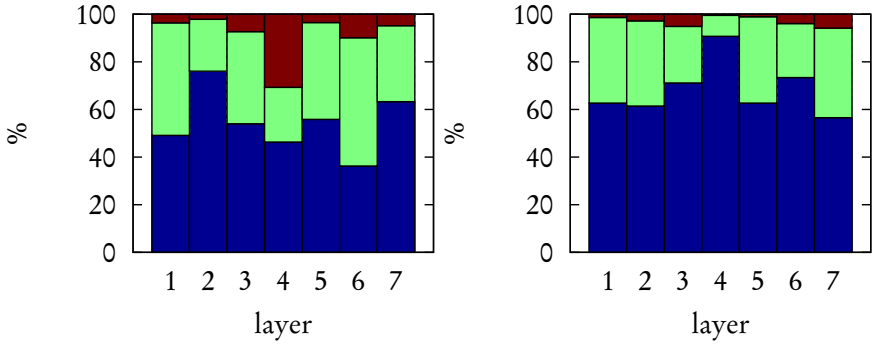

Figure 4.22: Area fractions of the clusters for the various layers. The colours are the same as in Fig. 4.21. Left panel: calcium; right panel: silicon.

it can be seen that the elements are complementary. In regions a large amount of with symbol C of the one element, symbol A dominates for the other. Symbol B regions act as filling and transition areas.

In our analysis we are mostly interested in how much each element is present in one layer and how it is distributed. In Fig. 4.22 it is shown which fraction of the area within one layer is covered by each symbol. In nearly all layers symbol A dominates, thus in most areas the density of the measured elements is low. However, one can also identify layers with remarkably high abundance of certain elements like layer 4 for calcium. From this particular layer it becomes also clear that calcium and silicon are in some sense complementary elements: when calcium content is high then the silicon content is low. From this information one can conjecture that the formation of layer 4 may be due to other mechanisms than the other layers.

As discussed above the relative amount of material in each layer is some useful

information which can be extracted by the cluster algorithm. But in general one is not only interested in the overall content of elements in each layer, even more important is the spatial distribution of the elements within each layer. Usually one wants to know if the material is clustered or spread. In terms of symbolic dynamics we want to gain information on the distribution of patches from class C. A standard measure often used to address this question is the lacunarity (Mandelbrot 1983; Allain and Cloitre 1991; Plotnick et al. 1996). However, it did not yield satisfactory results in our application. It detected randomly scattered, clustered sets, but failed to return a reasonable mean patch size. Thus, in order to gain more insight into the typical length scales of the different symbol clusters, we calculated the maximal numbers of connected pixels in vertical direction. We have chosen this direction because it is much easier to handle the rather complex boundaries of the layers in vertical direction compared to the horizontal one. But the results should not depend on the direction chosen. The distribution of the lengths is shown in Figs. 4.23. The mean lengths for symbol C are listed in Tab. 4.4. It can be seen that the slope of the decrease in length vs. frequency is nearly the same in every layer for symbols A and B. We now consider the maximal chain lengths of the different symbols in the layers. For calcium's symbol A the shortest lengths are found in layer 6. Their maximum length is 0.13 mm, the longest chains are in layer 7 and maximally 0.25 mm long. For symbol B the shortest length is in layer 4 (0.07 mm) and the longest in layer 2 (0.16 mm). For symbol C the shortest length is in layer 2 (0.02 mm) and the longest in layer 4 (0.14 mm). The length spectrum of silicon differs substantially from spectra obtained for calcium. The shortest lengths are in layer 2 (0.2 mm) for symbol A, layer 4 (0.06 mm) for symbol B and again layer 4 (0.025 mm) for symbol C. The longest chains are found in layer 4 (0.35 mm) for symbol A, layer 7 (0.16 mm) for symbol B and layer 2 (0.1 mm) for symbol C. In layer 4 we get the largest contiguous calcium abundance areas. They range up to 0.14 mm. The size of the largest silicon clusters is dependent on the particular layer and lies between 0.025 mm and 0.1 mm.

4.3.4 Discussion

To tackle the problem of characterising different layers of sediment in terms of their structures, we have used entropy measures as well as methods from symbolic dynamics. We have shown that the Kullback-Leibler distance between distribution functions is a good measure to characterise the homogeneity of the distribution of chemical elements. It turned out that one has to compare the distributions

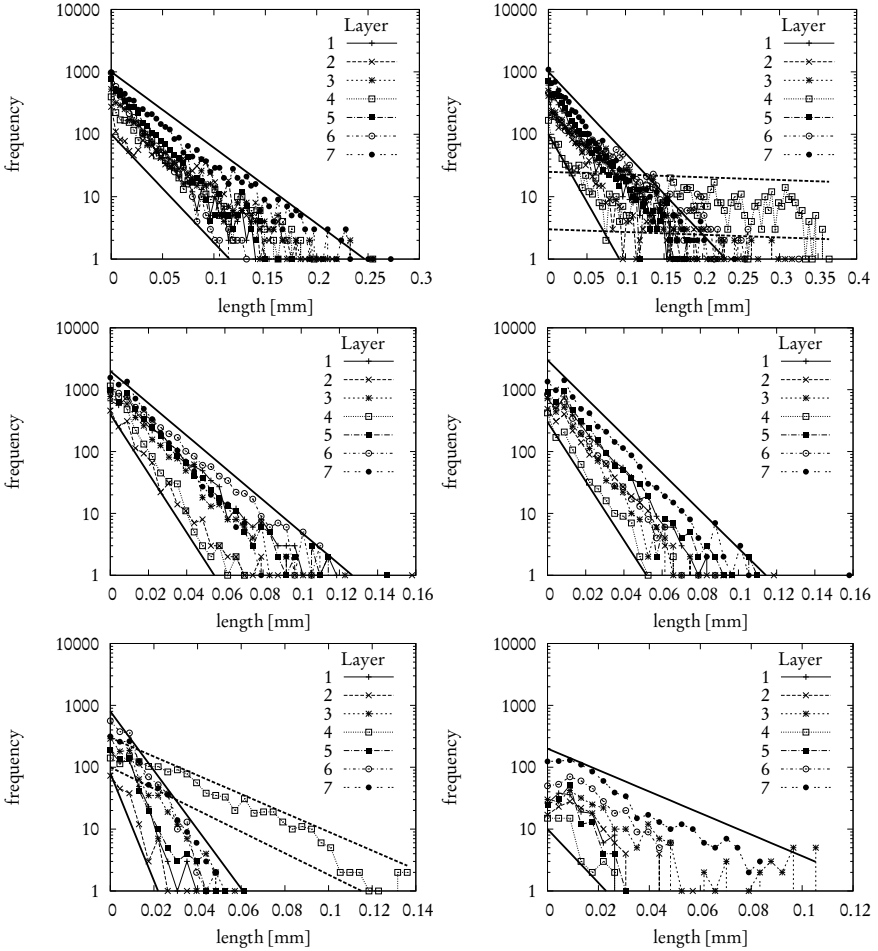

Figure 4.23: Length distributions of contiguous symbols in vertical direction for calcium. From top to bottom: symbol A, B, C. The thick solid lines are inserted by hand for orientation. The thick dashed line marks the corridor of the microbial mat layer. Note the different scales of the abscissa. The left column shows the results for calcium, the right one for silicon.

Layer	Ca	Si
1	2.36	3.10
2	2.31	3.89
3	2.70	6.21
4	7.17	2.62
5	2.49	2.93
6	2.52	4.24
7	2.85	4.77

Table 4.4: Mean lengths of contiguous high density clusters in vertical direction.

obtained from the electron microscopy images of the sediment with artificially created Poisson distributed random surfaces using the KL distance. Due to the same mean value of the distributions the KL distance is a reliable measure for the structuredness of the sediment surface. By contrast, the comparison with distributions in unstructured samples like glass as a reference yields incorrect results which are misleading. Thus we conclude that amorphous reference samples are not a good choice when using KL distances. Moreover, our method of comparing the measurements to Poisson-distributed surfaces is much simpler as no additional measurements are required and adapted to the problem. It is very easy to automate the analysis. Only the mean value and distributions have to be calculated from the data. From the information the Poisson distributed random numbers have to be generated and the KL distance can be calculated. This is very easily scriptable in a computer program.

We also showed that the method is suitable to classify different layers in the sediment. Especially layer 4 can be well isolated from the other layers. It has an eye catchingly high KL distance in the calcium measurement which reflects the high structuredness and clustering of this chemical element. Additionally, this layer exhibits a lack of silicon. The significant differences in both the calcium and the silicon measures enable to discriminate and to identify a buried microbial mat (layer 4) within in a sequence of siliciclastic laminae (layers 1 to 3 and 5 to 7) (cf. Fig. 4.15). Silicon constitutes quartz grains of the clastic laminae. Quartz minerals are seldom in microbial mats, since the mats grow during times of low sedimentation rates. The organic matter is subsequently mineralised and partially replaced by calcium-

minerals after burial of a microbial mat grown at the surface. These calcium-minerals, however, are not formed or are unstable within the siliciclastic laminae (Kropp et al. 1997).

We further derived estimations on typical sizes of regions rich of one element or poor of it in the sediments. We achieved this estimation by coarse graining the raw measurement data in terms of symbolic dynamics and then studying the resulting patterns. The coarse graining sorts every measurement point in one of three categories: element abundance is high, medium or low. This could be expected for the sandy material in the research area. The statistical measures yield quantitative information on the porous siliciclastic layers and the alternating microbial mats. Measures on the distribution of silicon correspond to the grain sizes of the quartz minerals constituting the inorganic skeleton of the sedimentary profile. Individual grains of sizes up to 110 μm are indicated (Fig. 4.23). This is in agreement with petrographic grain size analyses of these fine sands (mean grain sizes between 70 and 120 μm of the supratidal sediments of Mellum Island) (Gerdes et al. 1985). The deposition of individual grains is a stochastic sedimentation process of independent events by nature. The biogeochemical process of calcium mineralisation coupled with the biodegradation of microbial mats can clearly be distinguished by measures of a more homogeneous distribution pattern which reflect a complex in situ process. The size of the resulting clusters is 120 to 140 μm in maximum. Calcium indicates clusters of authigenic high-magnesium calcite (Kropp et al. 1997). The growth of these clusters is limited by intrinsic properties, i.e. pore size or microbial activity, and therefore controlled by a set of interdependent processes.

The measures on partially mineralised microbial mats significantly differ from those obtained for siliciclastic layers, i.e. the slope of the corridor of length distributions of contiguous symbol C in Fig. 4.23 (clusters of calcium-minerals formed during the mineralisation of microbial mats) and of symbol A in Fig. 4.23 (microstructure of clastic grains in microbial mats) are less steep than corridors of data on siliciclastic layers.

4.4 Summary

In this chapter we presented an algorithm, which is able to discriminate layers of different characteristics within sediments. Our application to artificial and real experimental systems yields very good agreements between expected and calculated results. The algorithm is a combination of the wavelet multiscale

decomposition and moving average techniques. It has four degrees of freedom which have to be chosen by the user: the maximum decomposition level, the number of layer boundaries and the width and height of the moving average window. The maximum decomposition level is strongly dependent on the amount of the data measured. For our application a number of 4 gives satisfying results and a higher number would have led to unacceptable small images. If the number of layers is not too high it sometimes can be guessed by visual inspection, otherwise one has to play a bit by adding more and more boundaries. The size of the moving average window is a bit more tricky and has to be found by trying different sizes, but in practice this has proven to be not too difficult.

We have shown that the algorithm significantly outperforms the results of a standard edge detection method. The algorithm may be a helpful tool for detecting layer boundaries as a prerequisite for a quantitative analysis of sediment profiles. Extensions of this algorithm are possible by using other wavelets as the basis of the decomposition.

Furthermore, we developed and applied a robust method to quantify the textural and structural homogeneity of layered sediments. The Kullback-Leibler distance proves to be an adequate measure for this. It enables to characterise areas of arbitrary shape. Comparisons of sedimentary structures which are known to be homogeneous may produce misleading results.

We introduce a way to filter measurement noise with the help of symbolic dynamics. With the filtered sediment profile it is then possible to extract information about characteristic patch sizes and chemical element abundance in every layer. The method can be used for measurements at arbitrary scale.

We were able to isolate a buried and partially biodegraded microbial mat in a siliciclastic sequence and quantify its characteristics based on geometrical information on the concentration pattern of elements. Silicon was proved to be an indicator of autochthonous physical sedimentation processes. Calcium indicates biogeochemical processes in a siliciclastic environment. Comparisons with samples from other areas are needed in order to give a more general interpretation on the use of elementary patterns as proxies for sedimentary processes. This is subject to ongoing research.

5 Summary and Outlook

We presented and discussed several methods to analyse surfaces generated by mechanisms where the underlying process is not fully understood. In the two examples we examined in this thesis the surfaces were formed by an interplay of many processes that could not be easily divided. We made use of the fact that the *a priori* assumption could be made that these processes act on a multitude of time and spatial scales. Our methods exploited this fact by extracting the information contained in the scales of the surfaces. They make the precise mathematical description of the surfaces' properties possible. On the one hand we successfully applied two multifractal methods to characterise the surfaces generated by a laser beam melt ablation process. They measure the local scaling of the heights at each measurement point on the material surface versus the size of an environment around each point. This gives insight into the fluctuation behaviour of the surface heights on many scales. On the other hand we created an algorithm which makes use of multiscale wavelet decomposition to remove the information contained in some scales and only keep it in the scales relevant for our application of tidal flat sediment analysis. It turned out that this is very useful for the division of the sediment into parts with similar statistics.

In our first example we analysed height profiles of the metal surfaces generated by a laser beam melt ablation process. The surface is melted by a high power laser beam and uses a high pressure gas jet to simultaneously blow out the melt. Each time the laser is run over the surface a depressed track emerges. Several of those ablation tracks can be put next to each other such that a larger depression in the material is obtained. The aim is to create a deep and broad depression which is smooth and at the same time sustain high ablation rates. At the moment this aim is not reached. The surface quality in terms of roughness is either bad or the ablation rate is low. The interaction of many effects like melt surface tension, Marangoni instabilities, laser heating and gas jet turbulence introduces processes on many time and spatial scales that are hard to distinguish. We succeeded in deriving a reasonable window of external process parameters where the method yields a good

compromise between ablation depth and surface smoothness.

We found a monotonous relationship between the arithmetic mean roughness and the material feeding speed for fixed laser power. It holds for all parameter combinations we used except one. This exception happens for very high laser powers and low feeding speeds. In this regime additional processes set in that prevent the ablation of more material. We assume that the energy is so high that the metal starts to evaporate. This consumes energy that lacks for the melting of more material. Outside this new regime the monotonous relationship allows us to predict the expected surface roughness for a given parameter combination.

We also showed that the line energy alone, often used by engineers as the key parameter of the external forcing, is not suitable to predict the surface properly. Instead the laser power and the feeding velocity have to be considered separately. This result implies that analytic models such as developed in Golovin et al. (2001) which have only one control parameter have to be adjusted.

Further, our study showed that the shape of the surface at the current position is only little determined by the shape of the previous position. On the other hand the shape of the previous ablation track has some great influence on the shape of the current track. Therefore, an online control has to rely largely on the information of the previous track from which the suitable process parameters for the succeeding track have to be calculated in order to adjust any deviations from the desired surface shape. We see that the surface formation is dominated by nonlinear effects in ablation direction, while linear ones are strong in perpendicular direction.

A multifractal analysis of the surface tracks showed an evident relationship of the adjustable process parameters and the multifractal spectrum. For all laser powers used in the experiments the maximum of the spectrum shifts towards higher Hölder exponents with decreasing feeding velocity. This indicates that the surfaces tend to develop larger scaled structures if more energy is put into the material. This can be explained by the fact that if too much material is molten, the impulse of the gas jet is not sufficient to remove all melt from the surface. The remaining melt pools joins together and the surface tension causes larger structures. For fast feeding speeds the opposite is true. All molten material is immediately blown out and the fluctuations take place on smaller scales. The multifractal spectrum also gives information on the scaling range in which the fluctuations take place. In our samples this is about 80 to 183 μm. It is now possible to make computer simulations that create artificial surfaces with the same multifractal statistics and to check physical models if they produce similar characteristics.

We have developed an offline control of the laser beam melt ablation process. The correlations of mean surface roughness and the multifractal spectrum to the process parameters allow to predict fluctuations and roughness of the surfaces generated. The nonlinear analysis on many scales has given much insight into the structure of the generated surfaces where linear analyses only detected noise. The methods provide an useful classification scheme. We made use of the fact that the structures become stable after a transient regime and used a one dimensional multifractal analysis. This allowed a much better utilisation of the short data sets.

In a further step a two dimensional analysis should be applied but it has to be expected that larger data sets are needed to yield reliable results. For an online control suitable state variables are still needed. The common ones, current laser power and optical emissions, have proven to be problematic as a dependence on the surface characteristics could not be found. Nonlinear correlation methods or black box modelling methods may give better results here.

In our second application we studied the layout and formation of recent tidal flat sediments. Those sediments consist of multiple layers which differ in grain and pore sizes as well as chemical element composition. The stratification reflects the different formation mechanisms. In our study we chose a sediment which contains a microbial mat layer. This was formed by the action of microorganisms within the sediment while the majority of the other layers was formed by sedimentation processes. The sediments were measured with a X-ray backscattering microscope. It returned density images of chemical element concentrations. The images have a natural size of a few millimetres. As chemical elements we chose silicon and calcium. Silicon is the main component of sedimented inorganic material while calcium is an important part of organic matter and may serve as proxy for early diagenetic processes and biogeochemical calcium mineralisation.

Our first task was to develop a criterion to distinguish the sediment layers within the microscopy images. We defined the layer boundaries to be connected lines of maximal vertical concentration gradients which are more or less parallel to the image baseline. With this definition it was possible to develop a numerical algorithm which finds the layer boundaries automatically. This simplifies the analysis of single layers significantly. As the data is disturbed by measurement noise, it is necessary that the algorithm uses some techniques to filter the noise. We use a multiscale approach which has proved to be very helpful. The relevant structures are mostly large scaled while the measurement noise plays only a role on small scales. With the multiscale wavelet decomposition it is possible to successively remove information on desired scales. We successfully applied the algorithm to an artificial

example and an image of a borehole core as well as to our tidal flat sediments. It is a huge improvement over traditional gradient finding algorithms known from image analysis. This is possible by the assumption of further constraints for the layer boundaries which are reasonable for this particular application. These constraints help avoiding lots of false positives. Our algorithm provides a helpful tool for the quantitative analysis of sedimentary layers.

In the next step we developed measures to characterise the various sediment layers in order to quantitatively distinguish them. A major focus of our work was on the separation of noise and signal. We developed a method to quantify the degree of structural organisation in a particular sediment layer. The method uses the Kullback-Leibler distance between the distribution curve of the measured chemical element densities and a Poisson distributed density image of the same size. We showed that this measure is well able to distinguish between structured and unstructured samples. It also provides a quantification of the structuring for the sediment layers. We demonstrated that our measure is able to locate the microbial mat layer by yielding significantly different results for silicon and calcium compared to layers whose formation was dominated by sedimentation.

We furthermore introduced techniques known from symbolic dynamics to the analysis of the sediment profile. In order to remove the measurement noise from the images we created embedding vectors for the measurement points and its next neighbours and then performed a cluster analysis in this newly created vector space. We divided the space in three regions which correspond to regions of low, medium and high element concentrations in the sediment. This way we get a coarse grained profile with an optimal distinction of the classes. Our results confirm that the microbial mat layer has the largest calcium clusters and the lowest silicon abundance. We also estimated grain and pore sizes from the symbolic images. This yielded quartz grain diameters of up to 70–120 μm, which is in good agreement with petrographic grain size analyses.

Our methods help experimenters to perform a quantitative analysis of their samples. It is possible to extract layers with special features and assign certain characteristics to them. We identified a microbial mat layer in siliciclastic bedding. It should be possible to identify other geological formations as well but more experimental work is needed here. The proposed methods need to be applied to sediment samples from different areas. By comparing the results the different characteristics can be assigned to certain formations. These comparisons will yield more insight into the possibilities and also limitations of the proposed methods. Our methods are not limited to a special length scale but can be applied to images

of samples from the submillimetre scale to metres and more. This makes them very flexible and useful in a wide range of applications.

Bibliography

G. Ahlers and R.P. Behringer. Evolution of turbulence from the Rayleigh-Bénard instability. *Phys. Rev. Lett.*, 40(11):712–716, 1978.

E. Alessio, A. Carbone, G. Castelli, and V. Frappietro. Second-order moving average and scaling of stochastic time series. *Eur. Phys. J. B*, 27:197–200, 2002.

C. Allain and M. Cloitre. Characterizing the lacunarity of random and deterministic fractal sets. *Phys. Rev. A*, 44(6):3552–3558, 1991.

J. Alvarez-Ramirez, E. Rodriguez, and J.C. Echeverría. Detrending fluctuation analysis based on moving average filtering. *Physica A*, 354:199–219, 2005.

Y. Anguy, R. Ehrlich, A. Ahmadi, and M. Quintard. On the ability of a class of random models to portray the structural features of real, observed, porous media in relation to fluid flow. *Cement and Concrete Composites*, 23:313–330, 2001.

A. Arnéodo, E. Bacry, and J.F. Muzy. The thermodynamics of fractals revisited with wavelets. *Physica A*, 213:232–275, 1995.

A. Arnéodo, N. Decoster, and S.G. Roux. A wavelet-based method for multifractal image analysis. I. Methodology and test applications on isotropic and anisotropic random rough surfaces. *Eur. Phys. J. B*, 15:567–600, 2000.

E. Bacry, J.F. Muzy, and A. Arnéodo. Singularity spectrum of fractal signals from wavelet analysis: Exact results. *J. Stat. Phys.*, 70(3–4):635–674, 1993.

P. Billingsley. *Ergodic Theory and Information*. J. Wiley and Sons, New York, 1965.

A. Block, W. von Bloh, T. Klenke, and H. J. Schellnhuber. Multifractal analysis of the microdistribution of elements in sedimentary structures using images from scanning electron microscopy and energy dispersive x ray spectroscopy. *J. Geophys. Res.*, 96(B10):223–230, 1991.

W. Brozio. *Temperaturmessung und Laserstrahlprofilanalyse mit der $YBa_2Cu_3O_7$-Atomlagenthermosäule*. PhD thesis, Universität Regensburg, 1999.

K. Bube, T. Klenke, and U. Feudel. An algorithm for detecting layer boundaries in sediments. *Nonlin. Processes Geophys.*, 13:661–669, 2006a.

K. Bube, T. Klenke, J.A. Freund, and U. Feudel. Statistical measures of distribution patterns of silicon and calcium in marine sedimentary layers. Submitted to J. Geophys. Res., 2006b.

K. Bube, C. Rodrigues Neto, R. Donner, U. Schwarz, and U. Feudel. Linear and nonlinear characterization of surfaces from a laser beam melt ablation process. *J. Phys. D: Appl. Phys.*, 36(7):1405–1412, 2006c.

J. Canny. A computational approach to edge detection. *IEEE Trans. Patt. Anal. Mach. Intell.*, 8(6):679–698, 1986.

G. Cantor. Ueber unendliche, lineare Punktmannichfaltigkeiten. *Math. Ann.*, 21 (4):545–591, 1883.

C. Capilla. Application of the Haar wavelet transform to detect microseismic signal arrivals. *J. Appl. Geophys.*, 59(1):36–46, 2006.

A. Chhabra and R.V. Jensen. Direct determination of the $f(\alpha)$ singularity spectrum. *Phys. Rev. Lett.*, 62(12):1327–1330, 1989.

G.R.J. Cooper. Interpreting potential field data using continuous wavelet transforms of their horizontal derivatives. *Comput. Geosci.*, 32(7):984–992, 2006.

A. Cser. *Laserstrahlschmelzabtrag – Prozessanalyse und -modellierung*. PhD thesis, Friedrich-Alexander-Universität Erlangen-Nürnberg, 2005. ISBN 3-87525-227-6.

A. Cser, R. Donner, K. Bube, A. Otto, U. Schwarz, and U. Feudel. Untersuchung nichtlinear-dynamischer Phänomene beim Laserstrahlschmelzabtrag. Project final report, VW Foundation, 2004. Project Numbers I/75 649, I/75 650.

I. Daubechies. *Ten Lectures on Wavelets*, volume 61 of *CBMS–NSF Regional Conference Series in Applied Mathematics*. SIAM Publications, Philadelphia, 1992.

N. Decoster, S.G. Roux, and A. Arnéodo. A wavelet-based method for multifracal image analysis. II. Applications to synthetic multifractal rough surfaces. *Eur. Phys. J. B*, 15:739–764, 2000.

DIN 4287. *DIN EN ISO 4287: Geometrische Produktspezifikationen (GPS) – Oberflächenbeschaffenheit: Tastschnittverfahren – Benennungen, Definitionen und Kenngrößen der Oberflächenbeschaffenheit*. Berlin, 1998.

R. Donner, A. Cser, U. Schwarz, A. Otto, and U. Feudel. An approach to a process model of laser beam melt ablation using methods of linear and non-linear data analysis. In G. Radons and R. Neugebauer, editors, *Nonlinear Dynamics of Production Systems*, pages 453–468, Weinheim, 2004. Wiley Europe.

G.V. Ermolaev, O.B. Kovalev, A.M. Orishich, and V.M. Fomin. Mathematical modelling of striation formation in oxygen laser cutting of mild steel. *J. Phys. D: Appl. Phys.*, 39:4236–4244, 2006.

Expedition 301 Scientists. Expedition 301 summary. In A.T. Fisher, T. Urabe, A. Klaus, and the Expedition 301 Scientists, editors, *Proc. IODP*, volume 301, College Station TX, 2005. Integrated Ocean Drilling Program Management International, Inc. doi: 10.2204/iodp.proc.301.101.2005.

J. Feder. *Fractals*. Plenum Press, New York, 1988.

M. Fedi, V. Paoletti, and A. Rapolla. The role of multilevel data in potential field interpretation. *Comput. Geosci.*, 31(6):681–688, 2005.

U. Frisch. *Turbulence*. Cambridge University Press, 1995.

G. Gerdes, W.E. Krumbein, and H.-E. Reineck. The depositional record of sandy, versicolored tidal flats (Mellum island, southern North Sea). *J. Sediment. Petrol.*, 55(2):265–278, 1985.

A.A. Golovin, A.A. Nepomnyashchy, S.H. Davis, and M.A. Zaks. Convective Cahn-Hilliard models: From coarsening to roughening. *Phys. Rev. Lett.*, 86(8): 1550–1553, 2001.

P. Grassberger. Generalized dimensions of strange attractors. *Phys. Lett. A*, 97(6): 227–230, 1983.

C. Grebogi, E. Ott, and J.A. Yorke. Chaos, strange attractors, and fractal basin boundaries in nonlinear dynamics. *Science*, 238:632–638, 1987.

D.M. Green and J.A. Swets. *Signal detection theory and psychophysics*. Wiley, New York, 1966.

J. Gunninga and M.E. Glinsky. Wavelet extractor: A bayesian well-tie and wavelet extraction. *Comput. Geosci.*, 32(5):681–695, 2006.

M. Haase and B. Lehle. Tracing the skeleton of wavelet transform maxima lines for the characterization of fractal distributions. In M.M. Novak, editor, *Fractals and beyond*, pages 241–250. Wold Scientific, Singapore, 1998.

T.C. Halsey, M.H. Jensen, L.P. Kadanoff, I. Procaccia, and B.I. Shraiman. Fractal measures and their singularities: The characterization of strange sets. *Phys. Rev. A*, 33(2):1141–1151, 1986.

B.-L. Hao. Symbolic dynamics and characterization of complexity. *Physica D*, 51: 161–176, 1991.

J.A. Hartigan. *Clustering Algorithms*. Wiley, New York, 1975.

J.A. Hartigan and M.A. Wong. A *k*-means clustering algorithm. *Appl. Statist.*, 28 (1):100–108, 1979.

F. Hausdorff. Dimension und äußeres Maß. *Mathematische Annalen*, 79(1–2): 157–179, 1918.

R. Haussels, T. Klenke, J. Kropp, and W. Ebenhöh. Observations on the influence of pore space geometry on concentration patterns and transportation properties of dissolved oxygen in a bioactive sandy sediment by a lattice Boltzmann automaton model. *Hydrol. Proc.*, 15:81–96, 2001.

H.G.E. Hentschel and I. Procaccia. The infinite number of generalized dimensions of fractals and strange attractors. *Physica D*, 8(3):435–444, 1983.

G.B. Hoflund, Z.F. Hazos, and G.N. Salaita. Surface characterization study of Ag, AgO, and Ag_2O using x-ray photoelectron spectroscopy and electron energy-loss spectroscopy. *Phys. Rev. B*, 62(16):11126–11133, 2000.

H. Hügel. *Strahlwerkzeug Laser*. Teubner Verlag, Stuttgart, 1992.

H.E. Hurst. Long-term storage capacity of reservoirs. *Trans. Am. Soc. Civ. Eng.*, 116:770–808, 1951.

Y. Jun and X.L. Wu. Large-scale intermittency in two-dimensional driven turbulence. *Phys. Rev. E*, 72:035302, 2005.

J.W. Kantelhardt, S.A. Zschiegner, E. Koscielny-Bunde, S. Havlin, A. Bunde, and H.E. Stanley. Multifractal detrended fluctuation analysis of nonstationary time series. *Physica A*, 316:87–114, 2002.

T. Kohonen. *Self-organizing maps*. Springer, Berlin, 3rd edition, 2001.

E. Koscielny-Bunde, A. Bunde, S. Havlin, H.E. Roman, Y. Goldreich, and H.-J. Schellnhuber. Indication of a universal persistence law governing atmospheric variability. *Phys. Rev. Lett.*, 81(3):729–732, 1998.

E. Koscielny-Bunde, J.W. Kantelhardt, P. Braun, A. Bunde, and S. Havlin. Long-term persistence and multifractality of river runoff records: Detrended fluctuation studies. *J. Hydrol.*, 322(1–4):120–137, 2006.

J. Kropp, A. Block, W. von Bloh, T. Klenke, and H.J. Schellnhuber. Multifractal characterization of microbially induced calcite formation in recent tidal flat sediments. *Sediment. Geol.*, 109(1/2):37–52, 1997.

S. Kullback and R.A. Leibler. On information and sufficiency. *Annals of Math. Stat.*, 22(1):79–86, 1951.

A. La Porta, G.A. Voth, A.M. Crawford, J. Alexander, and E. Bodenschatz. Fluid particle accelerations in fully developed turbulence. *Nature*, 409:1017–1019, 2001.

B. Läßiger. *Kontrollierter Formabtrag durch Sublimation mittels Laserstrahlung*. Shaker Verlag, Aachen, 1995.

E.N. Lorenz. Deterministic nonperiodic flow. *J. Atmos. Sci.*, 20(2):130–141, 1963.

A. K. Louis, P. Maaß, and A. Rieder. *Wavelets*. Teubner, Stuttgart, 1998.

S. Lovejoy. Area-perimeter relation for rain and cloud areas. *Science*, 216:185–187, 1982.

S. Lovejoy and D. Schertzer. Generalized scale invariance in the atmosphere and fractal models of rain. *Water Resour. Res.*, 21:1233–1250, 1985.

K.J. Måløy, J. Feder, and T. Jøssang. Viscous fingering fractals in porous media. *Phys. Rev. Lett.*, 55:2688–2691, 1985.

S.G. Mallat. A theory for multiresolution signal decomposition: The wavelet representation. *IEEE Trans. Pattern Anal. Mach. Intell.*, 11(7):674–693, 1989a.

S.G. Mallat. Multiresolution approximations and wavelet orthonormal bases of $L^2(R)$. *Trans. Amer. Math. Soc.*, 315(1):69–87, 1989b.

S.G. Mallat and W.L. Hwang. Singularity detection and processing with wavelets. *IEEE Trans. Info. Theory*, 32(2):617–643, 1992.

B.B. Mandelbrot. How long is the coast of Britain? *Science*, 156:636–638, 1967.

B.B. Mandelbrot. *The Fractal Geometry of Nature*. Freeman, New York, 1983.

B.B. Mandelbrot and J.R. van Ness. Fractional Brownian motions, fractional noises and applications. *SIAM Review*, 10:422–437, 1968.

D. Maraun, H.W. Rust, and J. Timmer. Tempting long-memory – on the interpretation of DFA results. *Nonlinear Proc. Geophys.*, 11:495–503, 2004.

C.-S. Maroni, A. Quinquis, and S. Vinson. Horizon picking on subbottom profiles using multiresolution analysis. *Digital Signal Processing*, 11:269–287, 2001.

J. Morford, L. Kalnejais, W. Martin, R. Francois, and I.M. Karle. Sampling marine pore waters for Mn, Fe, U, Re and Mo: Modifications on diffusional equilibration thin film gel probes. *J. Exper. Mar. Biol. and Ecol.*, 285/286:85–103, 2003.

T. Mościcki, J. Hoffman, and Z. Szymański. Modelling of plasma plume induced during laser welding. *J. Phys. D: Appl. Phys.*, 39:685–692, 2006.

J.F. Muzy, E. Bacry, and A. Arnéodo. Wavelets and multifractal formalism for singular signals: Application to turbulence data. *Phys. Rev. Lett.*, 67(25):3515–3518, 1991.

B. Niebuhr and A. Prokoph. Periodic-cyclic and chaotic successions of upper cretaceous (cenomanian to campanian) pelagic sediments in the north german basin. *Cretaceous Research*, 18(5):731–750, 1997.

P. Oświęcimka, J. Kwapień, and S. Drożdż. Wavelet versus detrended fluctuation analysis of multifractal structures. *Phys. Rev. E*, 74:016103, 2006.

E. Ott. Strange attractors and chaotic motions in dynamical systems. *Rev. Mod. Phys.*, 53(4):655–671, 1981.

E. Ott. *Chaos in dynamical systems*. Cambridge University Press, Cambridge, 1993.

A. Papoulis. *Probability, Random Variables and Stochastic Processes*. McGraw-Hill, New York, 1984.

U. Parlitz and C. Merkwirth. Prediction of spatiotemporal time series based on reconstructed local states. *Phys. Rev. Lett.*, 84(9):1890–1893, 2000.

C.-K. Peng, S.V. Buldyrev, S. Havlin, M. Simons, H.E. Stanley, and A.L. Goldberger. Mosaic organization of DNA nucleotides. *Phys. Rev. E*, 49(2):1685–1689, 1994.

F. Pettijohn and P.E. Potter. *Atlas and glossary of primary sedimentary structures*. Springer, Berlin, 1964.

R.E. Plotnick, R.H. Gardner, W.W. Hargrove, K. Prestegaard, and M. Perlmutter. Lacunarity analysis: A general technique for the analysis of spatial patterns. *Phys. Rev. E*, 53(5):5461–5468, 1996.

S. Rath, D. Paramanik, S.N. Sarangi, S. Varma, and S.N. Sahu. Surface characterization and electronic structure of HgTe nanocyrstalline thin films. *Phys. Rev. B*, 72:205410, 2005.

C. Rodrigues Neto, K. Bube, A. Cser, A. Otto, and U. Feudel. Multifractal spectrum of a laser beam melt ablation process. *Physica A*, 344:580–586, 2004.

O.E. Rössler. Chaotic behavior in simple reaction systems. *Z. Naturforsch. A*, 31: 259–264, 1976.

D. Ruelle and F. Takens. On the nature of turbulence. *Commun. Math. Phys.*, 20 (3):167–192, 1971.

A. Ruf, P. Berger, F. Dausinger, and H. Hügel. Analytical investigations on geometrical influences on laser drilling. *J. Phys. D: Appl. Phys.*, 34:2918–2925, 2001.

D. Rybski, A. Bunde, S. Havlin, and H. von Storch. Long-term persistence in climate and the detection problem. *Geophys. Res. Lett.*, 33:L06718, 2006.

M. Sahimi. Fractal-wavelet neural-network approach to characterization and upscaling of fractured reservoirs. *Comput. Geosci.*, 26(8):877–905, 2000.

D. Schubart. *Prozeßmodellierung und Technologieentwicklung beim Abtragen mit CO_2-Laserstrahlung*. PhD thesis, Friedrich-Alexander-Universität Erlangen-Nürnberg, 1999. ISBN 3-87525-122-9.

D. Schuöcker. Dynamic phenomena in laser cutting and cut quality. *Appl. Phys. B*, 40:9–14, 1986.

C.E. Shannon. A mathematical theory of communication. *The Bell System Technical Journal*, 27(3):379–423, 1948.

J. Shao and Y. Yan. Review of techniques for on-line monitoring and inspection of laser welding. *J. Phys.: Conf. Ser.*, 15:101–107, 2005.

R. Shaw. *The Dripping Faucet as a Model Chaotic System*. Aerial Press, Santa Cruz, 1984.

D.R. Smith, D. Schurig, and J.J. Mock. Characterization of a planar artificial magnetic metamaterial surface. *Phys. Rev. E*, 74:036604, 2006.

P. Solana, P. Kapadia, J.M. Dowden, and P.J. Marsden. An analytical model for the laser drilling of metal with absorption within the vapour. *J. Phys. D: Appl. Phys.*, 32:942–952, 1999.

W.M. Steen and K. Watkins. *Laser Material Processing*. Springer, London, 2003.

Z.R. Struzik. Removing divergences in the negative moments of the multi-fractal partition function with the wavelet transformation. Technical report, Centrum voor Wiskunde en Informatica, Amsterdam, 1998.

U. Sutor. *Formabtrag mit CO_2-Laserstrahlung*. Shaker Verlag, Aachen, 1994.

C. Torrence and G.P. Compo. A practical guide to wavelet analysis. *Bull. Amer. Meteor. Soc.*, 79:61–78, 1998.

C. Tsallis. Possible generalization of Boltzmann-Gibbs statistics. *J. Stat. Phys.*, 52 (1–2):479–487, 1988.

M.E. Tucker. *Sedimentary Petrology*. Blackwell, 2001.

D.L. Turcotte. *Fractals and Chaos in Geology and Geophysics*. Cambridge University Press, Cambridge, 2. edition, 1997.

L. Vázquez, R.C. Salvarezza, P. Ocón, P. Herrasti, J.M. Vara, and A.J. Arvia. Self-affine fractal electrodeposited gold surfaces: Characterization by scanning tunneling microscopy. *Phys. Rev. E*, 49(2):1507–1514, 1994.

A. Vincent and M. Meneguzzi. The spacial structure and statistical properties of homogeneous turbulence. *J. Fluid Mech.*, 225:1–20, 1991.

P.T. Visscher, R.P. Reid, and B.E. Bebout. Microscale observation of sulfate reduction: Correlation of microbial activity and lithified micrtic laminae in modern marine stromatolithes. *Geology*, 28:919–922, 2000.

M. Waechter, F. Riess, H. Kantz, and J. Peinke. Stochastic analysis of surface roughness. *Europhys. Lett.*, 64(5):579–585, 2003.

S. Wolfram. Statistical mechanics of cellular automata. *Rev. Mod. Phys.*, 55(3): 601–644, 1983.

S. Zeuner. *Atomlagenthermosäulen in Hochtemperatur-Supraleitern als schnelle Strahlungsdetektoren*. PhD thesis, Universität Regensburg, 1994.

Acknowledgements

I would never have finished this thesis without the support of many nice people. This chapter is dedicated to those who have directly or indirectly supported me. A big sorry to everyone I may have forgotten.

First I would like to thank my supervisor Ulrike Feudel for giving me the opportunity to work in her group, for her support, and for always digging up new funds for me.

I owe much gratitude to Camilo Rodrigues Neto for showing me the world of multifractals and without whom this part of the thesis would never have been realised. He also deserves the credit of inventing the infamous coffee break which is now an established ritual in the group.

This theoretical work would not have been possible without the work of many experimentalists. Thanks to Thomas Klenke and Gisela Gerdes for sharing some of their expertise and knowledge of the tidal flat sediments with me. Furthermore, I thank Adrienn Cser and Andreas Otto for performing the experiments with the laser device whose results contribute a major deal to this thesis. I also thank Reik Donner and Udo Schwarz who helped me a lot during the start of my work. Credits go to Jaqueline Süßfor introducing me to light microscopy, Bert Engelen for pointing me to the IODP database, and Imke Notholt and Sophie Martyna for operating the electron microscope and supplying me with newspapers during long measurement runs.

Thank you also to Jan Freund, who was my room mate for the last years, for many answered questions, explanations and stimulating discussions.

I shall not forget to mention the nice atmosphere in our group Komplexe Systeme. It was a pleasure for me to work there and have lots of incredible talks on unbelievable topics in many coffee breaks. The volleyball matches and the Bosseltouren were also a lot of fun.

Many, many thanks go to Jennifer for all the good time we had.

Also many thanks to my parents and family who always supported me and bore my numerous moves. I guess there still will be some more…

Finally, I would like to thank my girlfriend Tina for giving me all the nice things in life. I promise, there are still a lot more of happy days to come, soon in a threesome.

Kevin Bube
Oldenburg, January 2007

Curriculum Vitae

Name	Kevin Bube
Date of birth	22. 4. 1977
Place of birth	Stade
Nationality	German
Marital status	unmarried

Schooling

1983–1987	Grundschule Fredenbeck
1987–1989	Orientierungsstufe Fredenbeck
1989–1996	Gymnasium Athenaeum Stade

University

1996–2002	Student of Physics at Georg-August-Universität Göttingen May 2002 Diploma degree in Physics Topic of Diploma thesis: *Methods for the correlation analysis of bivariate time series*
since 2002	Member of group "Complex systems / Theoretical physics", Carl-von-Ossietzky Universität Oldenburg

Erklärung

Hiermit erkläre ich, daß ich diese Arbeit selbständig verfasst und keine anderen als die angegebenen Hilfsmittel verwendet habe.

....

Datum Unterschrift